From Synthesis to Application: A Review of $BaZrS_3$ Chalcogenide Perovskites

Author List: Shubhanshu Agarwal*[,1], Kiruba Catherine Vincent*[,1], and Rakesh Agrawal[1,a]

[1]Davidson School of Chemical Engineering, Purdue University, West Lafayette, IN 47907, USA

* Equal Contribution

[a)]**Author to whom correspondence should be addressed**: agrawalr@purdue.edu

Abstract

Chalcogenide perovskites are gaining prominence as earth-abundant and non-toxic solar absorber materials, crystallizing in a distorted perovskite structure. Among these, $BaZrS_3$ has attracted the most attention due to its optimal bandgap and its ability to be synthesized at relatively low temperatures. $BaZrS_3$ exhibits a high light absorption coefficient, excellent stability under exposure to air, moisture, and heat, and is composed of earth-abundant elements. These properties collectively position $BaZrS_3$ as a promising candidate for a wide range of applications, although traditional high-temperature synthesis has primarily been a significant challenge. In this review, we provide a critical discussion of the various synthesis methods employed to fabricate $BaZrS_3$, including solid-state synthesis, nanoparticle synthesis, and vacuum-based as well as solution-based approaches to synthesize thin films. We also comprehensively examine the experimentally measured and theoretically calculated optical, optoelectronic, electronic, and defect properties of $BaZrS_3$. Furthermore, this review highlights the functional devices based on $BaZrS_3$, showcasing applications spanning photovoltaics, photodetection, thermoelectrics, photoelectrochemical water splitting, piezoelectricity, and spintronics. Lastly, we propose a future roadmap to maximize the potential of this material. Additionally, this review extends its focus to $BaHfS_3$ and $BaTiS_3$, discussing their synthesis methods, properties, and explored applications, thereby offering a comparative perspective on this emerging family of chalcogenide perovskites.

1. Introduction

The demand for innovative semiconductors is growing in response to technological progress across various sectors.[1–7] A notable area of focus is the expanding photovoltaics market, which calls for high-quality, cost-effective semiconductors with optimal properties. Photovoltaics are expected to become a primary renewable energy source by the 2050s, emphasizing the need to improve existing solar cell technologies' efficiency.[8–10] Furthermore, there is a push to discover, synthesize, and validate the optoelectronic properties of emerging materials.

Despite the longstanding dominance of single-junction silicon solar cells in the photovoltaic (PV) market, concerns about efficiency stagnation have prompted interest in transitioning to tandem solar cells. These cells can utilize the solar spectrum more effectively, increasing power output per unit area. Although tandem solar cells can theoretically have more than two junctions, the efficiency gains beyond two junctions may not outweigh the additional costs.[11–15] The ideal bandgap for the bottom layer is between 0.9-1.1 eV, while it ranges from 1.6 to 1.9 eV for the top layer. While options for the bottom layer include $Cu(In,Ga)Se_2$ (CIGSe), and silicon, lead halide perovskites are ideally suited for the top layer. Lead halide perovskites offer exceptional potential for optoelectronic applications; however, concerns persist about their toxicity and sensitivity to air and moisture.[16–18]

Efforts such as encapsulation to contain lead and replacing lead with tin or germanium aim to address toxicity concerns associated with halide perovskites. Additionally, surface passivation and using 2D perovskites or 2D/3D perovskite composites show promise for enhanced stability.[19,20] However, any reduction in module lifetime for silicon/perovskite tandems compared to single-junction silicon modules after deployment would negate the benefits of transitioning to tandem solar cells from single-junction. Until substantial improvements in the stability of lead halide perovskites are achieved, justifying the deployment of lead halide perovskite-based tandem PVs remains challenging.

Chalcogenide perovskites have demonstrated early potential for tandem photovoltaic (PV) applications alongside other materials among emerging semiconductors. These materials adopt an ABX_3 structure, where A generally represents Ba, Sr, Ca, or Eu; B represents Zr or Hf; and X represents S (and in some specific cases Se). With bandgaps ranging from 1.7 to 2.4 eV, these materials exhibit corner-sharing octahedra similar to lead halide perovskites, facilitating favorable carrier transport properties.[21–26] For example in $BaZrS_3$, the Zr^{4+} cations are coordinated by six S^{2-} anions, forming ZrS_6 octahedra. These octahedra are corner-shared, forming a 3D network. The Ba^{2+} cations are located in the interstices of the network formed by the ZrS_6 octahedra. Orthorhombic $BaZrS_3$ exhibits slight tilting and rotation of the octahedra (7.027° out-of-phase tilt and 9.0005° in-phase tilt). The absence of this tilting could potentially reduce the bandgap by approximately 0.65 eV.[27,28] Sopiha et al. compiled the formation energies of several of these compounds and predicted that Ba, Sr, and Ca-based perovskites are stable against decomposition into binaries, with the perovskite phase being the ground state at room temperature.[23]

The ABX_3 formula encompasses a range of crystal structures beyond the traditional perovskite arrangement, including the hexagonal $BaNiO_3$-type and needle-like NH_4CdCl_3-type structures, characterized by face-sharing and edge-sharing octahedra. However, these structures inhibit efficient charge transport, making them less suitable for photovoltaic applications. Nonetheless, $BaTiS_3$ and $SrTiS_3$ in

hexagonal structures have shown promise for thermoelectric applications.[29–31] The stability of an ABX_3 compound in a perovskite structure can be estimated using tolerance (t) and octahedral (μ) geometric factors. A stable octahedral configuration is indicated by a μ factor between 0.41 and 0.73, while stability in the perovskite crystal structure corresponds to a t factor between 0.85 and 1.05. Values of t above 1.05 typically result in a hexagonal $BaNiO_3$-type crystal structure, while t below 0.85 leads to needle-like structures.[23,26,32–39] However, most chalcogenide perovskites fall short of meeting the octahedral factor criteria and only marginally satisfy the tolerance factor requirement. Consequently, chalcogenide perovskites often adopt a distorted orthorhombic structure, distinct from the cubic structure of lead halide perovskites.[23,25] The impact of this structural distortion on the optoelectronic and transport properties of chalcogenide perovskites remains an area of ongoing investigation. **Figure 1** shows the crystal structures of $BaZrS_3$, $BaHfS_3$, and $BaTiS_3$. While $BaZrS_3$ and $BaHfS_3$ exhibit distorted perovskite structures, $BaTiS_3$ adopts a hexagonal $BaNiO_3$-type structure.[40] In $BaTiS_3$, Ti^{4+} ions are coordinated by six S^{2-} ions, forming TiS_6 octahedra. These octahedra are linked together along the c-axis, creating infinite one-dimensional chains. The Ba^{2+} ions are situated between these chains, providing charge balance and structural stability.

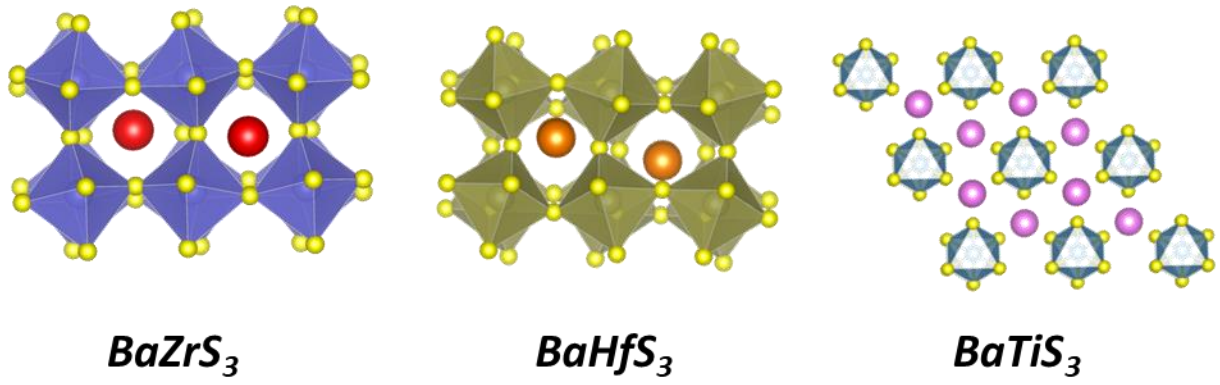

Figure 1. Crystal structures of $BaZrS_3$, $BaHfS_3$, and $BaTiS_3$. $BaZrS_3$ and $BaHfS_3$ exhibit distorted perovskite structures, while $BaTiS_3$ adopts a hexagonal crystal structure.

Other than $BaZrS_3$, Sr-based perovskites have also garnered notable interest from the research community due to their similarly exciting properties, with $SrHfS_3$ exhibiting strong green emission.[41–45] While the term "chalcogenide perovskites" is frequently used, this family of compounds predominantly consists of sulfide materials, with $LaScSe_3$ being the only selenide perovskite reportedly grown under thermal equilibrium growth conditions.[46] Additionally, some tellurium-based compounds have been predicted, such as $ACeTe_3$ (A = Ca, Sr, and Ba), which take on a distorted perovskite phase, though they have not yet been experimentally synthesized.[47] Beyond ABX_3 phases, the Ba-Zr-S system also supports the formation of layered 2D Ruddlesden-Popper phases. These phases have been shown to have lower bandgaps compared to $BaZrS_3$, with strong photoluminescence and high carrier lifetimes, making them promising for optoelectronic applications.[27,28,48–51] However, these compounds have primarily been reported as phase-pure only at high temperatures, and their challenging synthesis remains a bottleneck.[48] Moreover, some first-principle studies have reported exciting combinations of double chalcogenide perovskites, though their syntheses have not yet been achieved.[52–54]

The lower electronegativity of chalcogenides compared to oxides or halides leads to reduced electronegativity differences between the cations and anions, thereby decreasing the ionic nature of the

bonds and increasing covalency. This increased covalency contributes to achieving bandgaps in the visible range for chalcogenide perovskites. Jess et al. and Turnely et al. argued that due to the increased covalency in chalcogenide perovskites, using Shannon ionic radii derived from oxide materials in geometric factors is not ideal for predicting the structure of chalcogenide perovskites. They have proposed modifications to the existing rules to determine the correct phase, such as including the electronegativity differences between the cation and anion in predictions and utilizing ionic radii derived from a sulfide dataset instead. Their studies have also led to the prediction of a host of new possible chalcogenide perovskites, which should be further explored.[55,56]

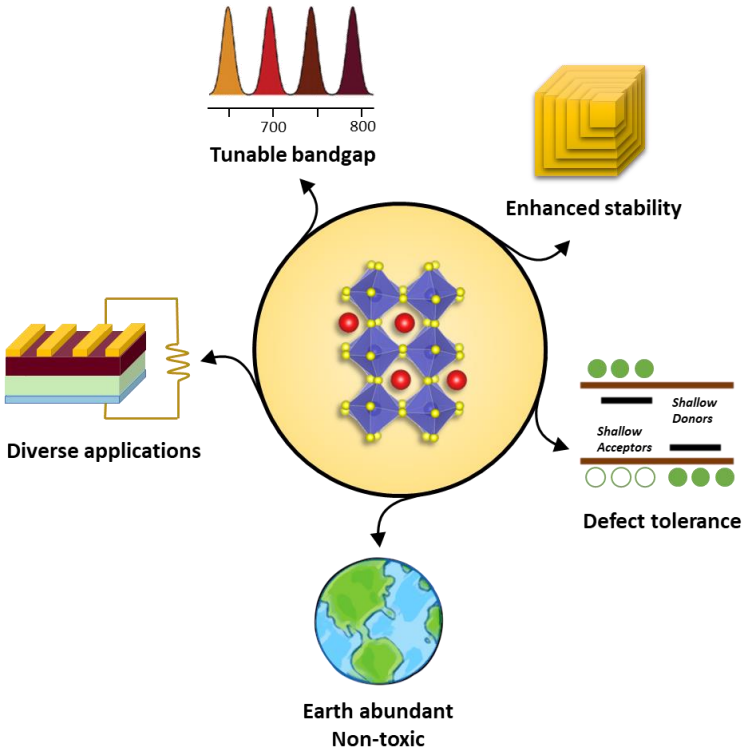

Figure 2. Schematic highlighting the notable properties of chalcogenide perovskites.

All synthesized chalcogenide perovskites exhibit promising properties, and their varying bandgaps make them suitable for various applications (see **Figure 2**). Notably, these materials feature tunable bandgaps, which can be adjusted by changing the elements in the structure or by alloying different elements, resulting in a wide range of bandgap values.[23,57–61] Despite crystallizing in the perovskite structure, they offer enhanced stability against air, moisture, and heat, combining the attractive features of the perovskite crystal structure with the robustness of chalcogenide semiconductors.[48,62–65] Composed of earth-abundant elements primarily sourced from the top 20 elements in the Earth's crust, they align with sustainability goals (see **Figure 3** for the relative abundance of elements).[23,66] DFT-predicted high absorption coefficients on the order of 10^5 cm^{-1} have been experimentally confirmed.[67,68] Additionally, properties such as high dielectric constant, low thermal conductivity, and high Seebeck coefficient suggest potential applications beyond photovoltaics.[66,69] **Figure 4** shows the high dielectric constant observed for cold-sintered $BaZrS_3$ powder and $BaZrS_3$ single crystals, among the highest reported for chalcogenide semiconductors. While other expected properties, such as strong photoluminescence, defect tolerance, and high carrier mobility, require further experimental validation, chalcogenide perovskites remain in the early stages of research and

development. The only reported device utilizing chalcogenide perovskites in a typical thin film architecture has been demonstrated for $LaYS_3$, indicating significant opportunities for other chalcogenide perovskite materials.[70] Additionally, other notable candidate of this family $Ca_3Sn_2S_7$ has been predicted to possess graphene-like linear electronic dispersion, an ultrasmall effective mass, and high carrier mobility. [71]

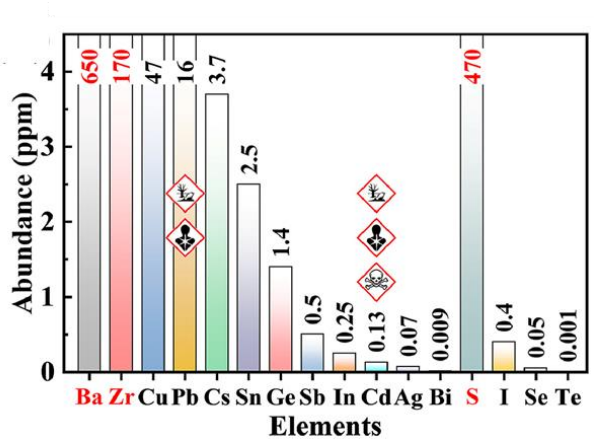

Figure 3. Schematic illustrating the relative abundance of Ba, Zr, and S in comparison to other key elements utilized in thin-film photovoltaic applications. Reproduced with permission.[66] Copyright 2024, Elsevier.

The synthesis of these materials has been reported in the literature with varying levels of difficulty, with $BaZrS_3$ and $BaHfS_3$ being synthesized at the lowest temperatures.[62,72–74] Among these, $BaZrS_3$, with its ideal bandgap of 1.7-1.9 eV for photovoltaic applications, has exhibited defect tolerance and a high dielectric constant. However, a deeper understanding of the key factors for achieving phase-pure synthesis is required. Despite significant progress in synthesizing $BaZrS_3$ at high temperatures, efforts to replicate this success at lower temperatures (<600°C) more suitable for practical applications have been challenging. Although many reports have successfully produced contiguous $BaZrS_3$ films at high temperatures, none have achieved this at lower temperatures, highlighting a significant hurdle. [48,62] **Figure 5** summarizes the strengths of chalcogenide perovskites (especially $BaZrS_3$) and the areas where further work is needed.

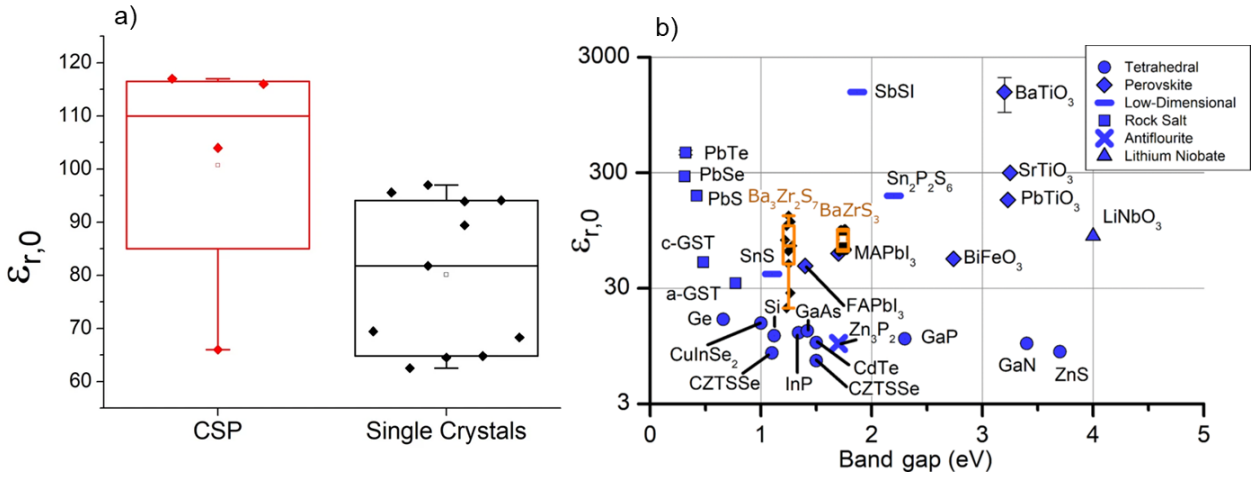

Figure 4. Dielectric constant of $BaZrS_3$ and other inorganic materials. a) Comparison of the dielectric constant for densified $BaZrS_3$ obtained through cold-sintering and single crystal $BaZrS_3$. b) Plot illustrating the relationship between the dielectric constant and bandgap for various inorganic materials. a) and b) Reproduced with permission.[69] Copyright 2021, Springer Nature.

Due to the high potential of $BaZrS_3$ in photovoltaic applications and significant interest from the research community in advancing this material, this report aims to review successful synthesis methods for $BaMS_3$ (M = Ti, Zr, Hf) compounds and their intriguing properties and applications. Additionally, it provides insights to bridge the gaps in synthesis methods, paving the way for the fabrication of contiguous $BaMS_3$ films at low temperatures within practical time frames.

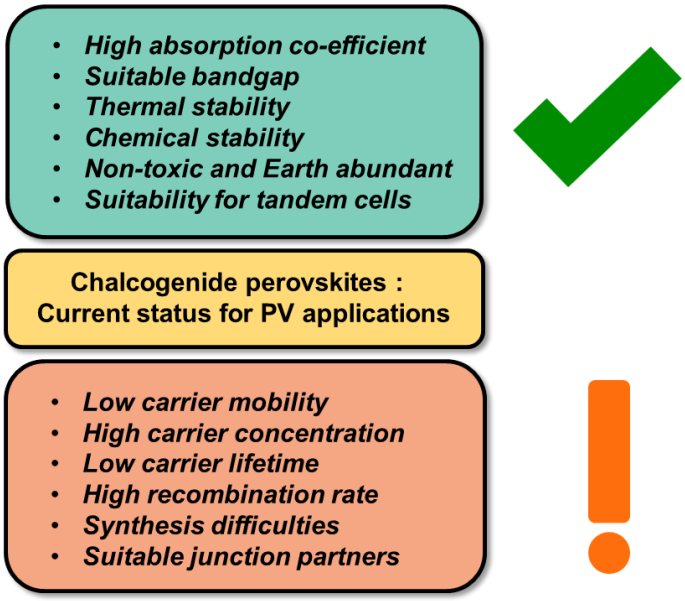

Figure 5. Schematic depicting the current status of chalcogenide perovskites, with a particular focus on $BaZrS_3$, in photovoltaic applications.

2. Synthesis of $BaMS_3$ compounds

Chalcogenide perovskites, often seen as potential high-performing alternatives to halide perovskites, have struggled to match the rapid advancement of their halide counterparts, primarily due to the harsh growth conditions required for their synthesis. $BaZrS_3$ is one of the most extensively studied chalcogenide perovskites, owing to its optimal bandgap and relative ease of synthesis compared to other chalcogenide perovskites. However, the synthesis temperatures for $BaZrS_3$ have typically been much higher than those required for other chalcogenide semiconductors such as $Cu(In,Ga)Se_2$, $Cu_2ZnSnSe_4$, and $AgInSe_2$.[75–79] Nonetheless, recent years have witnessed the development of numerous methods for the synthesis of $BaZrS_3$ and other chalcogenide perovskites. These methods range from flux-driven solid-state synthesis and epitaxial-based film growth techniques to solution-processing approaches, among others (see schematic in **Figure 6** for the four broad class of synthesis methods).

2.1. High-Temperature Synthesis

2.1.1. Solid-state Synthesis

The challenges of high-temperature synthesis have resulted in a wealth of literature focusing on $BaMS_3$ powders rather than thin films. The first reported synthesis of $BaZrS_3$ occurred in 1956 when Hahn and Mutschke combined binary sulfides and heated the powder mixture to temperatures exceeding 1000°C for several weeks to produce $BaZrS_3$.[80] The high stability of starting materials such as metal sulfides, oxides, and carbonates, coupled with the lack of flux, necessitated elevated temperatures for the growth of $BaMS_3$ powders, often surpassing 900°C.[62,67,68] Early transition metals like Ti, Zr, and Hf, known for their high oxophilicity and strong metal-oxygen bonds, have further complicated the synthesis conditions.[81,82]

Despite these challenges, the preferred method for the solid-state synthesis of $BaMS_3$ compounds has been the CS_2 sulfurization of oxide powders. This process involves continuously flowing CS_2 through oxide powders maintained at temperatures exceeding 1000°C for several hours to days.[40,48,83–86] In this method, oxide materials were reduced to their sulfide forms. According to thermodynamic calculations by Agarwal et al., CS_2 sulfurization of oxides is thermodynamically feasible at lower temperatures (<600°C) but may not be kinetically feasible at these temperatures.[73] Nishigaki et al. demonstrated a synthesis approach that involved mixing binary sulfide powders, pelletizing them, and subsequently annealing at temperatures exceeding 1000°C for several days.[67] Additionally, single crystals of $BaZrS_3$ have been produced using the $BaCl_2$ flux and I_2 vapor transport methods.[27,28,64] In both instances, barium sulfide, zirconium powder, and sufur pieces were combined with flux to accelerate mass transfer, resulting in several microns in size crystals. While these methods successfully achieved the desired crystal sizes, they pose a risk of leaving behind chlorine or iodine impurities in the growing crystals due to the high affinity of alkaline earth metals for halides. This could impact the material's intrinsic properties, which are not yet fully understood.

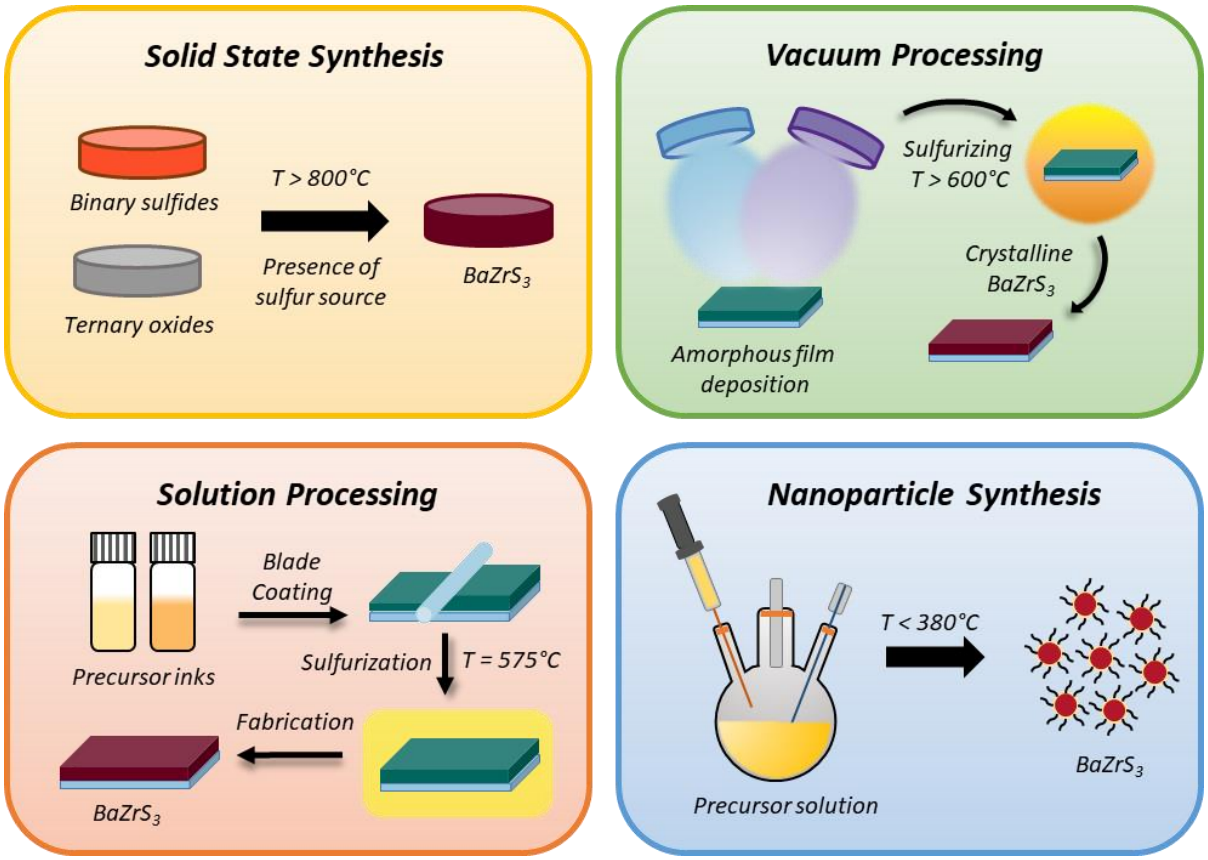

Figure 6. Schematic illustrating the various synthesis methods used for the preparation of $BaZrS_3$ and related compounds.

In an attempt to create dense pellets of $BaZrS_3$, Filippone et al. achieved high densification of $BaZrS_3$ powders at 450°C and 425 MPa by adding approximately two wt% iodine.[87] Their method, conducted under ambient conditions, did not lead to significant oxidation. Moreover, the boron-chalcogen method has previously been shown to convert various metal oxides into metal sulfides at moderate temperatures. Bystricky et al. extended this method to chalcogenide perovskites, using metal oxides and carbonates as precursors to form ternary compounds.[88] Notably, they obtained nearly phase-pure $BaZrS_3$ from oxide precursors at 600°C within a few hours of heat treatment using their flowing tubular furnace (see **Figure 7.a**). However, this method can introduce residual boron impurities into the target material. Although boron oxide is water soluble and can be removed with a light water wash, some water-insoluble boron oxysulfide impurities may remain.

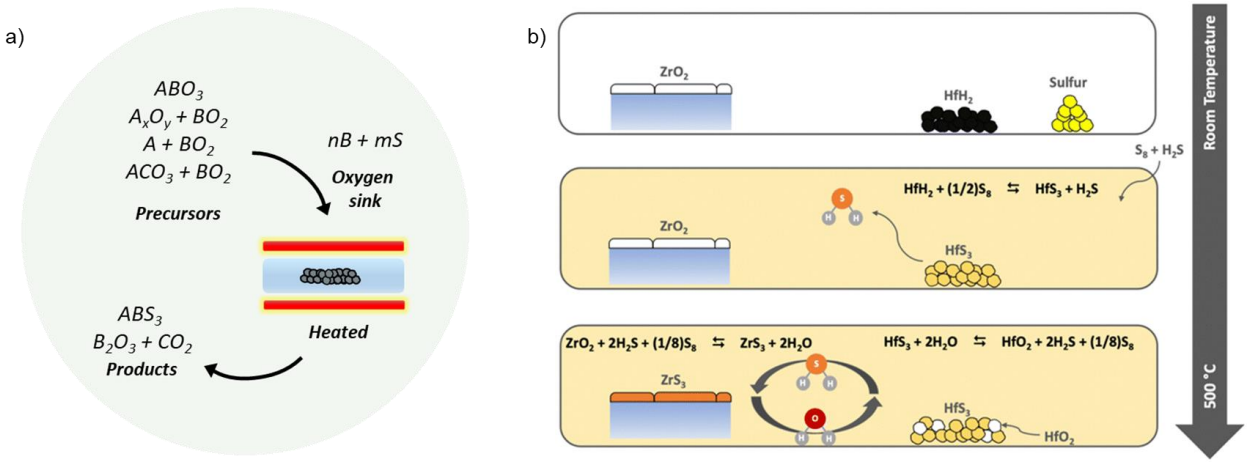

Figure 7. a) Schematic illustrating the conversion of binary and ternary oxide powders into ternary chalcogenides using boron and sulfur. a) Adapted with permission.[88] b) Schematic depicting the conversion of ZrO_2 into ZrS_3 using HfH_2 and sulfur. b) Reproduced with permission.[73] Copyright 2023, Royal Society of Chemistry.

In another significant contribution, Agarwal et al. used HfH_2 and sulfur in ampule sulfurization to create an H_2S-HfS_3 oxygen shuttle-sink system that converts oxide materials into sulfides at temperatures up to 600°C (schematic shown in **Figure 7.b**).[73] This approach is notable because Hf does not interact with the $BaZrS_3$ film, thus avoiding potential impurity contamination.

2.1.2. Thin Films

The Ravichandran, Koratkar, and Zeng groups have been pioneers in the thin-film synthesis and characterization of $BaZrS_3$, playing a pivotal role in showcasing its potential. Despite the potential of $BaZrS_3$, there have been few reports on its thin-film synthesis, and most of these involve high temperatures (>800-900°C), making them unsuitable for monolithic integration with the bottom layer in silicon solar cells. Successful thin-film synthesis of $BaZrS_3$ requires closely packed, oriented grains on an affordable substrate, potentially a type of glass that can withstand optimized temperatures. However, thin-film synthesis in the field of chalcogenide perovskites has faced numerous challenges due to barriers in the synthesis process. Operating at high temperatures can alleviate some of these challenges, but the drawbacks

of high-temperature methods in solar cell fabrication necessitate learning from these methods to inform the development of lower-temperature alternatives.

In recent notable advancements, the Jaramillo group at MIT successfully grew $BaZrS_3$ films on $LaAlO_3$ substrates using molecular beam epitaxy with an atomically sharp interface. **Figure 8.a** shows the lattice constants of commonly available commercial substrates and chalcogenide perovskites. They deposited thin films using elemental Ba and Zr alongside H_2S gas with the substrate temperature maintained at 900°C.[89] The films grew through two different mechanisms: buffered epitaxy, which creates a specific interface layer to alleviate strain, and direct epitaxy, in which the layers rotate to align despite significant differences in lattice size between the oxide and sulfide perovskites (shown in **Figure 8.b**). However, the epitaxially grown films exhibited planar defects, including antiphase boundaries, as demonstrated in **Figure 8.c**. Nonetheless, this method holds the potential for tuning the structure of sulfide perovskites and investigating the resulting properties. The group also expanded this technique to become the first, and currently the only, method to synthesize $BaZr(S,Se)_3$ films.[90]

Previously, Ravichandran group developed epitaxial $BaZrS_3$ thin films using pulsed laser deposition (PLD) on $LaAlO_3/SrLaAlO_4$ substrates (see **Figure 8.d**).[72] They employed $BaZrS_3$ as the target material and deposited films with a background of H_2S-Ar, depositing films in a single step at relatively low temperatures of 700-850°C. The significant variations in vapor pressure between the cations and sulfur source presented challenges, which their approach sought to address. While the films displayed epitaxial qualities near the film-substrate interface (as can be seen in **Figure 8.e**), they exhibited extended defects such as grain boundaries and Ruddlesden-Popper faults further from the interface. Surendran et al. also attempted to grow epitaxial films of quasi-1D $BaTiS_3$ using the same method, finding that the films exhibited weak epitaxial growth near the interface but were highly textured in the out-of-plane direction.[91]

The CS_2 sulfurization of oxide powders has proven successful in converting oxide powders into sulfides. However, the process is energy-intensive and typically requires high-temperature treatments. Koratkar group adapted CS_2 sulfurization to films by depositing oxide films using solution deposition and heating them with a flowing mixture of CS_2 and nitrogen at temperatures exceeding 1050°C (depicted in **Figure 9.a**).[62,92] This approach resulted in relatively uniform polycrystalline $BaZrS_3$ thin films on quartz substrates. While notable, this method may lead to some oxide impurities in the film and thus requires careful evaluation.

Similarly, Zeng group deposited $BaZrO_3$ film and amorphous Ba-Zr-S film using pulsed laser deposition (PLD) and converted them to $BaZrS_3$ using CS_2 sulfurization.[57,86,93] In another study, Dhole et al. used an aqueous solution route via polymer-assisted deposition (PAD) and sulfurized polymer-chelated cation precursor films with a flowing mixture of CS_2 and argon at 900°C.[94] Although their approach is significant, the resulting films exhibited a polycrystalline texture with nanometer-sized grains.

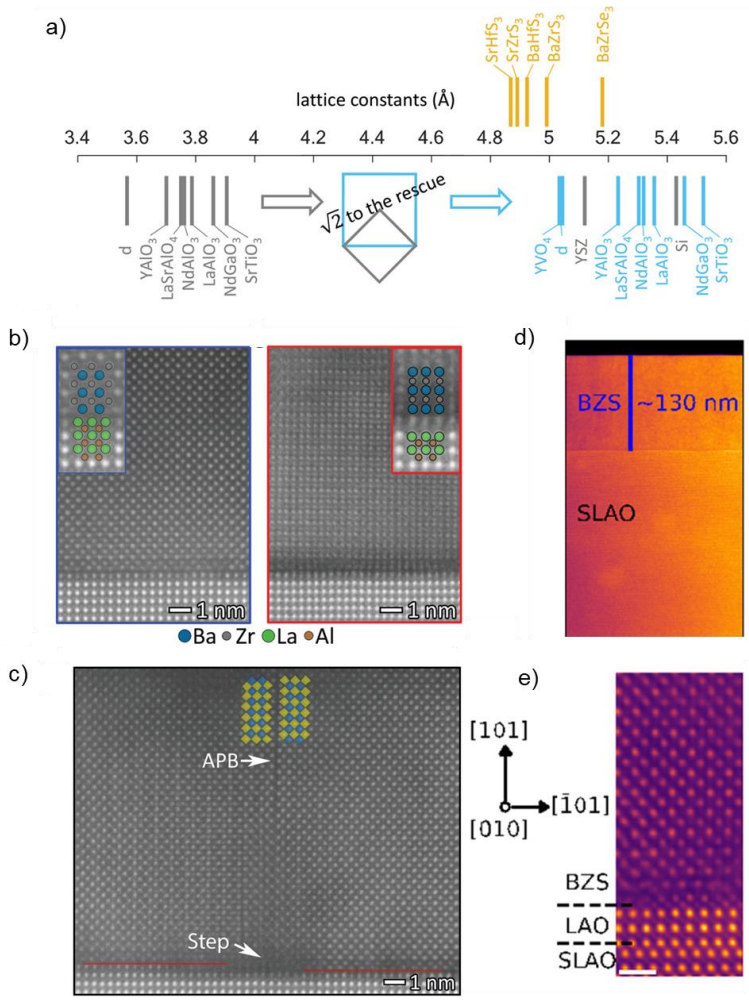

Figure 8. Epitaxially grown $BaZrS_3$. a) Comparison of pseudocubic lattice constants for chalcogenide perovskites and commercially available crystal substrates: d, diamond; YSZ, yttria-stabilized zirconia. Orange represents selected chalcogenide perovskites, gray denotes pseudocubic lattice constants of commercially available substrates, and blue indicates pseudocubic lattice constants scaled by a factor of sqrt 2. b) HAADF STEM images of a $BaZrS_3$ film grown on an $LaAlO_3$ substrate, showing two distinct epitaxial growth modes: b1) the predominant mode with pseudocubic edges aligned (growth mode M1), and c1) the rotated cube-on-cube mode with direct bonding (growth mode M2). Insets display magnified images with overlaid atomic species. c) STEM HAADF images revealing planar defects, including antiphase boundaries located at substrate step edges. Yellow and blue squares denote dimmer (Zr/S) and brighter (Ba) atom columns, respectively, adjacent to the antiphase boundary. Atom columns associated with growth mode M2, which may nucleate at substrate steps, are also faintly visible in the left-center region of the image. a), b) and c) Reproduced with permission.[89] Copyright 2021, Wiley. d) HAADF image of $BaZrS_3$ (BZS) film grown on an SLAO substrate, along with an image showing the polycrystalline nature of the BZS film. e) Atomic-resolution HAADF images of the BZS/SLAO interface, indicating the orientation of the BZS film in this region. d) and e) Reproduced with permission.[72] Copyright 2021, American Chemical Society.

While CS_2 sulfurization is a more common method for converting oxide films into ternary sulfides, H_2S sulfurization has also been explored in some studies. Marquez et al. sulfurized their amorphous Ba-Zr-O films at temperatures ranging from 700-1000°C under a continuous flow of 5% H_2S, finding increased crystallinity and sulfur content at higher temperatures.[68] However, the sulfurized films contained notable oxide impurities along with ternary $BaZrS_3$, with the sulfur content reaching a maximum of 0.85 S at%/(S

at% + O at%). They also reported that no solid solution of $BaZrO_3$ and $BaZrS_3$ was observed, and separate diffraction peaks for $BaZrO_3$ and $BaZrS_3$ were present.

Ramanandan et al. investigated the sulfurization mechanism of amorphous Ba-Zr-O films using H_2S treatment.[95] They found that the initial amorphous Ba-Zr-O film converted into crystalline $BaZrO_3$ and amorphous Ba-Zr-S at 700°C. The crystalline $BaZrO_3$ became amorphous at higher temperatures, forming an amorphous Ba-Zr-O-S phase from which crystalline $BaZrS_3$ nucleated alongside ZrO_2 at temperature increased above 900°C (see **Figure 9.b**). Their study suggests that the diffusion of sulfur-containing species is the rate-limiting step, necessitating high-temperature synthesis. It also highlights that low partial pressures of H_2S may not completely sulfurize the oxide film in a reasonable time due to slow kinetics. A mixture of H_2 and H_2S could be tested, as H_2 could aid in removing oxides while H_2S sulfurizes the film. However, concentrations of H_2S exceeding 4.3% in air become flammable and pose a safety hazard, so proper protocols must be followed.

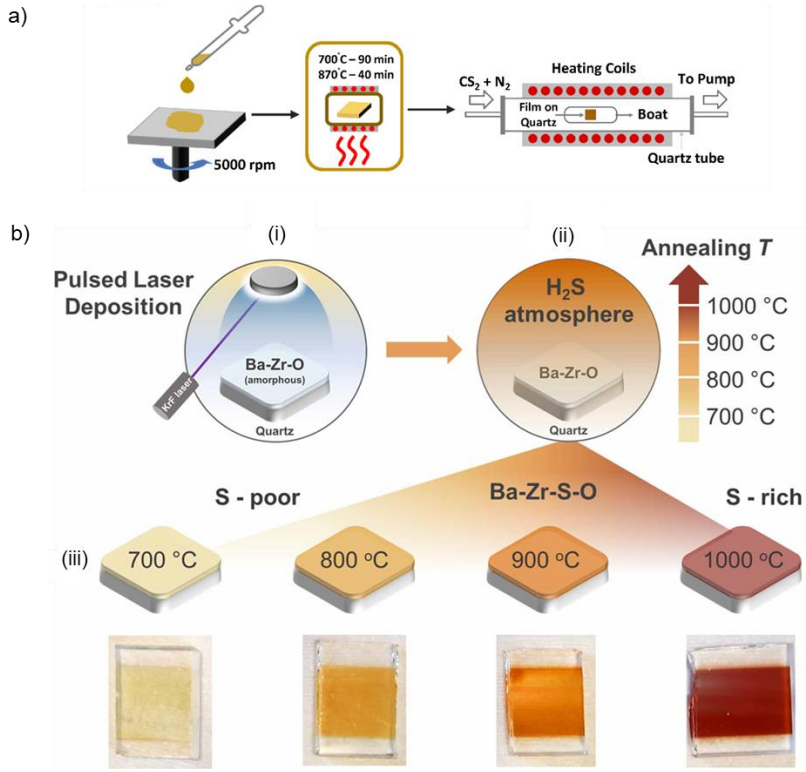

Figure 9. Conversion of Ba-Zr-O into $BaZrS_3$ at temperatures exceeding 900°C. a) Schematic illustrating the synthesis of $BaZrS_3$ film from an oxide precursor film, which is sulfurized in a CS_2 environment. a) Reproduced with permission.[96] Copyright 2021, American Chemical Society. b) Schematic depicting the synthesis of $BaZrS_3$ film from a pulsed laser deposited amorphous Ba-Zr-O film, followed by sulfurization with H_2S. b) Reproduced with permission.[95] Copyright 2023, IOP Science.

In a notable achievement, Comparotto et al. synthesized $BaZrS_3$ films by annealing amorphous Ba-Zr-S films, initially deposited via physical vapor deposition (PVD) at varying temperatures starting at 600°C. They found that the phase purity of $BaZrS_3$ films improved as annealing temperatures increased to 900°C, after which secondary oxide phases were observed at 1000°C. [97]

All the above methods relied on a mixed precursor film to synthesize BaZrS3. In an alternative approach, Freund et al. proposed a bilayer strategy in which they deposited a BaS layer onto zirconium foil and then sulfurized it in a flowing sulfur vapor environment at temperatures below 500°C.[98] However, this process resulted in the formation of BaS_3 film without the nucleation of ternary $BaZrS_3$, potentially due to surface oxidation of the Zr foil or diffusion limitations at the operating temperatures, which prevented the reaction of BaS_3 with Zr to form a ternary phase. Similarly, Jamshaid et al. applied a 300-600 nm layer of BaS onto a zirconium layer on a SiC substrate and sulfurized it under flowing sulfur at 1000°C, resulting in $BaZrS_3$ nucleation.[99]

Overall, these high-temperature methods provide valuable insights into the reactivity of various sulfur sources in converting oxides into sulfides. They also emphasize the challenges of sulfurizing highly stable oxide phases and underscore the need for using more reactive precursors to achieve faster kinetics and complete conversion.

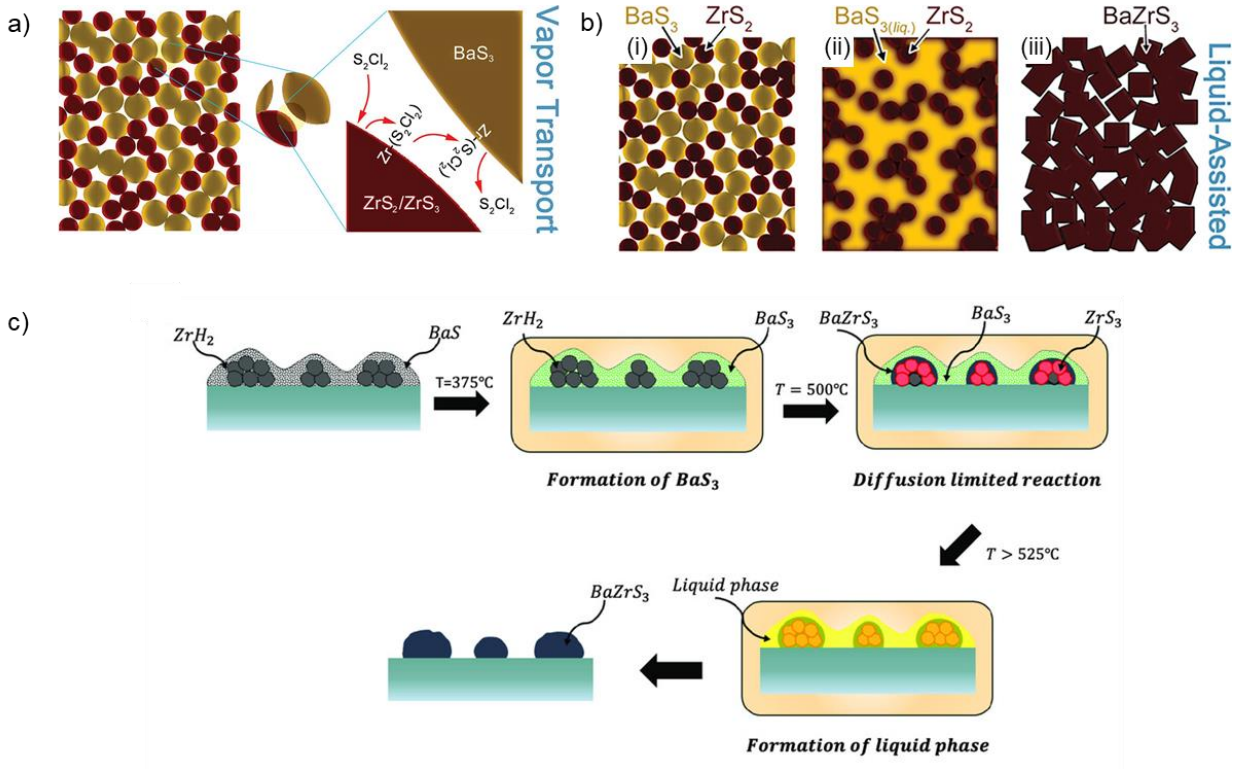

Figure 10. Schematic illustrating the working principles of: (a) S_2Cl_2 vapor transport agent, (b) BaS_3 liquid flux, and (c) BaS_x (x>3) liquid flux. a) Reproduced with permission.[100] Copyright 2023, American Chemical Society. b) Reproduced with permission.[101] Copyright 2023, Wiley.

2.2. Low-Temperature Synthesis

2.2.1. Flux-assisted solid-state synthesis

As noted earlier, most initial studies on $BaZrS_3$ synthesis involved high temperatures (>900°C) to produce bulk powders and thin films. The necessity for high temperatures was driven by using highly stable precursors such as oxides and carbonates, followed by sulfurization with CS_2 and H_2S. In many cases, the lack of flux resulted in slow mass transfer and required prolonged high-temperature reactions. It is essential

to recognize that while a compound may be thermodynamically stable compared to binary compounds at lower temperatures, it may still require annealing at higher temperatures to overcome kinetic barriers. Introducing a liquid flux, a transport agent, or a sulfur source can help lower kinetic barriers, facilitating faster synthesis at lower temperatures.

Wang et al. achieved a notable milestone by synthesizing $BaZrS_3$ at 500°C using a $BaCl_2$ flux in the presence of excess sulfur, representing the lowest reported temperature for producing phase-pure $BaZrS_3$ in bulk form.[102] Yang et al. later elucidated the mechanism of this reaction, explaining that sulfur interacts with chlorine from $BaCl_2$ to form S_2Cl_2 vapor, which acts as a transport agent and reduces the synthesis temperature. Confirming their hypothesis, they sealed binary sulfide precursors in an ampule with S_2Cl_2 liquid and reacted them at 500°C for 3 hours, successfully producing phase-pure $BaZrS_3$ (see **Figure 10.a**).[100] Similarly, Ravi et al. synthesized $BaZrS_3$ nanopowder using BaS, Zr, and stoichiometric sulfur at 600°C with the assistance of an I_2 transport agent.[65] Despite the benefits of lowering the synthesis temperature, both S_2Cl_2 and I_2 may introduce chlorine and iodine impurities, respectively, which could adversely affect the intrinsic properties of emerging semiconductors that are not yet fully understood. We performed thermodynamic calculations to validate this hypothesis, confirming that barium possesses one of the highest affinities for halide atoms among all elements in the periodic table.[103]

An ideal flux would consist of the same elements that form the desired compound, minimizing the potential for unwanted impurities. In this context, Vincent et al. identified a liquid flux of BaS_x ($x > 3$) that forms at temperatures above 525°C in a saturated sulfur environment, suitable for synthesizing $BaMS_3$ compounds.[101] They demonstrated the efficacy of this method on thin-film samples prepared using a hybrid precursor solution-processing route previously established by the Agarwal group[74], verifying the formation of a liquid BaS_x flux that reacted with in-situ generated ZrS_3 from ZrH_2, enabling the nucleation of $BaZrS_3$ within 5 minutes at 575°C (see **Figure 10.c**). They further applied this approach to the bulk solid-state synthesis of $BaZrS_3$ using BaS, ZrS_2, and excess sulfur, achieving synthesis within 15 minutes at 575°C. This starkly contrasts with previous solid-state reactions at temperatures above 900°C over several hours to days.

Building on these advances, Yang et al. suggested that BaS_3 could act as a liquid flux in the synthesis of $BaMS_3$ compounds, as BaS_3 melts between 540°C and 560°C. However, according to the Ba-S phase diagram, BaS_3 dissociates into BaS_2 and a sulfur-rich BaS_x at 554°C.[104] Thus, it is likely that BaS_x provides the actual liquid flux. Interestingly, they loaded large amounts of stoichiometric BaS_3 and ZrS_2 into an ampoule and heated the mixture to 540°C, forming $BaZrS_3$ within 5 minutes (as shown in **Figure 10b**). During this process, BaS_3 likely dissociated into BaS_2 and then into BaS, creating a saturated sulfur environment at 540°C while simultaneously providing a BaS_x liquid flux, which accelerated the growth of $BaZrS_3$. [100]

In a recent noteworthy report, our group demonstrated that selenium can also provide a liquid flux and lower the synthesis temperatures of $BaMS_3$ compounds.[105] Using an excess of selenium liquid flux, we successfully synthesized $BaMS_3$ compounds at 575°C starting from binary metal sulfide precursors. Although small amounts of $BaSe_3$ impurities were observed, they were found to be water-soluble. Consequently, a slight water wash of the synthesized powder resulted in seemingly phase-pure $BaMS_3$ compounds.

Overall, these low-temperature methods have significantly advanced the research on $BaMS_3$ compounds and paved the way for synthesizing them into thin films at lower temperatures.

2.2.2. Molecular precursor approaches: Group 4 binary and ternary perovskite synthesis

While high-temperature methods have been instrumental in experimentally validating the properties of $BaMS_3$ compounds as predicted by computational studies, their practical application in photovoltaics hinges on successfully fabricating low-temperature thin films while preserving their desirable properties. Among various techniques, solution processing is generally regarded as a low-temperature approach for thin film fabrication.[79,106,107] The success of halide perovskites is attributed, in part, to their facile solution processability at low temperatures. Solution processing has already been employed in the successful synthesis of several chalcogenide semiconductors, including $Cu(In,Ga)Se_2$, $Cu_2ZnSnSe_4$, and Sb_2Se_3, among others, resulting in device efficiencies comparable to those achieved through vacuum processing methods.[79,108–111] However, the adaptation of solution processing for chalcogenide perovskites has encountered challenges due to the strong affinity of alkaline earth metals to halides, the high oxophilicity of early transition elements, and the limited solubility of pure metals and metal sulfides in commonly used sulfide solution chemistries.

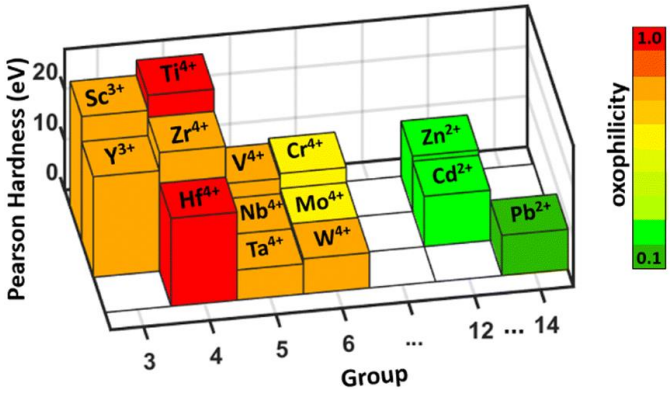

Figure 11. Plot showing the Pearson hardness and oxophilicity of common transition elements. Reproduced with permission.[81] Copyright 2023, Royal Society of Chemistry.

Kepp proposed an oxophilicity scale, which is a relative measure of an element's affinity for oxygen compared to the most oxophilic element in the periodic table.[82] Zilevu et al. noted that group IV elements rank among the most oxophilic elements in the periodic table with the highest oxophilicity, readily oxidizing upon exposure to air and moisture (shown in **Figure 11**).[81] Pearson hardness is another parameter that accounts for the high oxophilicity of early transition metals. It is derived from the hard and soft acids and bases (HSAB) theory, which states that hard acids, such as cations with small size and high charge, preferentially bond with hard bases, which are typically anions with small size, high charge, and high electronegativity. As a result, hard acids (early transition metals) exhibit a strong affinity for hard bases (such as oxygen), explaining the high oxophilicity of early transition elements (see **Figure 11**). This oxophilicity poses a significant challenge when dealing with molecular precursors, as their susceptibility to interaction with oxygen and moisture increases, leading to the formation of undesired oxides. Addressing this issue, Agarwal et al. introduced the aforementioned HfS_3-H_2S shuttle system to eliminate secondary oxides from molecular precursor films during sulfurization.[73] In their approach, they sulfurized the Ba-Zr-O film with excess sulfur in the presence of HfH_2. HfH_2 reacted with sulfur vapor, generating HfS_3 and in-

situ H_2S gas. The produced H_2S gas then reacted with Ba-O and Zr-O species in the film, forming Ba-S and Zr-S species while releasing H_2O. The generated H_2O was transported to HfS_3, leading to the formation of HfO_2 and the regeneration of H_2S. Due to the discrepancy in oxophilicity between Hf and Zr, oxygen was effectively transferred from the Ba-Zr-O film to HfS_3. Concurrently, the surplus sulfur vapor in the film facilitated the production of BaS_x liquid flux, reducing the diffusion barrier between Ba and Zr species and promoting rapid nucleation and growth of $BaZrS_3$ grains. This HfS_3-H_2S shuttle has been employed in the low-temperature, oxide-free, solution-processed synthesis of $BaZrS_3$ (**Figure 7b**).

Metal chlorides are commonly used as precursors in the solution-processed synthesis of other chalcogenide semiconductors.[78,112] However, we previously observed an abundance of residual crystalline alkaline earth metal chloride impurities in the film following the dissolution of alkaline earth metal chlorides in N, N-Dimethyl Formamide – Thiourea chemistry, annealing on a hot plate, and sulfurization in a sulfur environment.[113] This phenomenon likely stemmed from the greater stability of metal-chlorine bonds compared to metal-sulfur bonds for alkaline earth metals at operational temperatures. This is particularly interesting, as Yang et al.[100] used S_2Cl_2 as a vapor transport agent to synthesize $BaZrS_3$. We believe the key is to maintain a much lower molar fraction of chlorine-containing species to prevent the significant formation of Ba-Cl compounds, which could interfere with the formation of $BaZrS_3$.However, existing literature on other chalcogenide semiconductors advocates using impurity-free metal precursors in absorber material synthesis, as metal salt precursors may leave behind anionic impurities in the film, potentially altering its intrinsic properties uncontrollably.[76,114,115] Consequently, Pradhan et al. explored the dissolution of ZrS_2 and HfS_2 in various amine-thiol combinations, such as 1,2-ethanedithiol-1,2-ethylenediamine and 1,2-ethanedithiol-butylamine, among others, with no success.[113] Additionally, attempts using hydrazine chemistry to dissolve sulfides of various early transition metals including ZrS_2 and HfS_2 proved futile. Similar efforts with pure zirconium and hafnium nanoparticles in amine-thiol solutions yielded no positive outcomes.[113] Moreover, there is a dearth of reports on the successful dissolution of pure alkaline earth metals and their binary sulfides, raising uncertainty about their compatibility with common sulfide chemistries or the extent of rigorous testing. Despite these challenges, one study noted the co-dissolution of BaS alongside Cu_2S and SnO in an ethanedithiol-ethylenediamine mixture at 60°C for 11 days.[116] However, whether BaS alone would dissolve in the amine-thiol mixture remains unclear, as subsequent research has not explored BaS dissolution. In a recent report, our group successfully dissolved BaS and SrS using a different solution chemistry, which will be discussed later.[105] In summary, common precursors utilized in the solution-based synthesis of chalcogenide semiconductors for the late transition and p metals face obstacles in synthesizing chalcogenide perovskites. It is worth noting that during the peer-review stage of this study, another work of ours was published, where we demonstrated a method to synthesize $BaMS_3$ compounds using single-phase metal chloride precursor solutions.[103] This approach leveraged the higher affinity of potassium for chlorine compared to barium, enabling the transfer of residual chlorine in the film to a potassium sink during the annealing process via an H_2S-HCl shuttle. This method effectively resulted in chloride impurity-free $BaZrS_3$. Readers are encouraged to refer to the publication for further details.

The reactivity of starting precursors plays a crucial role in determining the success and efficiency of material synthesis processes. Highly reactive precursors tend to undergo chemical reactions more readily, leading to faster kinetics and potentially more complete conversion to the desired product. This can result in shorter synthesis times and higher yields. Conversely, less reactive precursors may require longer reaction times or higher temperatures to achieve the desired transformation, and they may also yield lower product yields. Additionally, the reactivity of precursors can influence the formation of by-products or impurities during

the synthesis process. Therefore, selecting precursors with appropriate reactivity levels is essential for controlling the synthesis conditions and obtaining the desired material properties.

Focusing on precursor reactivity, our group utilized organobarium bis(pentamethylcyclopentadienyl)barium (Cp^*_2Ba) as the barium precursor, reacting it with branched primary thiol 2-methyl-2-propanethiol to form $Ba(SC(CH_3)_3)_2$, which were found to be readily soluble in primary amines like propylamine and butylamine.[74] However, it remains unclear whether other primary and secondary thiols would react similarly with Cp^*_2Ba to form soluble thiolate species. It is plausible that the branched thiol aided solubility in less polar amine solvents. Further experiments are needed to confirm this hypothesis. Turnley et al. also employed ZrH_2 as the zirconium precursor, suspending it in a barium solution in butylamine and sonicating it to create a uniform suspension for depositing Ba-Zr precursor films.[74] The choice of zirconium precursor is somewhat peculiar, given the availability of more common metal-organic precursors for zirconium used in chemical vapor deposition processes. The possible reason for not using a metal-organic precursor may be attributed to zirconium's oxophilicity, as metal-organic species are highly reactive and prone to oxide formation. The Zr-H bonds are relatively stable and do not oxidize immediately upon air exposure. Using the hybrid precursor method, the solution was drop-cast onto a glass substrate and then sulfurized at 575°C for 2 hours in a borosilicate ampule (schematic shown in **Figure 12.a**). Subsequently, we followed a similar method and synthesized $BaZrS_3$ in as little as 5 minutes at 575°C with excess sulfur. It was proposed that the drop-cast film formed a mixture of BaS and ZrH_2, which upon sulfurization with excess sulfur, transformed into BaS_x liquid and ZrS_3, facilitating rapid $BaZrS_3$ synthesis. While both studies demonstrated $BaZrS_3$ synthesis at moderate temperatures, the hybrid precursor route yielded non-contiguous thin films.[101] A potential approach to contiguous films could involve functionalizing the surface of ZrH_2 nanoparticles to achieve colloidal stability in the same bulk solvent as the soluble barium precursor, albeit no reports on this have surfaced yet, making it an area worthy of exploration.

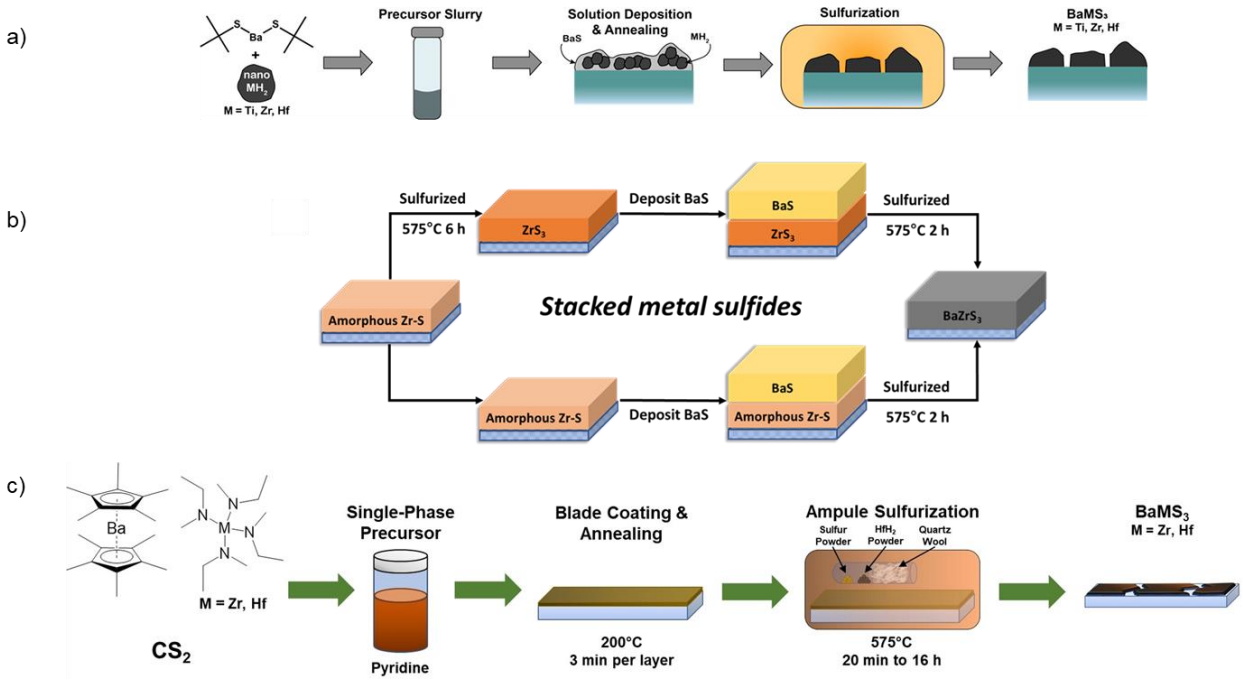

Figure 12. Schematic representation of the synthesis of solution-processed $BaMS_3$ (M = Ti, Zr, Hf) films. a) Synthesized from a precursor slurry containing soluble barium thiolate and suspended transition metal hydride precursors. Reproduced with permission.[74] Copyright 2022, American Chemical Society. b) Synthesized from a stacked precursor film of BaS and transition metal sulfides. Reproduced with permission.[105] Copyright 2024, Royal Society of Chemistry. c) Synthesized from soluble barium dithiocarboxylate and transition metal dithiocarbamate precursors. In all cases, the precursor films underwent a sulfurization step in a sulfur-rich environment to induce the crystallization of the ternary chalcogenides. Reproduced with permission.[117] Copyright 2023, Wiley.

In other noteworthy synthesis methods from our group, we reacted propylamine with CS_2 to form propyldithiocarbamic acid and used pyridine as a buffer solvent to dissolve the acid. This highly reactive dithiocarbamic acid species formed soluble complexes with BaS and SrS at room temperature, resulting in fully dissolved molecular precursor inks.[105] While ZrS_3 could not be dissolved, it was suspended in pyridine and sonicated to break down the smaller flakes, creating a stable suspension. The BaS and ZrS_3 solutions in pyridine were mixed to create a solution containing both barium and zirconium sulfide precursors. Upon coating on a glass substrate and sulfurization, this solution yielded phase-pure $BaZrS_3$, marking the first report of synthesizing $BaZrS_3$ using metal sulfide precursors at lower temperatures. In another method, we created a bilayer stack of BaS and ZrS_3 from the molecular precursor inks on a substrate. The ZrS_3 was synthesized from the molecular precursor solutions utilizing zirconium halide precursors, and the stacked film was sulfurized in a sulfur environment, accessing BaS_x liquid flux and forming $BaZrS_3$ (see **Figure 12.b**). This method represents the first synthesis of $BaZrS_3$ using Zr halide precursors.[105]

In a significant breakthrough, our group employed tetrakis amide precursors of zirconium as the metal source for synthesizing $BaZrS_3$. These precursors are commercially available and widely used in chemical vapor deposition processes.[117] Previously, Thompson demonstrated the utility of these precursors in his thesis, employing various sulfur sources such as carbon disulfide and ethyl isothiocyanate to form single-source metal-sulfur bonded precursors, ultimately synthesizing ZrS_2 via chemical vapor deposition.[118] Pradhan et al. utilized $Zr[N(MeEt)_4]$ as the zirconium precursor and inserted carbon disulfide in the metal amide bond to form zirconium dithiocarbamate species. Additionally, carbon disulfide was inserted into Cp^*_2Ba to generate a barium dithiocarboxylate precursor. While barium dithiocarboxylate proved soluble in pyridine, independent dissolution of tetrakisamido ethylmethylzirconium dithiocarbamate in pyridine was not feasible. However, co-dissolving barium and zirconium precursors in pyridine along with CS_2 resulted in the first reported fully dissolved molecular precursor ink at room temperature for the synthesis of $BaZrS_3$. However, similar success was not achieved with the dimethyl amide precursor of zirconium. The fully dissolved ink was then blade-coated and annealed on a hot plate, resulting in an amorphous matrix of Ba-Zr-S. Subsequent sulfurization with excess sulfur in the presence of HfH_2 at 575°C for as little as 20 minutes yielded $BaZrS_3$, marking a significant improvement over previous high-temperature synthesis methods (>900°C) (schematic shown in **Figure 12.c**). Pradhan et al. also observed increased crystallinity of $BaZrS_3$ grains, as indicated by the reduced full width at half maximum (FWHM) of the 25.2 peak, with longer sulfurization times. [117] Although not explicitly stated, the localized formation of BaS_x liquid flux likely facilitated $BaZrS_3$ nucleation and grain growth. Despite these advancements, further refinement is needed to address irregularly oriented agglomerates of cubic-shaped crystals and excessive carbon content known to influence grain size and composition during growth. Rigorous optimization of annealing parameters, sulfur amount, and substrate choice may be necessary to produce device-grade continuous films.

These reports have played a pivotal role in achieving thin films of $BaZrS_3$ via solution processing. However, several challenges persist. All the aforementioned methods relied on BaS_x liquid flux for crystal growth, resulting in rapid, uncontrolled growth and the formation of large micron-sized grains (see **Figures 13.a and 13.b**). Thus, there is a pressing need to develop strategies to mitigate uncontrolled growth. During the revision stage of this work, another manuscript from our group was published, introducing several novel methods for synthesizing $BaZrS_3$ thin films, some of which successfully produced contiguous films.[119] Notably, one method utilized metal thiolate precursors to synthesize $BaZrS_3$ without the need for HfH_2, and also prevented the overgrowth of $BaZrS_3$ grains. Further details can be found in the published article. Nonetheless, several challenges remain to be addressed. Due to $BaZrS_3$'s high absorption coefficient, a thin film as thin as 200 nm should suffice to fully absorb incoming light. However, the solution methods discussed have so far yielded films several microns thick, that could potentially impede the collection of light-generated charge carriers and impact performance of fabricated devices. Moreover, these films were grown on non-conductive substrates, necessitating further efforts to replicate them on conductive substrates. This endeavor presents challenges, as the metal back contacts used in many device architectures may sulfurize to their sulfides when exposed to prolonged sulfur environments. Consequently, additional research is required to identify a suitable, cost-effective, conductive back contact capable of withstanding prolonged exposure to sulfur environments.

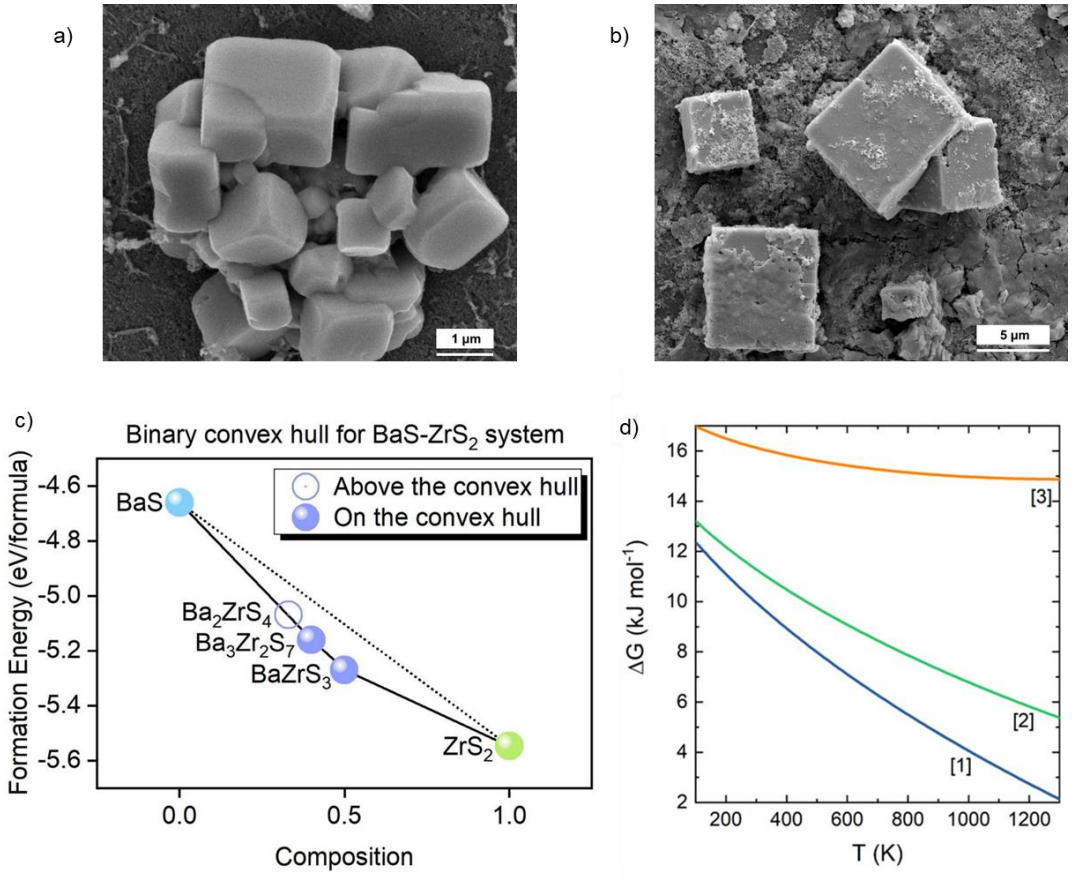

Figure 13. Uncontrolled growth of crystals synthesized from solution-processing routes and phase stability of $BaZrS_3$. Scanning electron microscope image of $BaZrS_3$ synthesized from a) a mixed slurry of BaS-ZrS_3 and b) bilayer stack of BaS-ZrS_3 and sulfurized in the presence of HfH_2-sulfur at 575°C. a), b) Reproduced with permission.[105] Copyright 2024, Royal Society of Chemistry. c) Binary convex hull for the BaS-ZrS_2 system. c) Reproduced with permission. [48]

Copyright 2023, Wiley. d) Gibbs free energy (ΔG) plotted as a function of temperature. ΔG is calculated for the decomposition of $BaZrS_3$ into: 1) $Ba_4Zr_3S_{10}$ and ZrS_2; 2) $Ba_3Zr_2S_7$ and ZrS_2; 3) Ba_2ZrS_4 and ZrS_2. For comparison, all materials are assumed to be in the I4/mmm phase. a) Reproduced with permission. [120] Copyright 2023, Elsevier.

2.2.2.1. Role of sulfur pressure:

BaS_x/BaS_3 liquid flux has been a crucial intermediate in lowering the synthesis temperatures of $BaZrS_3$. However, achieving these liquid fluxes requires maintaining a significantly high sulfur pressure. Our group's previous work has reportedly used around 1 bar of sulfur pressure to form in situ liquid flux during the synthesis of $BaZrS_3$ from either binary sulfide powders or a molecular precursor film.[101] Kayatha et al. also confirmed through their calculations that high sulfur pressure in this range is necessary to obtain the BaS_3/BaS_x phase.[121] As synthesis pressures decrease, the crystallinity of the ternary material diminishes, as evidenced by the FWHM of the <121> peak. Reducing the sulfur pressure below 0.3-0.4 bar results in a mixture of $BaZrS_3$ and Ruddlesden-Popper phases (predominantly $Ba_3Zr_2S_7$), regardless of the starting Ba:Zr ratio. This phenomenon is explained by the limited presence of a liquid flux at these low pressures, leading to a sluggish reaction and metastable intermediate Ruddlesden-Popper phases at temperatures below 600°C. At even lower sulfur pressures, binary sulfides remain unreacted. [101] Kayastha et al. and Han et al. also suggested that at high temperatures, $BaZrS_3$ and Ruddlesden-Popper phases have similar Gibbs free energies of formation, potentially resulting in a mixture of these phases regardless of the initial Ba:Zr ratios [48,120] Han et al. demonstrated that $Ba_3Zr_2S_7$ and $BaZrS_3$ lie on the convex hull, indicating their stability (see **Figure 13.c**).[48] Previously, Li et al. also showed that $Ba_3Zr_2S_7$ is the most stable Ruddlesden-Popper phase in the Ba-Zr-S system.[27] However, Kayastha et al. found that $Ba_4Zr_3S_{10}$ has the lowest formation energy among all the Ruddlesden-Popper phases (shown in **Figure 13.d**). They confirmed this by mixing binary sulfides and heating them together at 900°C for 5 days, showing that a mixture of $BaZrS_3$ and $Ba_4Zr_3S_{10}$ formed irrespective of the metal ratios.[120] These Ruddlesden-Popper phase impurities can become a bottleneck due to their similar X-ray diffraction patterns to $BaZrS_3$. Therefore, a secondary structural characterization technique, such as Raman spectroscopy, needs to be employed. This discussion underscores the need to maintain sufficiently high sulfur pressure during synthesis to achieve rapid synthesis and avoid the formation of Ruddlesden-Popper phases. However, high sulfur pressure could also result in the formation of sulfur interstitials, which have been shown to be low-energy deep defects for $BaZrS_3$.[122]

Moreover, our group's research shows that $BaZrS_3$ does not decompose into binary compounds under sulfur pressures up to 1 bar. [101] We also demonstrated that ZrS_3 can be used as a starting precursor for the synthesis of $BaZrS_3$ rather than being considered a decomposition product. Additionally, Kayastha et al.'s first-principles calculations predict that $BaZrS_3$ would not decompose into sulfur-rich binaries at sulfur pressures up to at least 100 bar. [121]

2.2.2.2. Challenges with molecular precursor routes for $BaMS_3$ compounds

Our group recently summarized the key challenges in the low-temperature, solution-processed synthesis of $BaMS_3$ compounds.[123] While we have successfully synthesized $BaMS_3$ compounds using fully dissolved molecular precursor inks and incorporating a second sulfurization step in a controlled sulfur environment, a gap remains in achieving grain nucleation directly after annealing the film on a hotplate. Several factors may hinder this, including excessive carbon, trace amounts of oxygen leading to the formation of amorphous metal oxysulfides, premature breakdown of metal-sulfur complexes forming an amorphous Ba-

M-S sulfide matrix, or rapid solvent evaporation causing premature nucleation of metal-sulfur complexes, which also result in an amorphous Ba-M-S sulfide matrix.

To address these issues, we developed the H_2S-HfS_3 oxygen shuttle-sink system to remove oxygen from the film during sulfurization. However, maintaining sufficient sulfur pressure is crucial to ensure phase-pure $BaZrS_3$ synthesis, as inadequate pressure can lead to Ruddlesden-Popper phase impurities. Additionally, the use of a liquid flux in low-temperature $BaMS_3$ synthesis has been effective in reducing mass transfer barriers and promoting crystal growth, but it has also led to uncontrolled, randomly oriented micron-sized grains with planar defects. This rapid growth can result in the entrapment of oxide impurities within the crystals. Controlling grain growth remains a key challenge that requires strategic approaches.

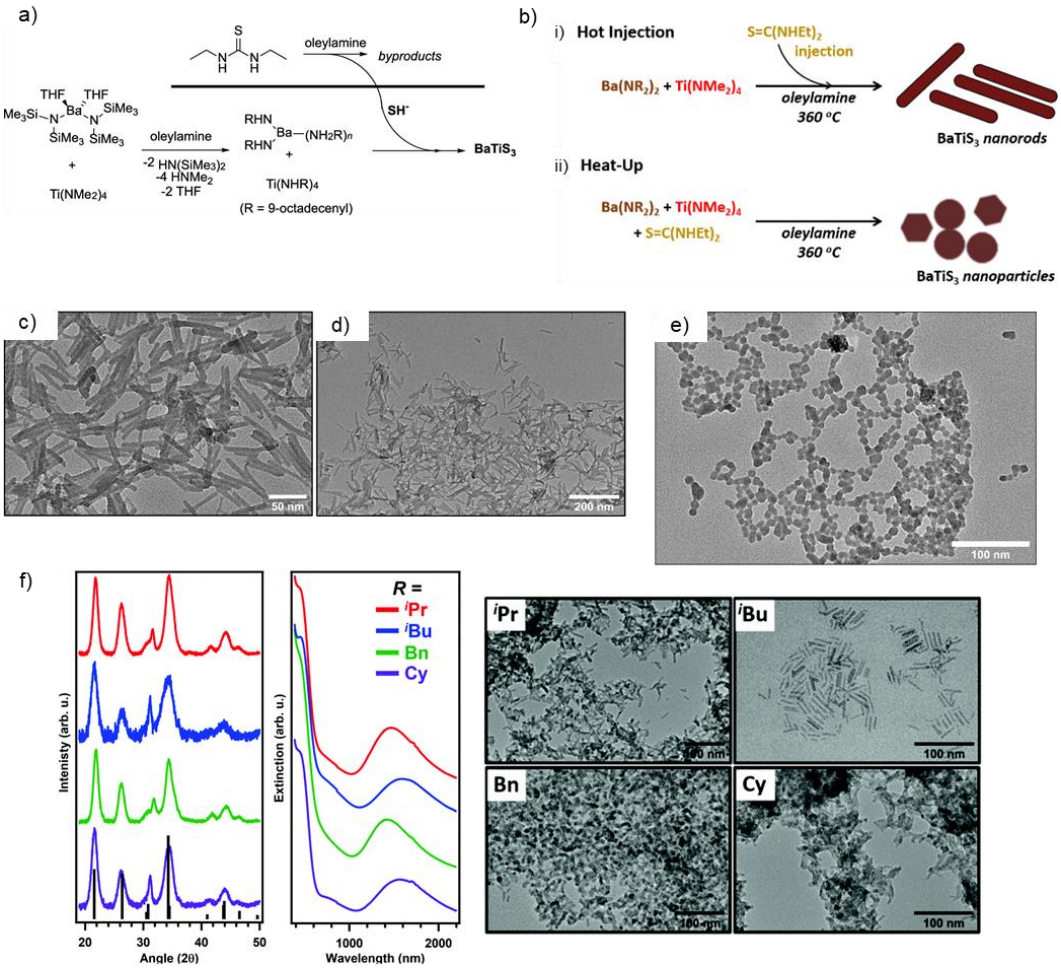

Figure 14. $BaTiS_3$ nanoparticles synthesis. (a) Reaction scheme for the synthesis of $BaTiS_3$ nanoparticles, (b) reaction conditions employed for the hot injection and heat-up synthesis of $BaTiS_3$ nanoparticles, (c) and (d) TEM images of nanoparticles synthesized using the hot injection method, (e) TEM image of nanoparticles synthesized using the heat-up method, (f) X-ray diffraction pattern and TEM images of $BaTiS_3$ nanoparticles synthesized from barium dithiocarbamate precursors with varying alkyl chains. a), b), c), d) and e) Reproduced with permission.[124] Copyright 2021, American Chemical Society. f) Reproduced with permission.[125] Copyright 2021, Royal Society of Chemistry.

Furthermore, substrate selection plays a critical role, as glass substrates often release cationic species during prolonged sulfurization, potentially leading to secondary phases in the film. While quartz may seem

appealing, it presents the opposite issue, as cations can diffuse into the quartz during annealing, as observed with Ba diffusion. Finally, while our H_2S-HfS_3 system effectively removes oxide impurities, it is less efficient in the presence of excessive moisture, as it interferes with the capacity of H_2S-HfS_3 system to remove oxygen present in the film. Therefore, careful handling is necessary to prevent moisture exposure to samples or ampoules before sulfurization.

Addressing these challenges is essential for developing high-efficiency optoelectronic devices from solution-processed $BaMS_3$ compounds.

2.2.3. Nanoparticle synthesis: Group 4 binary and ternary perovskite synthesis

Molecular precursor routes offer a straightforward method for synthesizing chalcogenide semiconductor films, yet there is potential for utilizing colloidally stable semiconductor nanoparticle solutions to deposit thin films. Nanoparticle inks afford greater flexibility in choosing device architectures for solar cells, underscoring their significance. Parameters such as ink concentration, particle size, morphology, and surface ligands can be adjusted to meet specific requirements. Additionally, varying synthesis temperatures, reaction times, and the synthesis procedure (e.g., hot injection vs. heat-up) may reveal intriguing features. Several high-efficiency chalcogenide solar cells have already been developed using nanoparticle inks, including $Cu(In,Ga)Se_2$ and $Cu_2ZnSnSe_4$.[126–129] However, challenges related to precursor dissolution, precursor purity, and the oxophilicity of early transition metals have rendered nanoparticle synthesis difficult for chalcogenide perovskites.

The initial instance of nanoparticle synthesis within the chalcogenide perovskite family involved the synthesis of $BaTiS_3$ nanoparticles utilizing reactive metal organoamide precursors. $BaTiS_3$ is known for its quasi-1D hexagonal structure, exhibiting distinct properties like optical anisotropy, mid-IR birefringence, and thermal transport characteristics.[30,91,130–132] Zilevu et al. indicated that controlling the morphology (nanoparticle versus nanorod) could be achieved by alternating between heat-up and hot injection methods during crystal growth (see **Figures 14.a and 14.b**). Furthermore, size regulation was attainable by adjusting reaction time and temperature, with a hot injection reaction at 360°C yielding nanorods with an aspect ratio of 8:1 (50 nm length, 6 mm width). Reactions were conducted in oleylamine, which with a boiling point of 364°C, provides a broad reaction temperature range. Although not explicitly demonstrated, the ligand on the nanoparticle surface may also influence the process. Oleylamine's π bond in its chain prevents chain folding and stacking, thereby averting agglomeration and facilitating stable suspensions.[133] To avoid undesired by-products, they employed reactive $Ba[N(SiMe_3)_2]_2(THF)_2$ and $Ti(NMe_2)_4$ metal precursors, combined with oleylamine and N,N′-diethylthiourea as the sulfur source. While testing various sulfur sources, such as elemental sulfur, carbon disulfide, thioacetamide, and different thioureas, nanocrystals were found to most readily synthesize with thioureas, known for their decomposition upon heating and liberation of H_2S, interacting with the metal precursors to form the desired compounds. Maintaining reaction conditions devoid of water, oxygen, or any oxygen-containing ligands was emphasized to prevent oxide impurity formation. In heat-up reactions, metal precursors, N,N′-diethylthiourea, and oleylamine were added to the reaction vessel and then heated to 360°C. Conversely, for hot injection reactions, metal precursors and oleylamine were heated to 360°C, while a preheated N,N′-diethylthiourea, and oleylamine solution at 60°C was injected into the reaction vessel. Despite testing different reaction temperatures, crystalline $BaTiS_3$ was not achieved below 290°C. However, the pXRD pattern of the synthesized nanorods slightly deviated from the reported bulk XRD pattern due to potential sulfur deficiency, resulting in a partial off-stoichiometric phase with a commensurate structure.[124] This structure, resembles that of Sr_xTiS_3, which

features two interpenetrating subcells based on TiS_3 and Sr lattices, causing additional peaks in the diffraction pattern and shifting the main peaks.[134] A clear difference in the morphology of $BaTiS_3$ nanoparticles grown using two different methodologies is evident in **Figures 14.c, d, and e**. Notably, the synthesized nanoparticles exhibited sufficient stability in air but degraded rapidly in water, potentially limiting their utility in water-based applications. Nevertheless, their air stability offers promise for utilization in optoelectronic applications.

Ingram et al. reported the synthesis of $BaTiS_3$ nanoparticles using single-phase precursors of barium and titanium dithiocarbamates.[125] The synthesis began with the preparation of barium N,N-dialkyl dithiocarbamate by forming a dithiocarbamate ion solution in water/ethanol through the combination of dialkylamine and carbon disulfide, followed by the addition of pure barium metal chunks. After stirring at room temperature for 30 minutes, the mixture was heated to 350°C for 30 minutes (where alkyl groups = isopropyl, isobutyl, benzyl, cyclohexyl), barium dialkyl dithiocarbamate formed in the solution. Subsequently, crystals were recrystallized by adding ether/tetrahydrofuran and dried under vacuum at 80°C to eliminate moisture and obtain anhydrous barium dithiocarbamate. Titanium dithiocarbamate species were obtained by introducing carbon disulfide to $Ti(NiPr_2)_4$, where carbon disulfide was inserted into the metal-amide bond to form dithiocarbamate species. The resulting barium and titanium dithiocarbamate precursors were co-added in a 2:1 molar ratio in an oleylamine solution and heated to 350°C to produce $BaTiS_3$ nanocrystals (See **Figure 14.f**). It was observed that excess Ba precursor was crucial for obtaining phase-pure $BaTiS_3$ nanocrystals and preventing TiS_2 impurities. However, the resulting nanorods exhibited poorer crystallinity compared to nanoparticles synthesized by Zilevu et al. The exact cause of this phenomenon is not fully understood but could stem from inherent impurities during barium dithiocarbamate synthesis, or the decomposition temperature of barium dithiocarbamate may not align with the ideal conditions for ternary $BaTiS_3$ synthesis. Additionally, some pXRD peaks were slightly shifted compared to the diffraction spectra of bulk $BaTiS_3$, indicating a sulfur-poor composition. While this method utilizes direct single-source precursors for $BaTiS_3$ synthesis, it offers less control over material properties compared to the hot-injection method previously developed by Zilevu et al. Nonetheless, this approach may hold promise for synthesizing $BaZrS_3$ nanocrystals.[125]

While $BaZrS_3$ has emerged as one of the most extensively studied chalcogenide perovskites, limited attention has been devoted to the direct nanoparticle synthesis of $BaZrS_3$, with only two reports available in the literature. Furthermore, both studies encountered challenges in producing colloidally stable nanoparticles, preventing the fabrication of $BaZrS_3$ films using such nanoparticles. The primary hurdle lies in effectively utilizing reactive metal precursors while maintaining oxygen and moisture-free conditions during synthesis. Addressing these challenges, Yang et al. employed metal dithiocarbamate precursors for $BaZrS_3$ nanoparticle synthesis. Barium dibutyl dithiocarbamate was synthesized from the reaction of $Ba(OH)_2$ with carbon disulfide and dibutylamine, while zirconium diethyldithiocarbamate was obtained by reacting $ZrCl_4$ with diethylamine and carbon disulfide. These dithiocarbamates were then added to oleylamine in a 1:1 metal ratio at a total concentration of 0.488 M. No additional sulfur source was necessary, as the thermal decomposition of the dithiocarbamates yielded metal-sulfur monomers. The solution was heated to 330°C and maintained for 18 hours to form $BaZrS_3$ nanocrystals (shorter reaction times of 30 minutes also resulted in $BaZrS_3$ nanocrystals). However, their powder X-ray diffraction (pXRD) pattern exhibited multiple impurity peaks that did not correspond to the perovskite crystal structure, which were attributed to zirconium-rich regions and oxide impurities (see **Figure 15.a**).[135] The TEM images reveal agglomerates of nanoparticles rather than distinct, isolated particles, indicating that the nanoparticles did

not disperse well in the solution (shown in **Figure 15.b**). The lattice spacing observed in the HRTEM image corresponded to $BaZrS_3$ (illustrated in **Figure 15.c**). Without STEM-EDX measurements, confirming the presence of zirconium-rich regions in the nanoparticles remains challenging, necessitating further investigation to accurately assign these peaks. Conversely, tighter control over oxygen and moisture exposure during nanoparticle synthesis could mitigate oxide impurities.

Similar to Yang et al., Zilevu et al. also synthesized $BaZrS_3$ nanoparticles, albeit using different precursors and sulfur sources. However, they encountered similar challenges with extra peaks in the diffraction pattern. Their method involved utilizing $Ba[N(TMS)_2]_2(THF)_2$ and $Zr[N(CH_3)_2]_4$ as the metal precursors, along with N,N-diethyl thiourea as the sulfur source. These precursors were combined in a 1:2:60 mole ratio to the dried oleylamine (shown in **Figure 15.d**). The reaction mixture was then heated to the desired temperature and maintained for 30 minutes. They observed additional peaks in the nanoparticles synthesized at temperatures around 275°C, which they attributed to a low-temperature phase. Upon increasing the reaction temperature to 365°C, they observed $BaZrS_3$ nanoparticles without structural distortions, indicating a high-temperature phase.[136] However, they encountered difficulties in consistently reproducing the high-temperature reaction. Variability in critical synthesis parameters, potentially due to the use of home-built setups relying on heating tape for temperature control, may contribute to this inconsistency. Thus, tighter control of synthesis parameters is necessary to ensure reproducibility when incorporating these nanoparticles into optoelectronic devices. Consistent with Yang et al., they also observed significant agglomeration of the nanoparticles, indicating poor dispersion (see **Figure 15.e**). Notably, Zilevu et al. found that the synthesized nanoparticles exhibited reasonable stability in air and water.[136]

Recently, our group published a study demonstrating a solution-based method for synthesizing impurity-free $BaZrS_3$ nanoparticles.[137] These nanoparticles exhibited no additional unassigned peaks previously observed by Zilevu et al.[136] and Yang et al[135] using heat-up synthesis method. While Yang et al.[135] attributed the extra peaks to impurities, Zilevu et al.[136] suggested that nanoparticles synthesized below 365 °C represented a distinct phase of $BaZrS_3$, which they termed low-temperature $BaZrS_3$. In our study, commercially available cyclopentadienyl barium and tetrakisethylmethylamido zirconium were utilized as zirconium precursors. During the standard heating procedure, these precursors were added to a round-bottom flask and reacted with a tenfold molar excess of CS_2 to form metal-sulfur-bonded intermediates. Subsequently, oleylamine was introduced as both a coordinating solvent and reaction medium. A portion of the oleylamine also reacted with the excess CS_2 in the flask to form oleyldithiocarbamate species. Heating this system to temperatures between 290–340 °C under a constant flow of argon yielded $BaZrS_3$ nanoparticles with additional peaks, similar to those previously reported in the literature. To address this issue, we hypothesized that rapid heating of the metal-sulfur-bonded precursors to temperatures significantly higher than 340 °C could produce phase-pure $BaZrS_3$ nanoparticles. To test this hypothesis, a hot-injection method was developed, marking the first application of this approach in the synthesis of chalcogenide perovskites. Using oleylamine as the primary solvent posed a challenge, as its excessive refluxing limited the reaction temperature to approximately 340 °C. To overcome this, mineral oil, consisting of long-chain alkanes, was employed, enabling the system to reach temperatures as high as 375 °C. For the hot-injection synthesis, mineral oil was used as the bulk solvent in the reaction flask and heated to 370–375 °C. Once the temperature stabilized, a slurry containing organobarium and metal-organic zirconium precursors in excess CS_2 and oleylamine was introduced into the flask via a Merlic adapter. This hot-injection method successfully and reproducibly synthesized phase-pure $BaZrS_3$ nanoparticles at the

lowest temperature reported in the literature. This breakthrough opens new avenues for exciting applications of $BaZrS_3$.

The same method was applied to synthesize $BaHfS_3$ nanoparticles. However, similar to earlier reports for $BaZrS_3$, the $BaHfS_3$ nanoparticles exhibited additional diffraction peaks, suggesting that a reaction temperature of 375 °C might still be insufficient for achieving phase-pure $BaHfS_3$. While we also synthesized other chalcogenide perovskites, such as α-$SrZrS_3$ and α-$SrHfS_3$, these materials fall outside the scope of this work. Readers are encouraged to consult our publication for further details.

Ravi et al. previously achieved a significant advancement by synthesizing $BaZrS_3$ nanocrystals at 600°C using the I_2 flux method initially developed by Niu et al. They functionalized the nanocrystal surfaces with N-methyl-2-pyrrolidinone to create a colloidally stable nanocrystal ink. Additionally, they capped the nanocrystals with non-polar oleylamine, resulting in a stable dispersion in chloroform (shown in **Figure 15.f**). The TEM image in **Figure 15.g** displays cubic crystals on the nanometer scale. This stable ink in chloroform was then used to coat a thin film of $BaZrS_3$, demonstrating a functional field-effect transistor.[65]

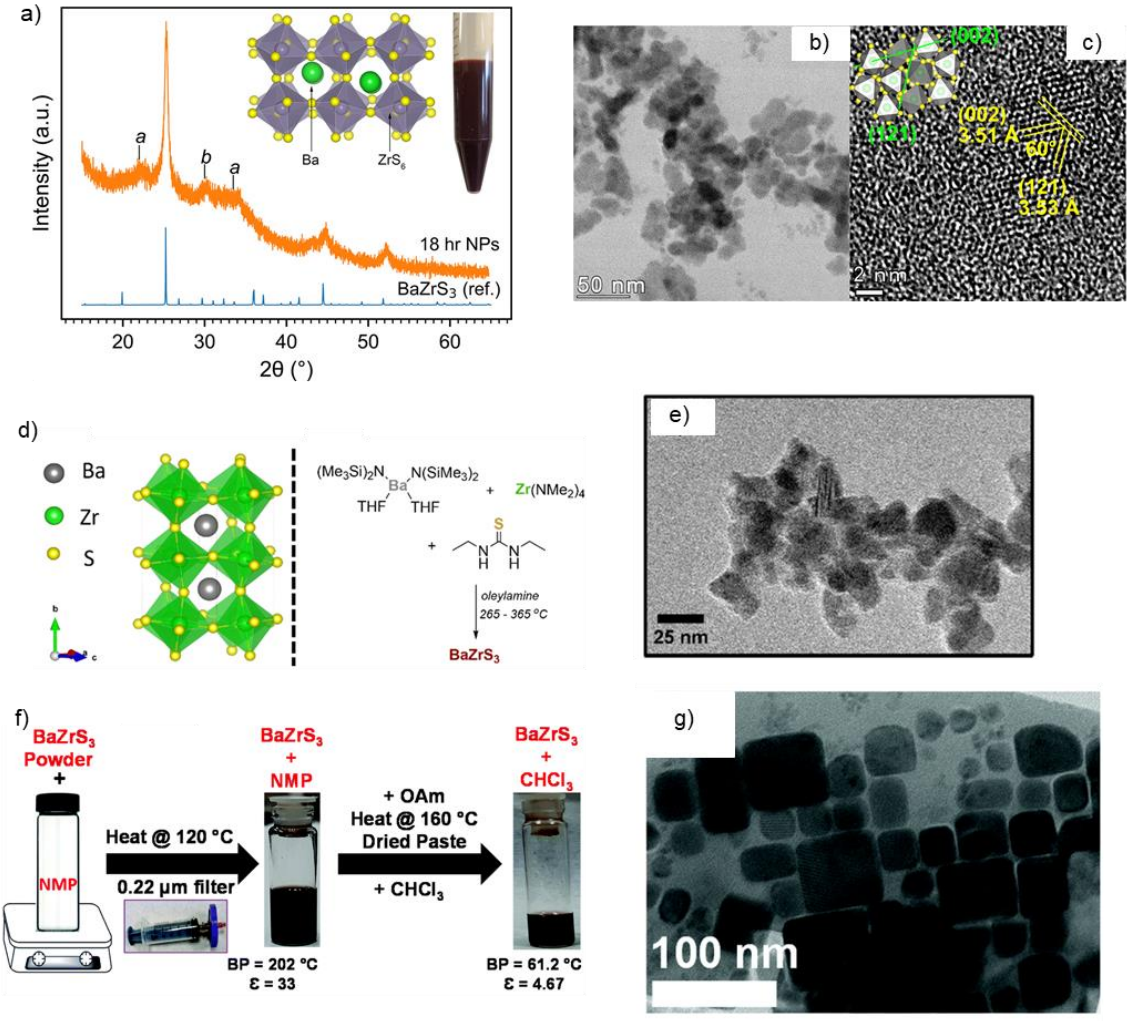

Figure 15. $BaZrS_3$ nanoparticles synthesis. a) X-ray diffraction pattern of $BaZrS_3$ nanoparticles synthesized from metal dithiocarbamate precursors, b) and c) TEM and HRTEM images of $BaZrS_3$ nanoparticles synthesized by Yang

et al.[135], d) reaction conditions used by Zilevu et al. [136] for synthesizing $BaZrS_3$ nanoparticles, e) TEM image of the synthesized nanoparticles, f) procedure for capping ligands on solid-state synthesized $BaZrS_3$ nanoparticles, g) TEM image of $BaZrS_3$ nanoparticles synthesized by Ravi et al.[65] a), b) and c) Reproduced with permission.[135] Copyright 2022, American Chemical Society. d) and e) Reproduced with permission.[136] Copyright 2022, Royal Society of Chemistry. f) and g) Reproduced with permission.[65] Copyright 2021, Royal Society of Chemistry.

Although substantial advancements have been achieved in synthesizing $BaZrS_3$ and hexagonal $BaTiS_3$ nanoparticles, further efforts are necessary to establish their colloidal stability in benign solvents. Additionally, exploring ligand exchange methods could enhance the attachment of desirable organic or inorganic ligands onto the surface of the nanoparticles. Efforts should be made to synthesize nanoparticles from cost-effective metal precursors such as metal acetylacetonates and metal halides. However, this process pose challenges due to the strong affinity of early transition metals for oxygen and alkaline earth metals for halides. Ravi et al.[65] reported attempts to synthesize $BaZrS_3$ nanoparticles from metal acetylacetonate and metal halide precursors but were unsuccessful in achieving ternary phases. Nonetheless, developing specific traps in solution that selectively react with these impurities could enable the phase-pure synthesis of ternary chalcogenides and should be pursued.

2.2.4. Vacuum-processed synthesis

While previously reported high- and low-temperature methods have been effective in synthesizing thin films of $BaZrS_3$, these methods often use non-conductive substrates, which limits their utility in optoelectronic applications. For efficient transport of charge carriers to and from the external circuit, smooth, contiguous semiconductor films must be deposited on conductive substrates. The rigorous synthesis conditions, such as high temperatures above 1000°C or moderate temperatures with long sulfurization times in the presence of sulfur, have rendered commonly used conductive substrates like molybdenum, TiO_2 and ITO ineffective.

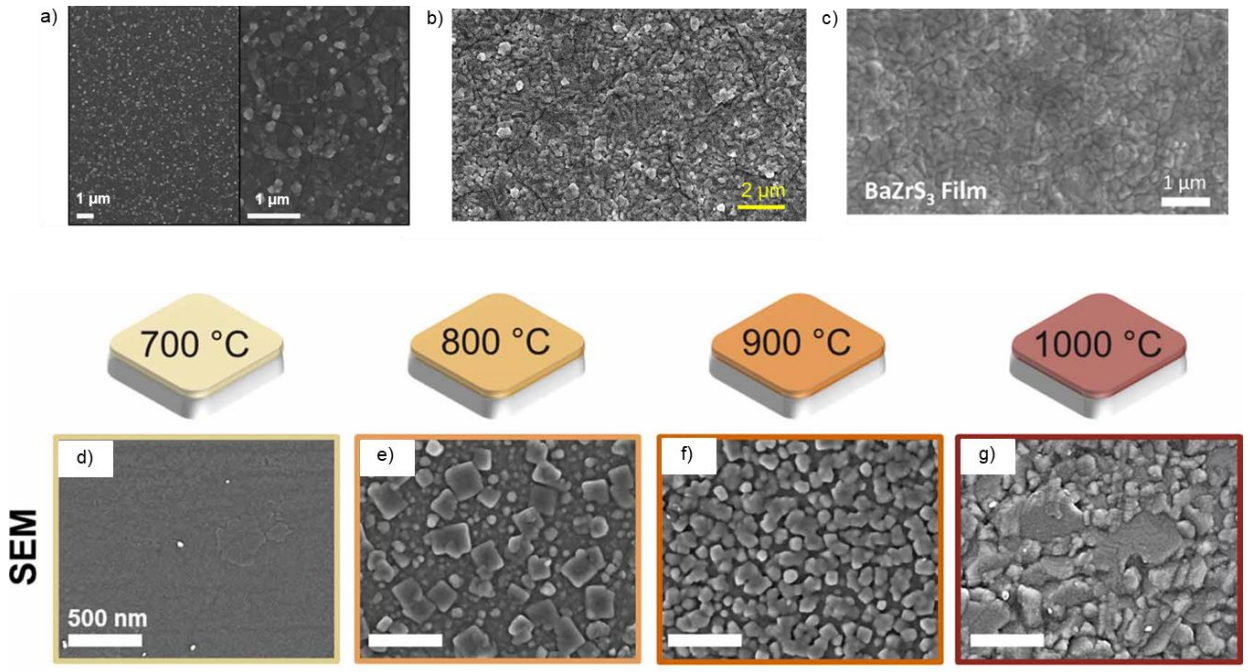

Figure 16. Morphology of $BaZrS_3$ films synthesized using various methods: (a) Gupta et al.[62] via CS_2 sulfurization of an oxide precursor film, (b) Han et al.[48] using magnetron sputtering from a $BaZrS_3$ target followed by annealing, (c) Sharma et al.[92] through CS_2 sulfurization of an oxide precursor film, and (d)-(g) Ramanandan et al.[95] via H_2S sulfurization of an oxide precursor film. a) Reproduced with permission.[62] Copyright 2020, Wiley. b) Reproduced with permission.[48] Copyright 2023, Elsevier. c) Reproduced with permission.[92] Copyright 2023, American Chemical Society. d), e), f) and g) Reproduced with permission.[95] Copyright 2023, IOP Science.

To address this issue, Comparotto et al. co-sputtered Ba-Zr onto a molybdenum deposited silicon substrate and capped the film with a 100 nm thick SnS layer to prevent oxidation before sulfurization in a flow-tube furnace. Surprisingly, they synthesized $BaZrS_3$ film at 590°C with sulfur pressures between 2-4 Pa within 20 minutes, achieving high crystallinity as measured by the FWHM of the 121 XRD peak.[138] This contrasts with Vincent et al., who reported the need for high sulfur pressures (>0.4 bar) for high crystallinity, attributing the success to the presence of BaS_x liquid flux.[101]

Comparotto et al. speculated that they achieved an intermediate flux, such as BaS_3, which reduced diffusion barriers and accelerated kinetics. However, given the low pressures used, it is unlikely they achieved BaS_3.[104] They also suggested that the absence of metal-sulfur bonds in their precursor film provided an alternative nucleation pathway compared to metal-sulfur bonded precursor films.

Interestingly, their synthesis method, possibly due to lower sulfur pressures, allowed the molybdenum back contact to survive, forming only a thin layer of MoS_2, thereby potential opening the door for solar cells and other optoelectronic devices using this approach. Further research into the reaction mechanism of this method is needed to enable its application to other synthesis techniques.

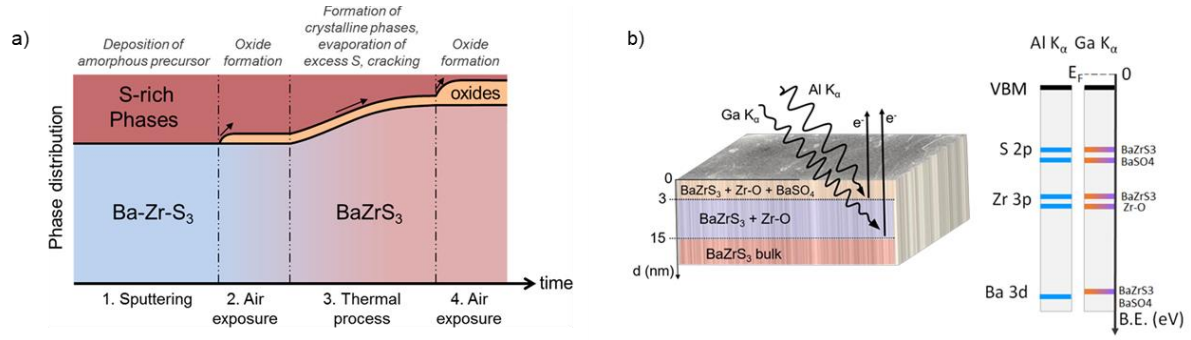

Figure 17. Surface oxide impurities in $BaZrS_3$. a) Schematic representation of phase distribution in the $BaZrS_3$ film over time upon exposure to air. a) Reproduced with permission.[97] Copyright 2020, American Chemical Society. b) Schematic illustrating the different phases present in the near-surface layers, as identified by hard X-ray photoelectron spectroscopy. b) Reproduced with permission.[139] Copyright 2024, American Chemical Society.

2.3. Film Morphology and Composition

Achieving a smooth, well-oriented film with a homogeneous composition and no secondary phases is crucial for synthesizing high-performance devices. Although $BaZrS_3$ films synthesized using CS_2 sulfurization of oxide precursor films have shown reasonable continuity with thicknesses ranging from 200 to 500 nm, they have been deposited on non-conductive substrates, limiting their applicability. Additionally, Gupta et al. observed that their sulfurized films exhibited relatively low crystallinity, with grains embedded in an amorphous matrix.[62] Similarly, Sharma et al., Wei et al., Han et al., and Xu et al., employing similar

sulfurization methods, confirmed the presence of significant oxide impurities on the surface, with species bonded to sulfur and oxygen (S-O) (see **Figures 16.a-c**).[48,57,86,92,140]

Marquez et al. used H_2S to sulfurize oxide precursor films, noting a gradual increase in sulfur incorporation with increasing sulfurization temperature. However, the S/(S+O) ratio plateaued at 0.85 at 1000°C, indicating the presence of substantial oxygen impurities. Despite containing closely packed grains with sizes around 100 nm, the annealed films exhibited cracks, attributed to thermal expansion mismatch between the $BaZrS_3$-$BaZrO_3$ film and the quartz substrate.[68] Ramanandan et al. followed up on Marquez et al.'s film deposition method and found that all sulfurized samples were Zr-rich and Ba-poor, with sulfur content increasing with temperature. They also observed higher sulfur content on the film surface than the bulk due to the diffusion limitation of sulfur-containing species. Unfortunately, the films displayed a Ba-S-O phase in the top layer, a common occurrence in $BaZrS_3$ films derived from oxide precursor sulfurization. Nonetheless, films produced using this method appeared relatively continuous and densely packed (shown in **Figures 16.d-g**).[95]

Comparotto et al. reported around 4% oxygen in the bulk of $BaZrS_3$ film, with a nearly stoichiometric Ba:Zr composition. **Figure 17.a** illustrates their hypothesis regarding the occurrence of oxygen contamination during the synthesis steps. [97] Mukherjee et al. conducted detailed compositional measurements on similarly rapid annealed films, noting compositional fluctuations near the surface, including various sulfur-containing species such as $BaSO_3$ and $BaSO_4$.[141] Riva et al. utilized Al K-α and Ga K-α x-rays to probe different film depths, identifying a $BaSO_4$ and Zr-O-rich layer up to a depth of 3 nm, followed by a Zr-O-rich layer up to a depth of 15 nm (see **Figure 17.b**).[139] Comparotto et al. also observed compositional fluctuations in their Sn-capped $BaZrS_3$ film.[138]

While detailed compositional analysis has not yet been conducted for low-temperature solution-processing methods, these samples indicate compositional fluctuations and non-stoichiometric compositions. Across all $BaZrS_3$ synthesis methods, challenges persist with substantial oxide impurities at the surface, notable oxygen content in the bulk, and significant compositional fluctuations and non-stoichiometries throughout the film. These issues may stem from the high oxophilicity of Zr, Ba's tendency to form stable sulfite and sulfate species, and mass transfer limitations during film growth. Grain size and composition vary depending on the method: solution-processing methods that rely on excess sulfur to access BaS_x flux have produced relatively large cubic grains (>1 μm). At the same time, CS_2 and H_2S sulfurized films exhibit more modest grain sizes. Controlling the composition is essential, as insufficient precision can lead to unwanted defects and impact film properties; addressing these issues is critical. Etching away a few layers from the film may help mitigate surface contaminants, but careful handling is necessary to avoid further contamination from the etchant.

Our group recently demonstrated that $BaZrS_3$ can accommodate barium-poor off-stoichiometric compositions similar to other chalcogenides, such as $Cu(In,Ga)Se_2$. Binary sulfide powders were mixed in various molar ratios with elemental sulfur and heated to a constant temperature of 575°C for 12 hours. No secondary phases were observed up to a Ba:Zr ratio of 0.7. Secondary impurities of ZrS_3 were observed for Ba:Zr ratios lower than 0.7. As expected, the BaS_3 secondary phase was observed for Ba:Zr ratios greater than 1. Since BaS_3 is water-soluble, a gentle water wash dissolved away the secondary phase, resulting in phase-pure $BaZrS_3$. Thus, phase-pure $BaZrS_3$ is attainable for Ba:Zr ratios greater than 0.7. [105] However, the different compositions may have implications on the electronic and optoelectronic properties of $BaZrS_3$, which need further study.

Table 1 summarizes the synthesis conditions for all film deposition methods used to prepare $BaZrS_3$.

Table 1. $BaZrS_3$ thin film deposition methods and synthesis conditions.

Synthesis method	Annealing temp (°C)	Annealing time	Annealing atmosphere	Substrate used	References
Reactive co-sputtering of Ba-Zr-S precursor films at ambient temperature followed by a thermal treatment to induce crystallization	900	1 min	Ar	Si wafer	Comparotto et al.[97]
Polymer-assisted aqueous solution of metal precursors was spincoated followed by sulfurization in a mixed CS_2 and Ar atmosphere	900	3 h	CS_2+Ar	Sapphire	Dhole et al.[94]
CS_2 sulfurization of solution deposited $BaZrO_3$ film	1050	4 h	CS_2+N2	Quartz	Gupta et al.[62]
Magnetron sputtering from the synthesized $BaZrS_3$ target followed by annealing	1000	1-16 h	CS_2	Quartz	Han et al.[48]
PLD deposited Ba-Zr-O films were annealed at temperatures between 700 and 1100 °C under a continuous flow of H_2S gas (5%)	900-1000	30 min	H_2S+Ar	Quartz	Marquez et al.[68]
Doctor blade coating of soluble mixed precursor ink utilizing CS_2 insertion chemistry followed by sulfurization of film in an ampule	575	20 min - 16 h	sulfur+HfH_2	Eagle XG glass	Pradhan et al.[117]
Coating of colloidal $BaZrS_3$ nanocrystals ink in chloroform followed by annealing	150-250	20 min	N_2	Si wafer	Ravi et al.[65]
Drop cast of hybrid precursor ink followed by sulfurization of film in an ampule	575	2 h	sulfur	Al_2O_3 coated Eagle XG glass	Turnley et al.[74]

Epitaxial growth using Pulsed laser Deposition on $LaAlO_3$	700-850		Ar+H_2S	$LaAlO_3$/ $SrLaAlO_4$	Surendran et al.[72]
Sputter Ba-Zr, capped with SnS followed by sulfurized in sulfur environment	600	20 h	sulfur	Mo/Si	Comparotto et al.[138]
Molecular beam epitaxial growth	900		H_2S	$LaAlO_3$	Sadeghi et al.[89]
CS_2 sulfurization of PLD deposited $BaZrO_3$ films	900-1050	4 h	CS_2+H_2/N_2	Sapphire	Wei et al.[86]
CS_2 sulfurization of PLD deposited amorphous Ba-Zr-S films	500-900	2-8 h	CS_2+Ar	Sapphire	Yu et al.[93]
Sputter deposit a stack of BaS/Zr on SiC followed by sulfurization	1000-1050		Sulfur	SiC	Jamshaid et al.[99]
Solution deposit a stack of BaS/ZrS_3 followed by sulfurization	575	2 h	sulfur+HfH_2	Al_2O_3 coated Eagle XG glass	Vincent et al.[105]
Doctor blade coat a mixed precursor ink of BaS and ZrS_3 followed by sulfurization	575	2 h	sulfur+HfH_2	Al_2O_3 coated Eagle XG glass	Vincent et al.[105]

3. Properties of $BaMS_3$ Compounds

3.1. Defect Chemistry

To successfully implement $BaZrS_3$ as a solar absorber in solar cells, it is crucial to understand its defect chemistry. This knowledge can guide the selection of dopants, influencing the conductivity type, carrier concentrations, and identifying deep defects that could hinder the performance of solar cells. Regarding $BaZrS_3$, three studies have reported on its defect chemistry, all using the HSE06 hybrid functional but with different Hubbard U values and supercell sizes.[122,142,143] Despite these variations, all studies agree that sulfur vacancies are the predominant shallow donor defects in $BaZrS_3$, characterized by low formation energies. These low formation energies may result in high electron concentrations under sulfur-poor growth conditions.

The defect calculations included intrinsic point defects such as vacancies (V_{Ba}, V_{Zr}, and V_S), antisites (Ba_{Zr}, Zr_{Ba}, Ba_S, S_{Zr}, S_{Ba}, Zr_S), and interstitials (Ba_i, Zr_i, and S_i). Yuan et al. suggested that, unlike sulfur vacancies, V_{Ba} and Ba_{Zr} also have shallow acceptor defects, albeit with high formation energies. Under sulfur-rich conditions, the defect formation energy of V_S increases while the formation energies of acceptor defects are reduced. Consequently, the Fermi level would be pinned closer to the intersection of V_S and V_{Zr}, which lies approximately 0.5 eV below the conduction band. Therefore, they argued that intrinsic $BaZrS_3$ will always be n-type, while the carrier concentrations can be modified by the growth conditions. The shallow acceptor defects such as V_{Ba}, V_{Zr} and Ba_{Zr} are strongly compensated by the donor defects, and even in the best-case

scenario with p-type doping, under sulfur-rich conditions, the Fermi level will be pinned approximately 0.6 eV above the valence band maximum.[122]

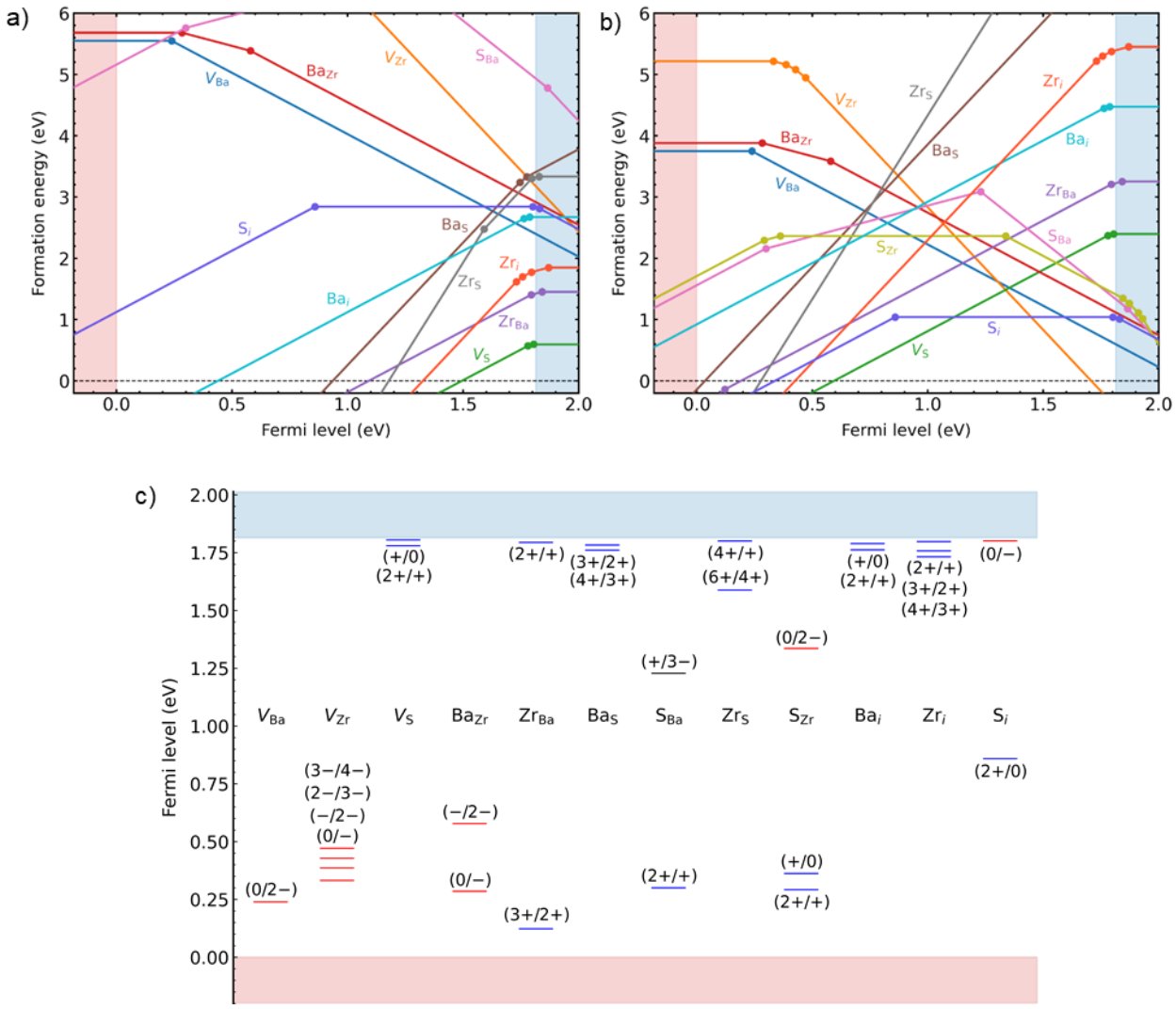

Figure 18. Defect chemistry calculations for $BaZrS_3$. a) Plot showing the formation energy of various defects as a function of the Fermi level under sulfur-poor conditions. b) Plot showing the formation energy of various defects as a function of the Fermi level under sulfur-rich conditions. c) Plot illustrating the charge transition levels of various defects within the forbidden energy region. a), b) and c) Reproduced with permission.[122] Copyright 2024, American Physical Society.

Among the deep defects such as V_{Zr}, Ba_{Zr}, S_{Ba}, S_{Zr}, and S_i, only S_i has a low formation energy, especially in sulfur-rich conditions. Therefore, under sulfur-rich conditions, high concentrations of sulfur interstitials are likely, which could lead to deep recombination centers. **Figure 18** summarizes the defect calculations. Yuan et al. further calculated a capture coefficient of 1.25×10^{-9} cm^3/s, arguing that it is slightly smaller than the dominant recombination centers of iodine interstitials in $CH_3NH_3PbI_3$.[122]

In light of the above discussion, it would be advisable to operate under sulfur-poor conditions to achieve a weak n-type character by optimizing the growth conditions for the films and devising a p-i-n architecture. An external p-type dopant, such as La on the Zr site or alkali metals on the Ba site, could also be explored to keep the electron concentration in check while growing $BaZrS_3$ films under sulfur-poor conditions. Oxygen-related defects could be common in $BaZrS_3$ due to the frequent sulfurization of oxide films to synthesize ternary chalcogenides and the high oxophilicity of early transition elements. Interestingly, Yuan et al.'s calculations showed that both O_i and O_S are electrically inactive and stable in the neutral charge state across almost the entire Fermi level range.[122] Moving forward, it would be valuable to study defect complexes in $BaZrS_3$, as they could have low formation energies and significantly affect the material's intrinsic properties.

3.2. Stability

Chalcogenide perovskites have been proposed as stable alternatives to lead halide perovskites that are known to degrade under heat, air, and moisture. Experimental evidence supports this assertion, with some reports indicating $BaZrS_3$'s superior stability compared to halide perovskites. Gupta et al. highlighted $BaZrS_3$'s improved luminescence stability over methylammonium lead iodide ($MAPbI_3$) perovskite, as the photoluminescence (PL) of $MAPbI_3$ vanished within 2 weeks of exposure to air, whereas $BaZrS_3$ maintained substantial PL even after 5 weeks, though with some reduction in intensity (see **Figures 19.a and 19.b**). They emphasized $BaZrS_3$'s superior chemical stability by observing that the film's X-ray diffraction (XRD) pattern remained unchanged after 10 weeks in ambient conditions.[62] Similarly, Zilevu et al. found no changes in the powder XRD (pXRD) pattern of their synthesized $BaZrS_3$ nanoparticles after 9 weeks of air exposure, indicating robust atmospheric stability even at the nanoscale (shown in **Figure 19.c**).[136]

In addition to atmospheric stability, $BaZrS_3$ demonstrated greater moisture resistance than $MAPbI_3$, which lost its PL instantly upon exposure to steam, while $BaZrS_3$ maintained its PL for 10 minutes in the presence of steam. Ab initio Molecular Dynamic simulations revealed that $BaZrS_3$ has weak interactions with water, and anion vacancy migration, a significant cause of instability in $MAPbI_3$, is seven orders of magnitude lower in $BaZrS_3$, suggesting photodegradation is not a major concern.[62] Han et al. reported strong water stability for $BaZrS_3$ thin films, observing minimal change in electrical conductivity (remaining within 80% of the original value) after 10 cycles of water rinsing (totaling 100 seconds) (shown in **Figure 19.d**). XRD measurements confirmed the phase stability of $BaZrS_3$.[48]

Yang et al. rinsed $BaZrS_3$ powder synthesized from BaS_3 liquid flux multiple times to remove water-soluble impurities, obtaining a phase-pure XRD pattern for $BaZrS_3$.[100] Ravi et al. tested the photocatalytic activity of $BaZrS_3$ nanocrystals (synthesized using an I_2 flux) by studying methylene blue degradation in water under sunlight. Their results demonstrated $BaZrS_3$'s reasonable photocatalytic activity and water stability. However, they noted that $BaZrS_3$ began to degrade in water after 10-12 hours under light and after a few days in the dark.[65] Zilevu et al. also observed their synthesized nanoparticles starting to degrade in water after 30 minutes.[136] In summary, $BaZrS_3$ exhibits much greater water stability than lead halide perovskites but still needs to meet the standard for water-based applications.

Eya et al. recently demonstrated the superior stability of $BaZrS_3$ surfaces in the presence of oxygen and moisture through density functional theory (DFT) calculations.[144] Their study focused on the three most stable surfaces of $BaZrS_3$: (010), (100), and (111). They found that moisture exhibited only weak interactions with these surfaces, while oxygen, although interacting relatively more strongly, did not significantly alter the electronic properties. Notably, these interactions were predominantly localized at Zr sites, with Ba sites showing no interaction with either moisture or oxygen.

In a solar farm exposed to intense heat, solar panels can reach temperatures of up to 60-80°C. Therefore, understanding the thermal stability of promising photovoltaic materials is crucial. In this context, Niu et al. conducted thermogravimetric analysis (TGA) and differential scanning calorimetry (DSC) studies to evaluate the stability of $BaZrS_3$ across different temperatures. They found that $BaZrS_3$ remains stable in air up to 650°C but degrades at higher temperatures into a mixture of $BaSO_4$ and ZrO_2 (see **Figure 19.e**).[64] Similarly, Han et al. heated $BaZrS_3$ in air at 200°C and observed no signs of degradation (illustrated in **Figure 19.f**).[48] Consistent with these findings, Ravi et al. also heated $BaZrS_3$ nanocrystals in air up to 400°C without detecting any degradation.[65] Recently, Bystricky et al. reported significantly higher thermal stability for chalcogenide perovskites (including $BaZrS_3$ and $BaHfS_3$) compared to their lead halide counterparts ($MAPbI_3$ and $CsPbI_3$). They observed that while $MAPbI_3$ and $CsPbI_3$ start decomposing around 250-290°C in air, $BaZrS_3$ remains stable and does not decompose or change composition in air below ~500°C. It decomposes into oxides and sulfates only slowly at higher temperatures. $BaZrS_3$ also showed no degradation in structural or optical properties in air at 100°C for at least one week. The authors attributed the high stability of $BaZrS_3$ to the absence of any organic components and the higher stability of $BaZrS_3$ compared to its binary constituents. Additionally, the lack of a tendency for binary sulfides to undergo sublimation before oxidation further contributes to its stability. Finally, they noted that the presence of a thin layer of ZrO_2 on the surface of the film could also provide stability against oxidation in air.[63]

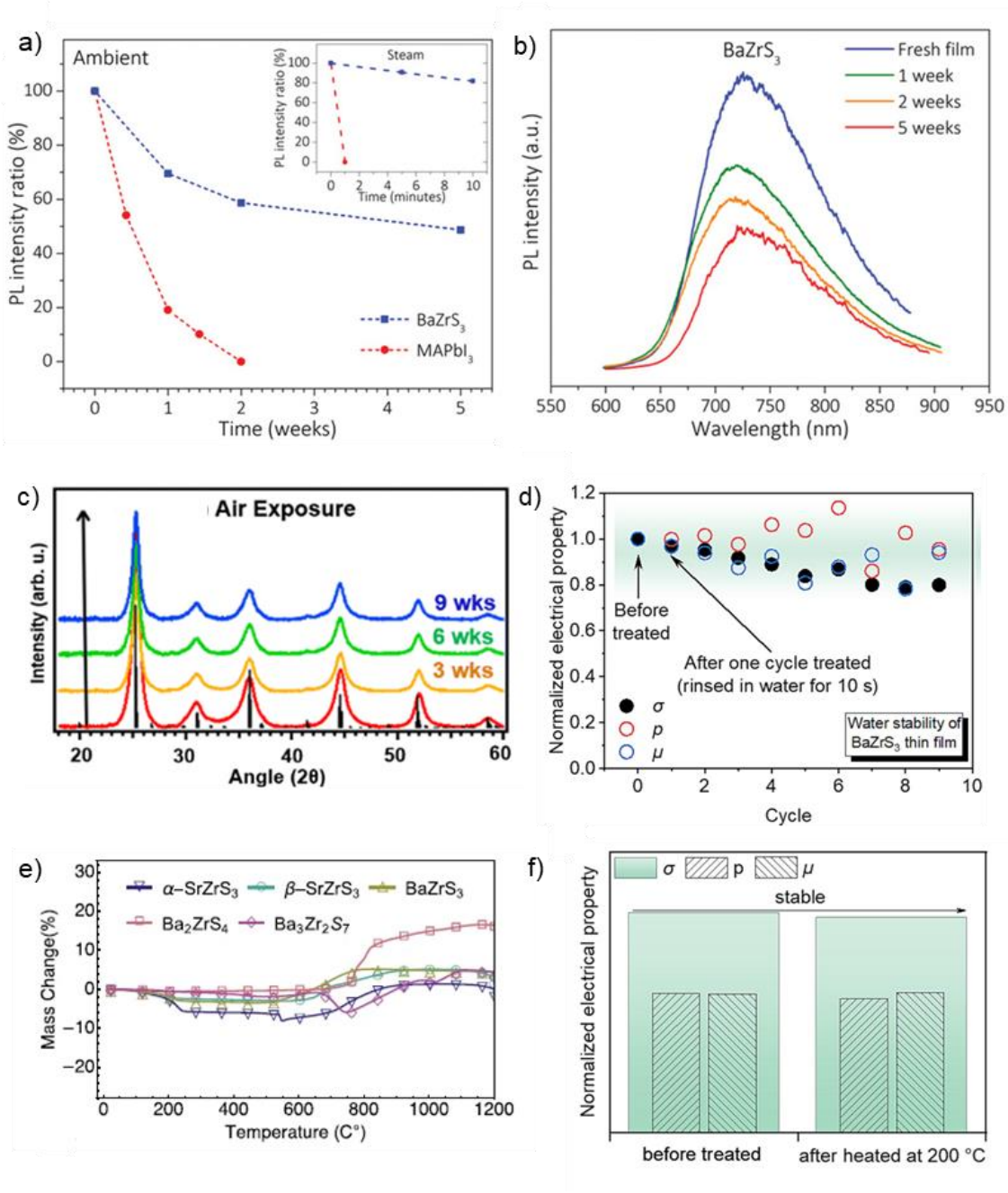

Figure 19. Stability of $BaZrS_3$ against extrinsic factors. a) Plot comparing the PL intensity of $BaZrS_3$ and $MAPbI_3$ films under ambient conditions over time, with an inset showing the variation in PL intensity upon exposure to steam. b) Plot depicting the PL intensity of $BaZrS_3$ over several weeks of exposure to ambient conditions. a) and b) Reproduced with permission.[62] Copyright 2020, Wiley. c) Plot illustrating the structural stability of $BaZrS_3$ nanoparticles over several weeks in air. c) Reproduced with permission.[136] Copyright 2022, Royal Society of Chemistry. d) Plot demonstrating the superior water stability of $BaZrS_3$ film by assessing carrier properties after water rinsing. d) Reproduced with permission.[48] Copyright 2023, Elsevier. e) Plot showing the exceptional thermal stability of $BaZrS_3$ powder up to 500 °C. e) Reproduced with permission.[64] Copyright 2018, Springer Nature. f) Plot indicating minimal changes in the carrier properties of $BaZrS_3$ after heat treatment at 200 °C. f) Reproduced with permission.[48] Copyright 2023, Elsevier.

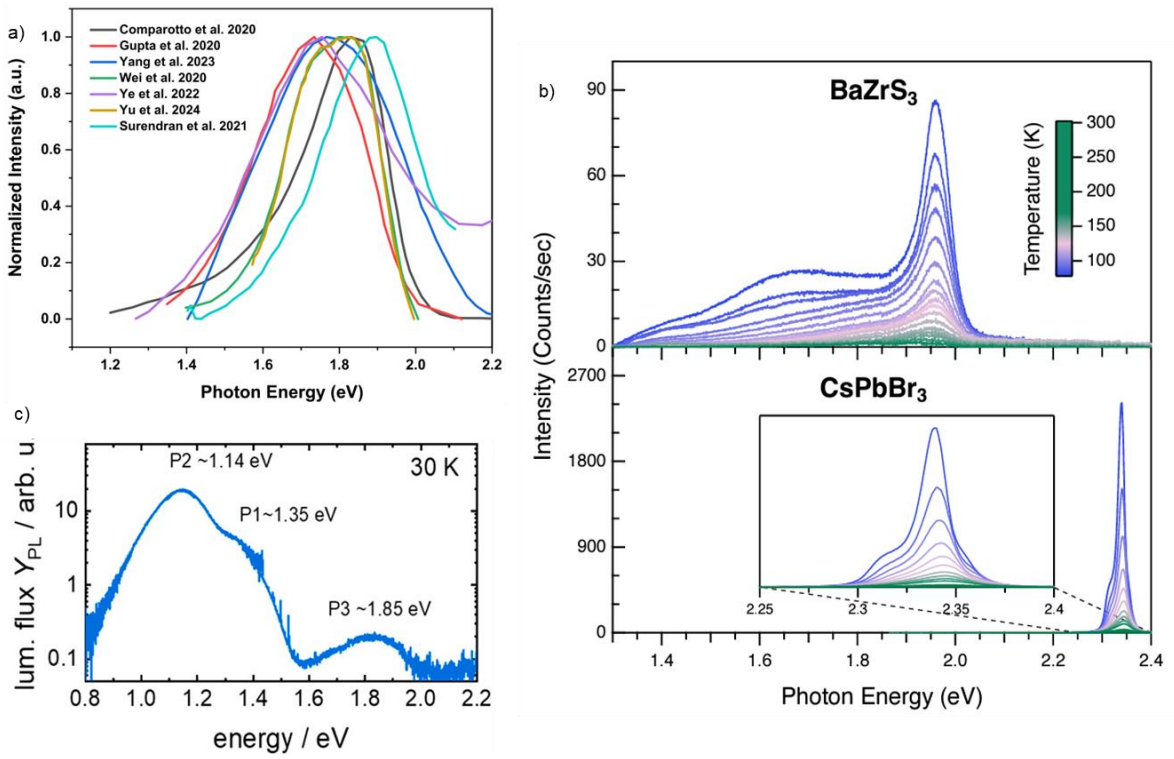

Figure 20. Photoluminescence in $BaZrS_3$. a) Plot comparing the normalized PL spectra of $BaZrS_3$ synthesized using different methods. b) Plot showing the temperature-dependent PL spectra of $BaZrS_3$ and $CsPbBr_3$ single crystals. b) Reproduced with permission.[145] Copyright 2024, American Physical Society. c) Low-temperature PL spectrum of $BaZrS_3$ film grown by H_2S sulfurization of Ba-Zr-O film. c) Reproduced with permission.[68] Copyright 2021, American Chemical Society.

Although macroscopic measurements indicate that $BaZrS_3$ exhibits considerable stability in air, moisture, and heat, further analysis using techniques such as X-ray absorption spectroscopy or X-ray photoelectron spectroscopy could provide more in-depth insights.

3.3. Photoluminescence

Photoluminescence (PL) is a crucial measure of the optical quality of semiconductor materials. Highly luminescent direct bandgap materials, such as halide perovskites, contribute to efficient optoelectronic devices. Quantitatively, photoluminescence is often described as photoluminescence quantum yield (PLQY), which represents the ratio of emitted photons with energy equal to the bandgap to the total number of absorbed photons. PLQY values close to 1 indicate pristine materials with minimal deep defects and limited non-radiative recombination. In addition to PL intensity, the width of the PL peak is significant as it is related to the Urbach energy. A broader PL peak width suggests higher Urbach energy and an increased density of shallow defect states near the band edges. This can have a detrimental effect on the open-circuit voltage of a solar cell.

$BaZrS_3$, which has been indicated as a promising material for optoelectronic applications, has not demonstrated strong photoluminescence, regardless of the synthesis method used. The reported photoluminescence exhibits a broad peak spanning from 1.4 eV to around 2.2–2.3 eV, with peak locations

varying between 1.65–1.95 eV (shown in **Figure 20.a**).[48,51,62,65,68,72,86,92–94,96,97,100,141] The wide range of peak locations suggests that there are variations between samples depending on the synthesis conditions. Additionally, there has been limited characterization of the photoluminescence quantum yield (PLQY) for $BaZrS_3$, but reports suggest that its photoluminescence is significantly weaker than that of strontium-based chalcogenide perovskites.[93] It is worth noting that most samples of $BaZrS_3$ exhibiting reasonable photoluminescence were sulfurized under a CS_2 atmosphere, highlighting the potential role of CS_2 in more effectively removing oxygen impurities. While most PL peaks for $BaZrS_3$ are below 2.0 eV, Yang et al. reported PL around 2.2 eV for the synthesized nanoparticles. They reported the size of $BaZrS_3$ nanoparticles to be between 10-20 nm, which is larger than the exciton Bohr radius calculated by Ravi et al. for $BaZrS_3$. Hence, it is unlikely that the PL peak shift is due to quantum confinement. Since the nanoparticles themselves are not in the true phase and contain unidentified peaks, the actual PL of the synthesized nanoparticles might be blue-shifted. Additionally, any organic residue left from the reaction could also be luminescing and needs to be verified.[65,135]

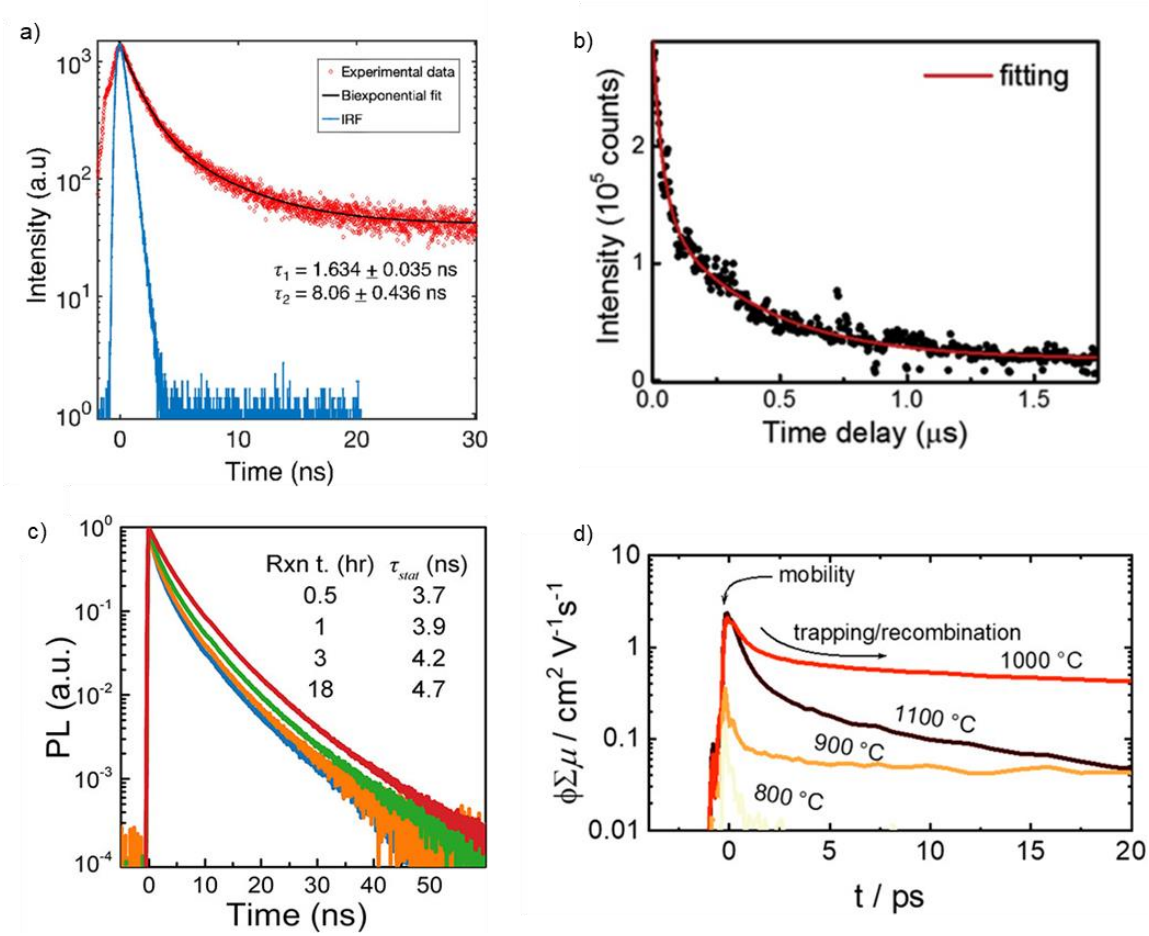

Figure 21. Carrier Lifetime measurements for $BaZrS_3$. a) TRPL measurement on the epitaxial film of $BaZrS_3$ grown by PLD. a) Reproduced with permission.[72] Copyright 2021, American Chemical Society. (b) Time-resolved PL spectrum of the $BaZrS_3$ thin film sulfurized at 1050 °C for 4 hours, showing time constants τ1 and τ2 as 40 ns and 400 ns, respectively, from the bi-exponential fitting. b) Reproduced with permission.[86] Copyright 2020, Elsevier. c) TRPL spectra of $BaZrS_3$ nanoparticles grown by Yang et al.[135] c) Reproduced with permission.[135] Copyright 2022, American

Chemical Society. d) Transient photoconductivity measurements on $BaZrS_3$ films grown by H_2S sulfurization of Ba-Zr-O films. d) Reproduced with permission.[68] Copyright 2021, American Chemical Society.

In a recent study, Ye et al. compared the photoluminescence spectra of $BaZrS_3$ single crystals grown from $BaCl_2$ flux, $BaZrS_3$ films produced via molecular beam epitaxy, and single crystals of lead halide perovskite $CsPbBr_3$. [145] They observed much weaker photoluminescence from $BaZrS_3$ samples than $CsPbBr_3$, with four orders of magnitude higher recombination rate in $BaZrS_3$. This underscores the high concentration of non-radiative recombination centers in the material. Furthermore, the non-radiative recombination in $BaZrS_3$ persisted even at low temperatures, indicating a low thermal activation energy (see **Figure 20.b**). Marquez et al. also reported two mid-gap defect peaks in their $BaZrS_3$ film, one at 1.14 eV and another at 1.35 eV (shown in **Figure 20.c**).[68] The origin of these defect peaks remains to be determined, but they may be present in other $BaZrS_3$ samples that have not been analyzed at such low energy levels. These peaks closely align with the band positions of the Ruddlesden-Popper (RP) phases of Ba-Zr-S, suggesting the potential presence of nano-domains of RP phases within the bulk $BaZrS_3$.

Pradhan et al. measured the photoluminescence of $BaZrS_3$ samples synthesized by the Agrawal group using various solution chemistries and solid-state powders from BaS_x flux, selenium flux, and I_2 vapor transport. They observed weak photoluminescence around 1.05-1.15 eV in all samples.[123] This weak photoluminescence was attributed to deep defects, such as sulfur interstitials, or the presence of undetected secondary phases in small amounts, such as embedded Ruddlesden-Popper phases. In the absence of a clear understanding, further research is needed to identify origins of this peak, as it may be responsible for quenching the photoluminescence in $BaZrS_3$ samples. Additionally, a recent report clarified that the weak photoluminescence observed by Pradhan et al.[117] and Turnley et al.[74] was not due to $BaZrS_3$, but rather caused by calcium impurities. The glass substrate that they used contained calcium, which diffused out during the sulfurization step and likely formed CaS:Zr phosphors. These phosphors were amorphous and, therefore, not detectable by X-ray diffraction. The luminescence of these phosphors is very close to the optical bandgap of $BaZrS_3$. These observations underscore the necessity of carefully selecting substrates. [123] Similarly, Comparotto et al. did not observe significant photoluminescence from films synthesized in a sulfur atmosphere at temperatures below 600°C.[138] Yang et al.[100] and Ravi et al.[65] are the only researchers to report notable photoluminescence for $BaZrS_3$ synthesized at temperatures below 600°C. Notably, Yang et al. found that significant photoluminescence emerged only after water rinsing the synthesized $BaZrS_3$ powder.[100]

Despite the challenges, the reported minority carrier lifetimes in $BaZrS_3$ are comparable to those of other chalcogenides like $Cu(In,Ga)Se_2$, according to studies by Surendran et al., Wei et al., and Ye et al (see **Figures 21.a and 21.b**). Time-resolved photoluminescence (TRPL) data exhibit a biexponential decay, suggesting the coexistence of multiple recombination pathways in the material. This points to the presence of defects, surface recombination, trap states, or different carrier populations. Understanding these processes is crucial for improving the material's optoelectronic properties, especially for applications in photovoltaics and other semiconductor devices. The estimated lifetimes, ranging between 5-50 ns, offer hope, indicating that $BaZrS_3$ may still hold potential.[51,72,86] However, the lifetime values with monoexponential decay reported by Yang et al. need to be revisited, as they appear to be outliers (see **Figure 21.c**).[135] Additionally, the solution-processing method by Apurva et al. achieved only a lifetime of a few hundred picoseconds, highlighting severe recombination centers in those film.[117]

The transient photoconductivity measurements on $BaZrS_3$ film synthesized by Marquez et al. at 1000°C also showed a fast initial decay followed by a longer time constant of around 30 ps, which could possibly be attributed to the trapping of carriers into localized states or the very fast recombination of charge carriers (shown in **Figure 21.d**).[68] Zhao et al. also observed a similar pattern in the transient photocurrent measurement of $BaZrS_3$ single crystal, where the photoexcited carriers showed a fast initial decay followed by a slow decay.[146]

The overall poor photoluminescence in $BaZrS_3$ necessitates a thorough investigation into the presence of deep defects, which may arise from unoptimized synthesis conditions rather than being intrinsic to the material. Improvements in defect control during synthesis and processing are critical for $BaZrS_3$'s potential in optoelectronic applications and represent a significant challenge for its adoption.

3.4. Optical Bandgap

The Tauc plot is a widely used method for estimating the optical bandgap of semiconductors and insulators. It is based on the Tauc equation, which relates the absorption coefficient of a material to photon energy and the type of electronic transition. However, the bandgap determination from the Tauc plot may not be fully accurate due to the simplifications inherent in the approach, which requires an assumption about the type of electronic transition (e.g., direct allowed, direct forbidden, indirect allowed, or indirect forbidden). The estimated bandgap may be imprecise if the assumed transition type is incorrect. On these lines, Nishigaki et al. reported that the lowest transition (V1→C1) is forbidden in $BaZrS_3$ and the next lowest allowed transition (V2→C2) is 0.1 eV higher than the bandgap. This might lead to errors in the bandgap estimation from Tauc plot which has also been reflected in a wide range of bandgap reported for $BaZrS_3$ in the literature 1.7-1.95 eV.[67]

Additionally, the extrapolation of the linear portion of the Tauc plot can be subjective. Determining the exact onset of absorption can also be challenging, particularly in materials with tails in their absorption spectra due to defects, disorder, or other non-idealities. This can lead to an overestimation or underestimation of the bandgap. The assumption of ideal optical absorption processes, such as neglecting excitonic effects, may not always hold and could also lead to errors.

Given these limitations, the Tauc plot is not solely relied upon in the literature and is often complemented with other techniques like photoluminescence, which measures band-to-band emission and is generally considered more reliable. However, as discussed in detail in the previous section, photoluminescence peaks vary significantly across samples and methods in the $BaZrS_3$ literature, leading to a need for a clearer consensus on the actual bandgap. It is believed to be around 1.8 eV, generally within the 1.7–1.9 eV range.[40,48,62,65,86,93,140,147]

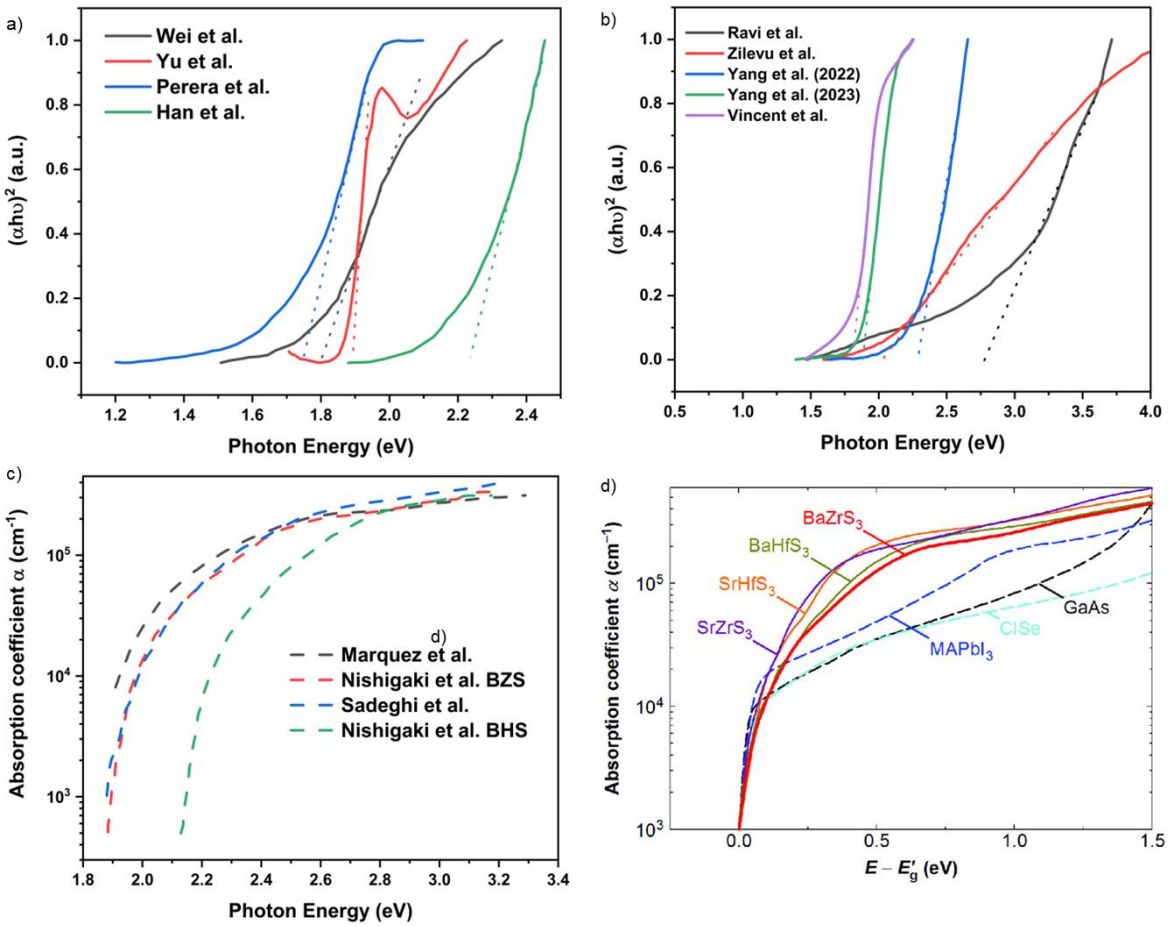

Figure 22. Bandgap and absorption measurements for $BaZrS_3$. a) Tauc plot showing the estimated bandgap for $BaZrS_3$ grown via different methods at temperatures a) exceeding 600°C, b) below 600°C. c) Absorption coefficient measurements of $BaZrS_3$ and $BaHfS_3$ grown via different methods. d) Comparison of the absorption coefficients of chalcogenide perovskites with other notable semiconductors. d) Reproduced with permission.[67] Copyright 2020, Wiley.

Surprisingly, the absorption spectra of $BaZrS_3$ nanoparticles synthesized by Zilevu et al.[135,136] and Yang et al.[135] indicate a bandgap greater than 2 eV. Consequently, these data warrant further investigation. The trends in photoluminescence peaks typically correlate with bandgap estimations from the Tauc plot in the $BaZrS_3$ literature. **Figure 22.a and 22.b** presents the Tauc plot for various synthesis methods and displays a wide range of bandgaps. These variations emphasize the need for streamlined synthesis processes and optimized conditions to achieve consistent results. The bandgap has been estimated to be approximately 2.1 eV for $BaHfS_3$ using Tauc plot analysis.[67,85,105]

3.5. Absorption Coefficient

A high absorption coefficient is desirable for solar cell absorbers as it minimizes the required thickness to absorb nearly all incoming light, thereby reducing material consumption. A thinner film also decreases the series resistance in the solar cell and can accommodate lower carrier lifetimes and mobility. Density Functional Theory (DFT) studies have shown that chalcogenide perovskites, including $BaZrS_3$, possess a high absorption coefficient exceeding 10^5 cm^{-1} within 0.3-0.5 eV above the onset of absorption.[67,143] This

absorption coefficient is significantly higher than that of other commercialized and emerging chalcogenides such as $Cu(In,Ga)Se_2$ and $Cu_2ZnSnSe_4$, and is comparable to or slightly better than lead halide perovskites.[148,149] This high absorption is attributed to the high density of states in the valence and conduction bands of $BaZrS_3$ and other chalcogenide perovskites, where sulfur 3p orbitals constitute the valence band edges and transition metal d orbitals constitute the conduction band edges. This high absorption has also been experimentally verified (see **Figure 22.c**).[67,68,89,140]Furthermore, the light absorption in these materials has been shown to be sharp, resulting in low Urbach energies (22-34 meV), which can help mitigate open-circuit voltage losses in photovoltaic (PV) devices.[67] However, Marquez et al. reported that the absorption coefficient does not conform well to the parabolic band assumption, and the relation $\alpha \propto (E-Eg)^{0.5}$ does not hold.[68] Nishigaki et al. explained this discrepancy based on the forbidden lowest energy transition and the next-lowest energy transition being 0.1 eV above the bandgap.[67] On one hand, this high light absorption coefficient indicates that an absorber film only 100-200 nm thick is required to absorb all incoming light completely. On the other hand, synthesizing such thin films remains challenging for $BaZrS_3$. Nonetheless, Nishigaki et al. compared the absorption spectra of chalcogenide perovskites, including $BaZrS_3$ and $BaHfS_3$, with $MAPbI_3$ and other notable inorganic semiconductors, finding that the former exhibited markedly superior performance (see **Figure 22.d**).[67] The synthesis conditions notably influence the absorption coefficient of $BaZrS_3$, as Marquez et al. observed that it significantly red-shifts and increases in magnitude with enhanced crystallinity and sulfur content. [68] In a different study, Xu et al. sulfurized $BaZrO_3$ powder using CS_2 to synthesize $BaZrS_3$ and observed that the absorbance decreased with an increasing amount of sulfur in the mixture. Conversely, post-annealing of fully converted $BaZrS_3$ in air below 500°C increased the absorbance, suggesting that oxygen impurities in $BaZrS_3$ might actually be beneficial.[140] Therefore, although the material exhibits promising light absorption properties, synthesis-related challenges need to be overcome to fully exploit this potential.

3.6. Carrier Properties

The literature contains numerous examples of solar absorbers that, despite having promising optical bandgaps, lack essential carrier properties such as low effective carrier masses, high carrier mobility, low resistivity, and optimal carrier concentration.[150–152] These properties are crucial for ensuring the unrestricted flow of carriers by minimizing traps throughout the material while maintaining a sufficiently high carrier concentration to form a p-n/p-i-n junction for the effective separation of light-generated charge carriers. Although $BaZrS_3$ is still in its early stages of development, there has been inconsistency in the reported carrier properties. Wei et al. confirmed n-type conductivity in $BaZrS_3$ films synthesized by CS_2 sulfurization of pulsed laser deposition (PLD) deposited $BaZrO_3$ films. They observed n-type conductivity in all samples sulfurized at temperatures between 900-1050°C, attributing this to sulfur vacancies. For sulfur vacancies to contribute electrons to the conduction band and result in n-type conductivity, these vacancies must be shallow defects with low formation energy.[86] Wu et al. and Yuan et al., through computational defect chemistry studies, confirmed that sulfur vacancies act as shallow donor defects in $BaZrS_3$, suggesting that the sulfur vacancies formed at high sulfurization temperatures are likely responsible for the observed n-type conductivity.[122,142] Interestingly, Wei et al. reported high doping density in their $BaZrS_3$ films, with carrier concentrations on the order of 10^{19}-10^{20} cm^{-3}.[86] This implies that approximately one in every 100-1000 sulfur atoms is missing, contributing to the remarkably high doping density. Additionally, finding a compatible p-type layer for n-type $BaZrS_3$ with such high carrier density poses a challenge, limiting its integration into conventional solar cell architectures. Nonetheless, there may be ways to reduce the n-type carrier density, such as external p-type doping to compensate for the high n-type doping. The high carrier

density also results in a moderately high conductivity of 3.52–588 S/cm. Wei et al. also reported a respectable carrier mobility of 13.7 $cm^2/V \cdot s$ for a film synthesized at 1050°C and noted that the carrier mobility increased with sulfurization temperature (see **Figures 23.a-c**). Based on conductivity measurements as a function of temperature, they proposed the Efros-Shklovskii variable range hopping model to describe charge carrier transport in $BaZrS_3$ films and estimated an activation energy of 1.7 meV. This energy was attributed to the ionization energy of sulfur vacancies. Their analysis indicated that sulfur vacancies can be easily ionized at room temperature, leading to a high electron concentration.[86]

Differing from Wei et al., Yu et al. also reported ambipolar conductivity in $BaZrS_3$ films synthesized by CS_2 sulfurization of pulsed laser deposition (PLD)-deposited amorphous films at 500°C. They argued that a lower concentration of sulfur vacancies would result from annealing at a lower temperature. They confirmed n-type conductivity with a significantly lower electron concentration of $4.4x10^{10}$ cm^{-3} when operating the constructed field-effect transistor with positive gate voltage. A similar but lower current magnitude was measured with negative gate voltage, indicating ambipolar characteristics. They further estimated the electron and hole mobilities to be approximately 16.8 and 2.6 $cm^2/V \cdot s$, respectively.[93] The smaller crystallite size resulting from the low-temperature sulfurization step may have increased carrier scattering, reducing carrier mobility. Ravi et al. also reported ambipolar electron-dominated conductivity for the colloidal $BaZrS_3$ nanocrystals.[65]

Recently, Aggarwal et al. demonstrated insulating behavior in $BaZrS_3$ films synthesized by sputtering Ba and Zr onto a substrate, followed by sulfurization in a sulfur atmosphere. [153] However, these films exhibited dominant n-type conductivity when annealed under vacuum at temperatures between 500°C and 600°C. This was attributed to sulfur loss from the film, leading to shallow sulfur vacancy defects. The sulfur vacancies contribute electrons to the conduction band, causing the carrier concentration to increase beyond 10^{20} cm^{-3}, which is sufficiently high for delocalizing shallow defect levels and overlapping with the conduction band edge. While the carrier concentration varied with increasing annealing temperature and time, the carrier mobility remained stagnant around 1 $cm^2/V \cdot s$. The authors attributed this to grain boundary scattering or phonon scattering, possibly unrelated to ionized impurity scattering. However, the carrier concentration saturated after reaching 10^{22} cm^{-3}. Temperature-dependent Hall effect measurements revealed a low activation energy of 8 meV, indicating a shallow donor defect. Similarly, Mukherjee et al. reported n-type conductivity for $BaZrS_3$ films achieved by co-sputtering Ba-Zr-S and annealing the film at 950°C, as evidenced through hard X-ray photoelectron spectroscopy.[141] Additionally, Yang et al. reported n-type conductivity for $BaZrS_3$ bulks with a carrier concentration of 1.02×10^{19} cm^{-3} and a high mobility of 354 $cm^2/V \cdot s$.[66]

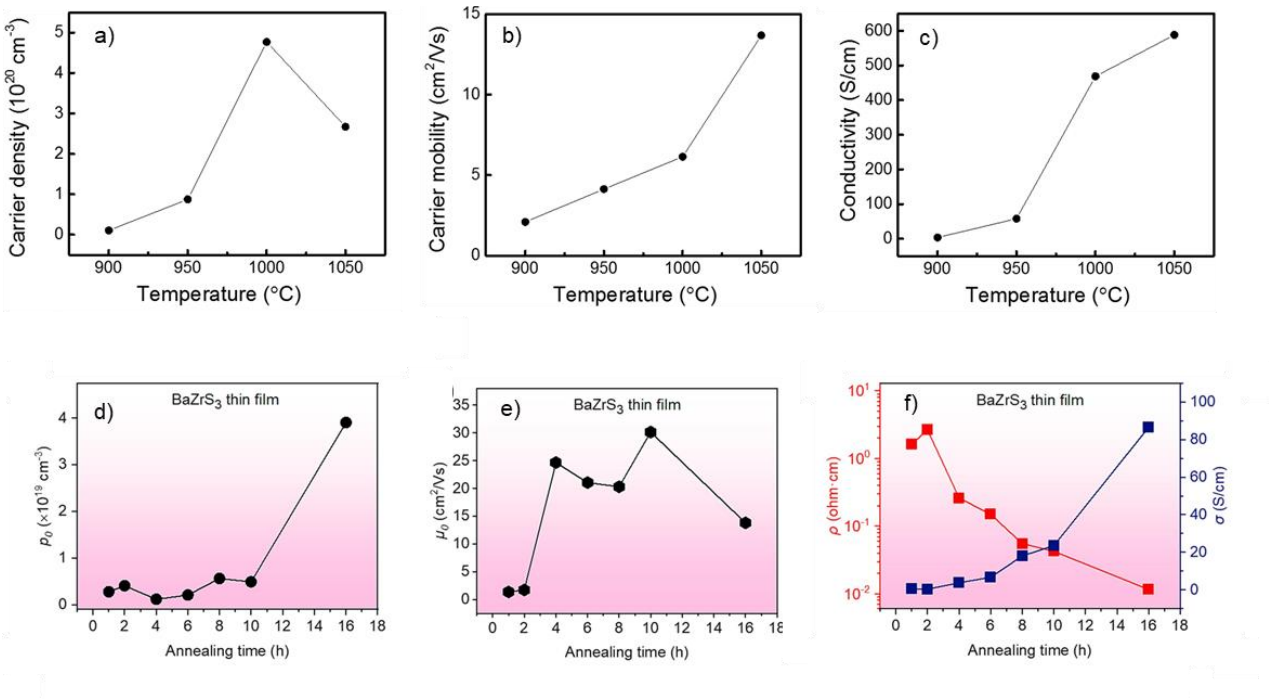

Figure 23. Charge carrier properties of $BaZrS_3$. a)-c) Plots showing the variation in carrier density, carrier mobility, and conductivity with growth temperature for $BaZrS_3$ film synthesized by CS_2 sulfurization of $BaZrO_3$ film. a)-c) Reproduced with permission.[86] Copyright 2020, Elsevier. d)-f) Plots showing the variation in carrier density, mobility, and resistivity/conductivity with annealing temperature for $BaZrS_3$ film grown by magnetron sputtering from a $BaZrS_3$ target. d)-f) Reproduced with permission.[48] Copyright 2023, Elsevier.

Many emerging chalcogenide absorbers exhibit p-type conductivity and have found suitable n-type junction partners. Therefore, a p-type $BaZrS_3$ film might easily find an n-type junction partner. In this context, Han et al. reported $BaZrS_3$ films with p-type conductivity.[48] They synthesized $BaZrS_3$ films at 1000°C via CS_2 sulfurization of amorphous PLD-deposited Ba-Zr-S films and suspected Ba-loss during the growth, resulting in Ba-deficient films. Since barium vacancies are expected to act as shallow acceptor defects, their films demonstrated p-type conductivity, which is rarely reported for $BaZrS_3$. They further noted that the film's conductivity improved with extended annealing time, which was attributed to increased carrier concentration and hole mobility. The mobility enhancement was suggested to result from reduced defect scattering due to the improved quality of the film after prolonged annealing. Additionally, longer annealing times likely led to increased barium loss, thereby increasing the hole concentration after annealing for more than 10 h. While the highest carrier concentration of 10^{19} cm^{-3} was achieved after annealing for 16 h, mobility was compromised. An annealing duration of 4-10 h was found to be optimal, yielding a mobility of 30 cm^2/V.s and a carrier concentration of 10^{18} cm^{-3} (see **Figures 23.f-f**). Temperature-dependent Hall effect measurements indicated an Efros-Shklovskii variable range hopping relationship between conductivity and temperature, from which an activation energy of 26.22 meV was estimated. This activation energy can be roughly interpreted as the ionization energy between the acceptor levels and the valence band edge, suggesting that the acceptor levels in $BaZrS_3$ are shallow.

Instead of performing hall effect measurements, Ravichandran and his collaborators estimated p-type conductivity for the $BaCl_2$ flux-grown $BaZrS_3$ single crystal by measuring the surface photovoltage using the Kelvin probe microscopy.[146] They estimated a positive photovoltage for all the wavelengths tested,

which indicates either a p-type conductivity or hole-transport dominated ambipolar nature of $BaZrS_3$, which could have been induced by the barium or zirconium vacancies during the growth. This is in contrast to the frequently reported n-type conductivity for $BaZrS_3$. Marquez et al. also estimated the combined mobilities of photoexcited electrons and holes from the photoconductivity decay measurements for samples sulfurized under H_2S at 1100°C; a combined mobility of approximately 2 $cm^2/V \cdot s$ was observed.[68]

The literature on the carrier properties of $BaZrS_3$ is limited, with most studies focusing on films synthesized at high annealing temperatures. These films often suffer from barium or sulfur loss, resulting in high concentrations of holes or electrons due to shallow barium and sulfur vacancies. Therefore, a systematic study of the effects of different synthesis conditions, such as annealing temperature, time, and sulfur pressure, on the carrier properties is necessary. Additionally, it would be valuable to investigate the carrier properties of $BaZrS_3$ films produced by recently reported low-temperature solution-processing methods. However, film discontinuity in such methods may limit the measurements. The intrinsic nature of $BaZrS_3$ at low synthesis temperatures might also result in extremely high resistivity in the films, making measurement challenging. Nonetheless, controlling the carrier concentration in $BaZrS_3$ through self-doping or extrinsic doping, along with achieving low effective carrier masses and high mobility, is crucial for the material's utility in electronic devices.

3.7. Polymorphism

Polymorphism refers to the ability of a material to adopt different crystal structures while maintaining the same chemical composition. This phenomenon is often influenced by factors such as pressure, temperature, the type of precursors, and other synthesis conditions. Polymorphism is significant because it can drastically alter a material's optical, electronic, and mechanical properties, enabling its use in diverse applications. For instance, WSe_2 exhibits polymorphism, where the 2H phase is semiconducting while the 1T phase is metallic.[154]

$BaZrS_3$, a chalcogenide perovskite, exhibits an orthorhombic Pnma ground state that has been experimentally verified.[28] However, Kayastha et al. used molecular simulations to demonstrate that, at ambient pressure (0 Pa), $BaZrS_3$ can exist in three distinct polymorphs. [155]They found that the orthorhombic Pnma phase remains stable up to 610 K, beyond which it transitions to a tetragonal I4/mcm phase. At temperatures above 880 K, it converts to a cubic $Pm\bar{3}m$ phase, which is commonly observed in halide and oxide perovskites but had not previously been reported for $BaZrS_3$. Furthermore, Kayastha et al. conducted calculations across varying pressures and temperatures, constructing a comprehensive phase diagram for $BaZrS_3$.

Recently, Jaiswal et al. experimentally validated polymorphism in $BaZrS_3$ by heat-treating $BaZrS_3$ powder in air at various temperatures.[156] Using in situ high-temperature X-ray diffraction, Raman spectroscopy, and bandgap measurements, they characterized the structural phases and optical properties. Their observations diverged slightly from those of Kayastha et al.[155] Jaiswal et al. reported that orthorhombic Pnma $BaZrS_3$ transitions to a Cmcm phase at approximately 400 °C, which subsequently transforms into the tetragonal I4/mcm phase above 500 °C.[156] However, since the heating was done in air, due to oxidation, the $BaZrS_3$ powder began degrading above 500 °C and decomposed completely around 700 °C. No additional phases were observed between 500 °C and 700 °C.

In situ bandgap measurements revealed that within a single phase, the bandgap decreased with increasing temperature. A sharp discontinuity in the bandgap was observed during phase transitions, with the Pnma

phase exhibiting the highest bandgap and the I4/mcm phase the lowest. Notably, upon cooling, the orthorhombic Pnma phase was restored. These findings on $BaZrS_3$ polymorphism are intriguing, as the distinct phases may exhibit other divergent properties. However, isolating these phases at room temperature remains a significant challenge.

3.8. Alloying

3.8.1. Ti alloying

$BaZrS_3$ is attractive for tandem solar cell applications due to its promising properties. However, its bandgap is too high for single-junction applications. One approach to modify the bandgap is through alloying isovalent elements at the A/B/X site, with Ti-alloying in $BaZrS_3$ being particularly promising. Meng et al., through first-principles calculations, demonstrated that 10% Ti alloying in $BaZrS_3$ could reduce the bandgap to 1.47 eV. They predicted, however, that mixtures with more than 25% Ti alloying would decompose into secondary ternary phases. Under pressure, the alloying percentage limit could be higher, indicating that non-thermal equilibrium growth might be necessary for synthesizing $Ba(Zr,Ti)S_3$ films.[143]

Li et al., using first-principles and molecular dynamics simulations, suggested that Ti alloying enhances phonon-electron coupling in $BaZrS_3$, leading to localized polarons that affect carrier mobility. This could potentially result in increased electron-hole recombination and reduced photogenerated carrier lifetime due to alloying with Ti. [157] Nishigaki et al. attempted Ti alloying in $BaZrS_3$ by annealing ground binary sulfide powders. They reported a bandgap reduction for 5% Ti alloying but observed phase segregation at 10% Ti alloying. Additionally, they found that alloying broadened the band-edge absorption, leading to high Urbach energy while maintaining a high absorption coefficient (see **Figure 24.a**). They attributed the tail absorption to atom clustering due to limited Ti-Zr solubility or unoptimized synthesis conditions.[67]

Koratkar group synthesized thin films of $Ba(Zr,Ti)S_3$ and observed a similar monotonic reduction in bandgap with increasing Ti percentage. [96] However, their alloyed films suffered from significant photoluminescence quenching and peak broadening compared to the parent $BaZrS_3$, indicating defect formation from alloying. They also observed phase segregation beyond 6% alloying, with no further bandgap reduction (shown in **Figure 24.b**). Zeng group also attempted the powder synthesis of $Ba(Zr,Ti)S_3$ and reported a monotonic decrease in bandgap with increasing Ti content, reaching 1.51 eV with only 4% Ti alloying. [57] Higher alloying concentrations destabilized the perovskite phase (see **Figures 24.c-d**). Similar to Nishigaki et al., they observed an absorption tail in the 4% alloyed sample, attributing it to secondary phases.

Han et al. deposited thin films of $Ba(Zr,Ti)S_3$ by co-sputtering from $BaZrS_3$ and $BaTiS_3$ targets, observing phase separation beyond 5% Ti alloying. [48] They reported a bandgap reduction to 1.5 eV with 4% Ti alloying. Electrical characterizations of their unoptimized film with pinholes showed high sheet resistance compared to pure $BaZrS_3$ films. Additionally, they reported p-type conductivity for their 4% Ti alloyed film, with a hole concentration of 6×10^{18} cm^{-3} and a carrier mobility of 6 $cm^2/V\cdot s$, which was significantly decreased compared to $BaZrS_3$, likely due to increased scattering effects.

In a recent study, Creutz group explored Ti alloying in $BaZrS_3$ nanoparticles, reporting alloying levels up to 11%. [158] While the behavior of materials at the nanoscale can differ and allow for greater alloying, the synthesized $BaZrS_3$ nanoparticles and their alloys did not posses the correct phase in this study.

Consequently, any higher percentage of Ti alloying in these nanoparticles require further exploration. Nonetheless, this work marks a significant step forward in attempting alloying at the nanoscale.

Similar to Ti alloying in $BaZrS_3$, Ti alloying in $BaHfS_3$ is also a promising approach to reduce its bandgap and enhance its suitability for photovoltaic applications. Kong et al. conducted powder synthesis of Ti alloying in $BaHfS_3$ and observed a reduction in bandgap with no secondary phases up to 5% Ti alloying. UV-Vis measurements revealed that a 5% Ti alloying resulted in a bandgap of 1.4 eV for $Ba(Hf,Ti)S_3$ (see **Figure 24.e**). A similar shift in the photoluminescence peak was also observed for Ti alloying in $BaHfS_3$ (shown in **Figure 24.f**).[85]

3.8.2. Se alloying

In addition to Ti alloying, selenium alloying at the anion site is also an intriguing option to modify the bandgap. Selenium alloying has been observed to reduce the bandgap of chalcogenide semiconductors, making it a potential approach to lower the bandgap of $BaZrS_3$ to within the single-junction photovoltaic limit. However, the bulk $BaZrSe_3$ lacks a distorted perovskite structure, which restricts the amount of selenium that can be alloyed in $BaZrS_3$. Attempts to synthesize bulk $BaZrSe_3$ in a perovskite structure have instead resulted in a $BaNiO_3$-type structure.[159] Ong et al., using ab initio molecular dynamic simulations, predicted $BaZrSe_3$ to be stable with a bandgap of 1.14 eV, but it has not been experimentally observed in thermal equilibrium growth methods.[160] **Figure 25** summarizes the findings from both first-principles calculations and experimental studies, demonstrating the reduction in bandgap with selenium alloying in $BaZrS_3$. Meng et al. conducted first-principles calculations and observed a decrease in bandgap with Se alloying, although they noted a bowing effect at high selenium compositions. They further reported that selenium alloying is less effective than Ti alloying in reducing the bandgap: while 4% Ti alloying reduces the bandgap to 1.47 eV, it takes about 30% Se alloying to achieve the same effect. However, they calculated high absorption coefficients for $BaZr(S,Se)_3$ comparable to $BaZrS_3$.[143] Zitouni et al. corroborated Meng et al.'s findings, showing a reduction in bandgap with Se alloying through first-principles calculations.[161] Li et al. calculated that in $BaZr(S,Se)_3$, the valence band maximum is formed by the orbitals of S and Se atoms, while the conduction band minimum is composed of Zr orbitals. Unlike Ti alloying, they calculated delocalized large polarons with Se alloying, which could benefit charge transport properties. The reduced electron-phonon coupling in $BaZr(S,Se)_3$ would decrease the electron-hole recombination rate and an increase in the carrier lifetime by 60% compared to $BaZrS_3$ was estimated.[157]

However, few experimental reports have attempted selenium alloying in $BaZrS_3$. Nishigaki et al. conducted powder-based synthesis of $BaZr(S,Se)_3$ by mixing BaS, ZrS_2, and $ZrSe_2$ powders and annealing them at temperatures exceeding 1100°C. They observed a monotonic decrease in the bandgap up to 40% Se alloying, beyond which phase segregation occurred. The bandgap decreased by approximately 0.25 eV with 40% Se alloying, with light absorption shifting towards lower energies. Similar to Ti alloying, they noted broadening of the absorption spectrum with Se alloying, resulting in an Urbach energy of 50-70 meV, likely due to increased scattering by atomic clusters or unoptimized synthesis. Additionally, they observed impurities of the Ruddlesden-Popper $Ba_3Zr_2S_7$ phase in their 40% selenium alloyed sample, complicating the accurate estimation of the alloyed content and the observed properties.[67]

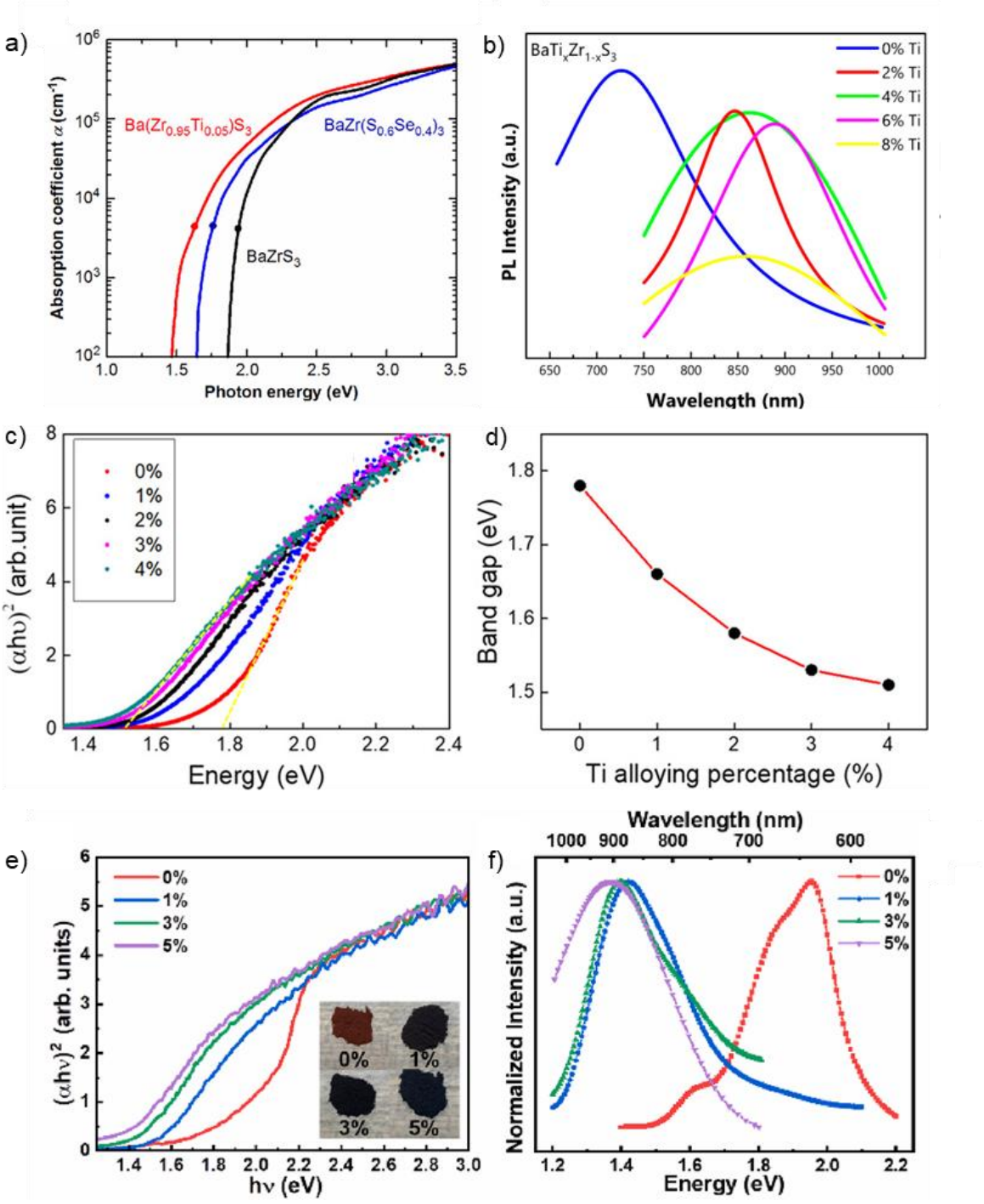

Figure 24. Ti alloying in $BaZrS_3$ and $BaHfS_3$. a) Comparison of the absorption coefficients for $BaZrS_3$ and $Ba(Zr_{0.95}Ti_{0.05})S_3$. a) Reproduced with permission.[67] Copyright 2020, Wiley. b) Comparison of the PL spectra for $BaZrS_3$ and Ti-alloyed $BaZrS_3$. b) Reproduced with permission.[96] Copyright 2021, American Chemical Society. c)-d) Variation in the bandgap with Ti-alloying in $BaZrS_3$. c)-d) Reproduced with permission.[57] Copyright 2020, American Chemical Society. e)-f) Variation in the bandgap and PL spectra with Ti-alloying in $BaHfS_3$. e)-f) Reproduced with permission.[85] Copyright 2024, Elsevier.

While thermal equilibrium growth conditions have resulted in a relatively low alloying limit for selenium in $BaZrS_3$, non-thermal equilibrium growth techniques can potentially overcome this limitation and stabilize higher selenium content in $BaZrS_3$. Jaramillo group demonstrated this by growing Ba-Zr-S-Se films using gas source molecular beam epitaxy with H_2S gas as the sulfur source, stabilizing the full range of compositions $BaZrS_{(3-x)}Se_x$ in the perovskite structure, where $0 < x < 3$. [90] As expected, the bandgap decreased with increasing Se content, with phase-pure $BaZrS_3$ having a bandgap of around 1.9 eV and $BaZrSe_3$ around 1.5 eV. They constructed photodetectors using these films by depositing Ti/Au electrodes on the film's surface and measured the responsivity of the photodetectors. Interestingly, they noted that the responsivity decreased monotonically by several orders of magnitude with increasing selenium content. This significant reduction in responsivity severely limits the utilization of selenium doping in $BaZrS_3$ and could be due to various factors, such as increased bulk or surface defects, which may depend on processing conditions and composition and thus require detailed study.

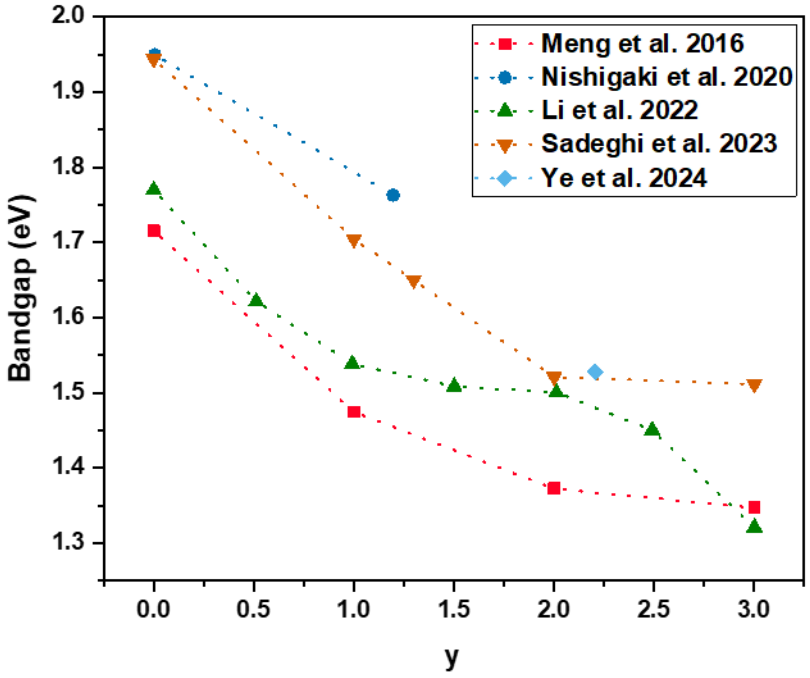

Figure 25. Plot showing the reductions in bandgap for selenium-alloyed $BaZr(S_{3-y},Se_y)_3$.

In other notable work, the Jaramillo group demonstrated the synthesis of $BaZr(S,Se)_3$ films through anion exchange of sulfur with selenium in $BaZrS_3$ films in an H_2Se atmosphere at 800°C without disturbing the microstructure of the original $BaZrS_3$ films. [61] This method does not require the films to be epitaxially grown, and the full range of compositions was achieved for both epitaxial and polycrystalline thin films of $BaZrS_3$. Importantly, they noted that photoresponsivity was orders of magnitude higher for selenium alloyed films grown by the anion exchange method compared to direct growth, possibly due to the reduction of extended defects.

3.8.3. Hf alloying

$BaHfS_3$ and $BaZrS_3$ are expected to be fully miscible across the entire composition range, as both exhibit distorted perovskite structures with similar space groups. The bandgap of $BaZrS_3$ is approximately 1.8-1.9

eV, while that of $BaHfS_3$ is estimated to be around 2.1 eV. Therefore, without considering the bowing effect, the bandgap of the mixture should vary within this range. This tunability in the bandgap of $BaZrS_3$, spanning from 1.4 to 2.1 eV through alloying with Ti, Se, or Hf, could be beneficial for various optoelectronic applications.

Romagnoli et al. synthesized powders of $BaZrS_3$, $BaHfS_3$, and their mixtures by annealing BaS, Zr, Hf, and sulfur powders in an ampule at temperatures below 550°C. [147] As anticipated, they observed homogeneous alloying across the entire composition range. The researchers noted a gradual decrease in lattice parameters and an increase in the bandgap as the Hf content in the mixture increased.

3.8.4. Sn alloying

Tin (Sn) is significantly more stable in the +4 oxidation state than in the +2 state and has an ionic radius very similar to that of Zr^{+4}. Consequently, it presents a viable option for alloying in $BaZrS_3$ to tune the bandgap. However, $BaSnS_3$ is known to crystallize in a hexagonal structure and has only been synthesized under high pressures, making the realization of a high percentage of Sn alloying in $BaZrS_3$ challenging.

Chami et al., through first-principle calculations, demonstrated that substituting Zr with Sn is feasible up to 25%, resulting in a monotonic decrease in the bandgap with increasing Sn content. [60] They predicted a reduction in the bandgap to below 1 eV with 25% Sn alloying and noted a high absorption coefficient for the alloyed sample, accompanied by a red shift in the absorption onset. While these calculations indicate a promising reduction in the bandgap and enhanced optoelectronic properties, achieving 25% Sn alloying in polycrystalline samples might be difficult due to the different structures of the terminal ternaries.

3.8.5. Ca alloying

In a recent study aimed at identifying high-performance elements for alloying in $BaZrS_3$, Sharma et al. utilized first-principle calculations and machine learning models to generate data and train a predictive model for the defect formation energy and bandgap as a function of the alloying percentage of an element in $BaZrS_3$. Their calculations identified Ti and Ca as promising elements with low formation energies that could significantly reduce the bandgap. Interestingly, they suggested that 2-4% Ca alloying in $BaZrS_3$ could reduce the bandgap below 1.3 eV, even though the bandgap of the parent compound $CaZrS_3$ is estimated to be around 1.9 eV, slightly higher than that of phase-pure $BaZrS_3$. Even considering a possible bowing effect in the bandgap, the observed reduction seems somewhat large.[92]

Nonetheless, Sharma et al. conducted experimental synthesis to verify their findings and observed a significant red shift in the photoluminescence peak with Ca alloying, with the bandgap reduction stabilizing after 2% alloying. While there exists a photoluminescence peak at 985 nm, a broad tailing towards lower wavelengths was also observed, indicating the potential presence of secondary phases. Compared to Ti alloying, they suggested that Ca alloying resulted in less quenching of photoluminescence, possibly due to fewer defects.

While Ca alloying appears to be a promising method to reduce the bandgap of $BaZrS_3$, a more comprehensive study is needed to investigate the solubility limit of Ca in $BaZrS_3$, the defects formed, the band tailing towards higher energies, and the impact on carrier transport. This would be necessary to confirm its reliability as a method for bandgap reduction compared to Ti or Se alloying.

3.9. Effect of Pressure

High pressure can significantly influence the electronic and mechanical properties of a material. It can lead to modifications in the band structure as the atomic distances change, affecting the bandgap, conductivity, and other electronic properties. Mechanically, high pressure typically increases stiffness and hardness and can induce phase transitions that fundamentally alter the material's structure and properties. Rong et al. conducted ab initio DFT calculations to determine the effect of pressures up to 20 GPa on the structure of $BaZrS_3$. [162] They observed that the ductility of $BaZrS_3$ increased with pressure, as did the dielectric constant. Additionally, all the peaks of the optical constants shifted to lower energies, i.e., they exhibited red shifts. Gross et al. experimentally confirmed a red shift in the absorption edge with increasing pressure, noting a decrease of approximately 0.015 eV/GPa. They also did not observe any structural changes in $BaZrS_3$ up to 8.9 GPa.[83]

3.10. Properties of $BaTiS_3$

Unlike $BaZrS_3$ and $BaHfS_3$, $BaTiS_3$ is important for its quasi-1D structure, which unlocks a range of interesting properties. Notably, it exhibits giant optical anisotropy and electronic phase transitions, which enable functionalities such as polarization detection and resistive switching.[131,132] $BaTiS_3$ demonstrates optical anisotropy at mid-wave and long-wave infrared energies, making it an excellent candidate for polarization-selective infrared optics (shown in **Figure 26.a**).[163]

While reports exist on nanocrystals and quasi-epitaxial thin films of $BaTiS_3$, emerging studies highlight the large single crystals synthesized either through chemical vapor transport (CVT) or metal salt fluxes such as BaI_2, $BaCl_2$, or KI.[91,124,125] Interestingly, single crystals obtained from KI flux have been significantly larger in volume compared to those synthesized from chemical vapor transport or barium salt fluxes.[132]

Chen et al. achieved a high birefringence of 0.8 in the mid-infrared region for wavelengths of 4 μm and above in their KI flux-grown (001) oriented $BaTiS_3$ crystals and discovered a high dichroic window from 1 to 4 μm. [132] Previously, Niu et al. measured a high birefringence of 0.76 in their CVT-grown single crystals and observed two distinct absorption edges at 0.28 eV and 0.78 eV, resulting in a large dichroic window.[164] Yang et al. studied the photoelectric properties of $BaTiS_3$ and fabricated a polarized photodetector using an $Ag/BaTiS_3/Ag$ architecture, which showed a broad wavelength detection range from visible light to 1550 nm and a high responsivity of 1.22 A/W and detectivity of $3.8*10^{10}$ Jones under 780 nm illumination. The photodetector device characteristics are shown in **Figures 26.b-h**. Yang et al. also reported excellent transport properties for CVT-grown and sulfur-treated $BaTiS_3$ crystals with mobility around 300 $cm^2/V{\cdot}s$ along the c-axis and n-type conductivity. These exciting properties suggest that $BaTiS_3$ could have applications in optical communication and integrated polarization sensors, among other fields.[131]

The measured bandgap, band positions and other properties of $BaTiS_3$ are listed in **Table 2** and **Figures 26.i-j**. The low thermal conductivity and structural anisotropy of $BaTiS_3$ could also make it favorable for thermoelectric applications. Sun et al. identified glass-like ultralow thermal conductivity in pristine, high-quality crystals of $BaTiS_3$, attributed to sub-THz frequency atomic tunneling states.[165] Using first-principles calculations, Paudel et al. estimated a maximum power factor of 928 $\mu W/K^2$ and a thermoelectric figure of merit (ZT) of 0.48 for electron-doped $BaTiS_3$, and a power factor of 74 $\mu W/K^2$ and ZT of 0.17 for a hole-doped sample at room temperature. The power factor and ZT increase with temperature, reaching a ZT of 0.77 for electron-doped $BaTiS_3$ at 800K.[30] These impressive values underscore the thermoelectric potential of $BaTiS_3$.

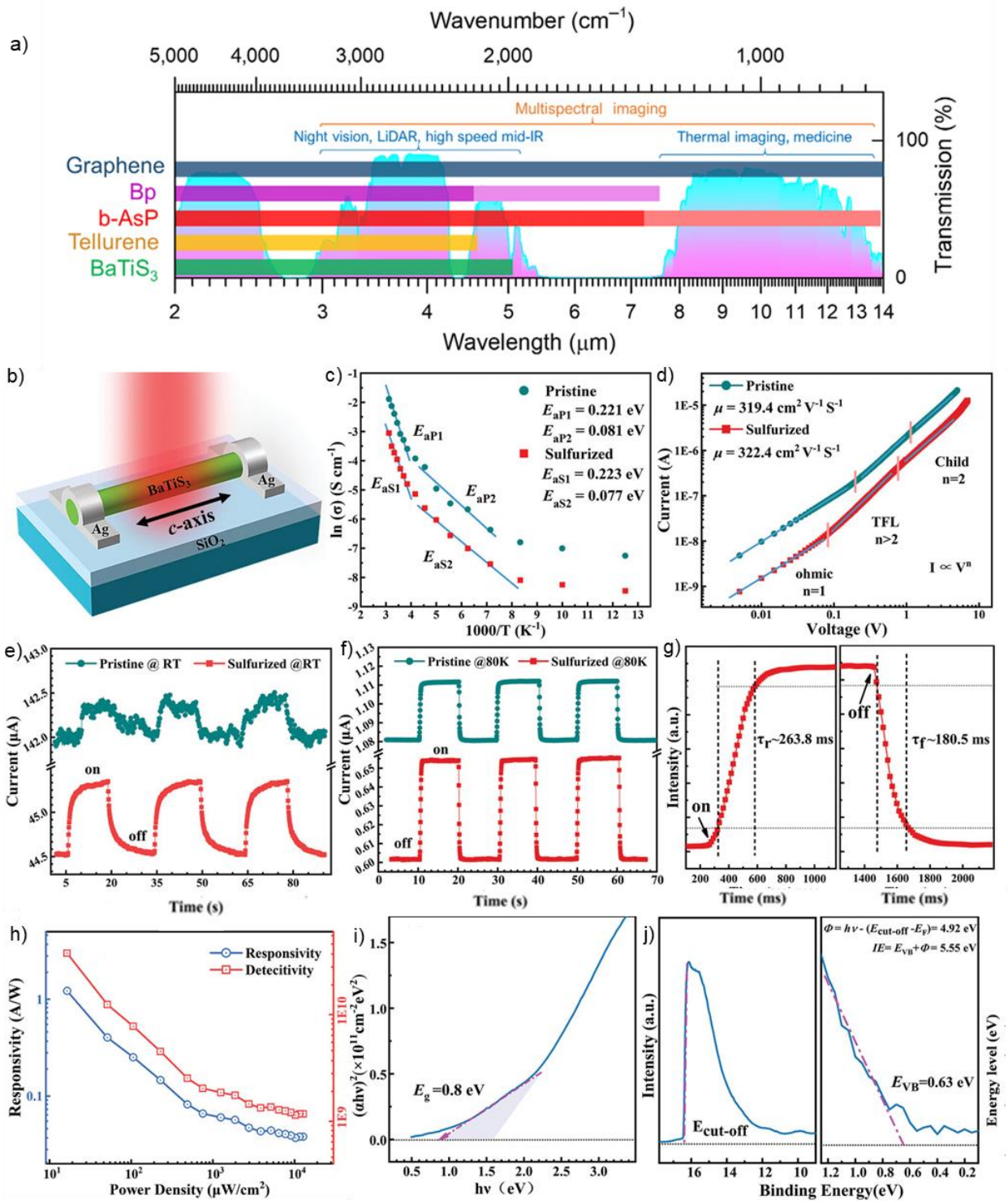

Figure 26. Photoelectric performance of $BaTiS_3$ photodetectors and the electronic configuration. (a) Transmission spectrum of the atmosphere in the mid-IR range, showing the band gaps of various two-dimensional (graphene, BP, b-AsP, and Te) and quasi one-dimensional materials ($BaTiS_3$). a) Reproduced with permission.[163] Copyright 2021, Springer Nature. Defect characterization and photoelectric performance of $BaTiS_3$ single crystal photodetectors. b)

Configuration of the $BaTiS_3$ photoconductive detector under near-infrared light irradiation. c) Temperature-dependent conductivity and corresponding Arrhenius fitting of pristine and sulfurized $BaTiS_3$ single crystals from 80 to 320 K. d) Linear and quadratic fittings according to the SCLC model. e)-f) Comparison of the temporal photocurrent response performance for pristine and sulfurized $BaTiS_3$ photodetectors at room temperature (RT) and 80 K, @1 V, 780 nm illumination with a power density of 12.8 mW cm^{-2}. g) Time-resolved photoresponse speed of the $BaTiS_3$ photodetector under 780 nm illumination, @1 V, 80 K. h) Light intensity-dependent responsivity and detectivity of the $BaTiS_3$ photodetector under 780 nm illumination, @1 V, 80 K. i) Tauc plot from the optical absorption spectrum of $BaTiS_3$ films showing an Eg ≈ 0.8 eV. j) UPS spectrum (left) and the valence band spectrum (right) of $BaTiS_3$ with He 1 excitation. b)-j) Reproduced with permission.[165] Copyright 2020, Springer Nature.

Table 2. Basic properties of $BaTiS_3$.

Property	Value
Thermal conductivity (W m^{-1} K^{-1})	0.39 (ref. [165])
zT	0.48 (e^- doped sample), 0.17 (h^+ doped sample) (ref. [30])
bandgap	0.85 (ref. [131]), 0.5 (ref. [30])
Conductivity	n-type (ref. [131])
Fermi level (eV)	4.92 (ref. [131])
Deep defect activation energy (eV)	~0.44 (ref. [131])
Shallow defect activation energy (eV)	~0.11 (ref. [131])
Dielectric constant	2152 (ref. [131])
Crystal mobility (cm^2 V^{-1} s^{-1})	322 (ref. [131])
Powder carrier concentration (cm^{-3})	3.6×10^{16} (ref. [131])
Responsivity (@780 nm, 1 V, 80 K)	1.22 AW^{-1} (ref. [131])
Absorption edges	(0.35 eV, 0.77 eV) (ref. [132]), (0.28 eV, 0.78 eV) (ref. [164])
Birefringence	0.8 (ref. [132]), 0.76 (ref. [164])
Dichroic window	1 to 4 μm (ref. [132])

4. Working Applications of $BaZrS_3$

4.1. Photo Detectors

A photodetector can be one of the simplest devices to test the functionality of a semiconductor material, and has thus been frequently fabricated in $BaZrS_3$ research. Koratkar group deposited gold contacts on their CS_2-sulfurized $BaZrS_3$ film to create the device and fabricated a similar device with $MAPbI_3$ for comparison (shown in **Figure 27.a**). [62] They observed a high dark current in the $BaZrS_3$ film, which they attributed to a high number of sulfur vacancies formed due to annealing at high temperatures. Consequently, the photocurrent was estimated by subtracting the dark current from the current under illumination. Interestingly, the measured responsivity value of 46.5 mA/W at 5 V for the $BaZrS_3$ photodetector is comparable to the reported values for lead halide perovskites and the $MAPbI_3$ device they fabricated. While the responsivity of $BaZrS_3$ decreased by 40% after 4 weeks in ambient conditions, the responsivity of $MAPbI_3$ reduced by 95% in just 4 days, and the film decomposed into PbI_2 (see **Figure 27.b**

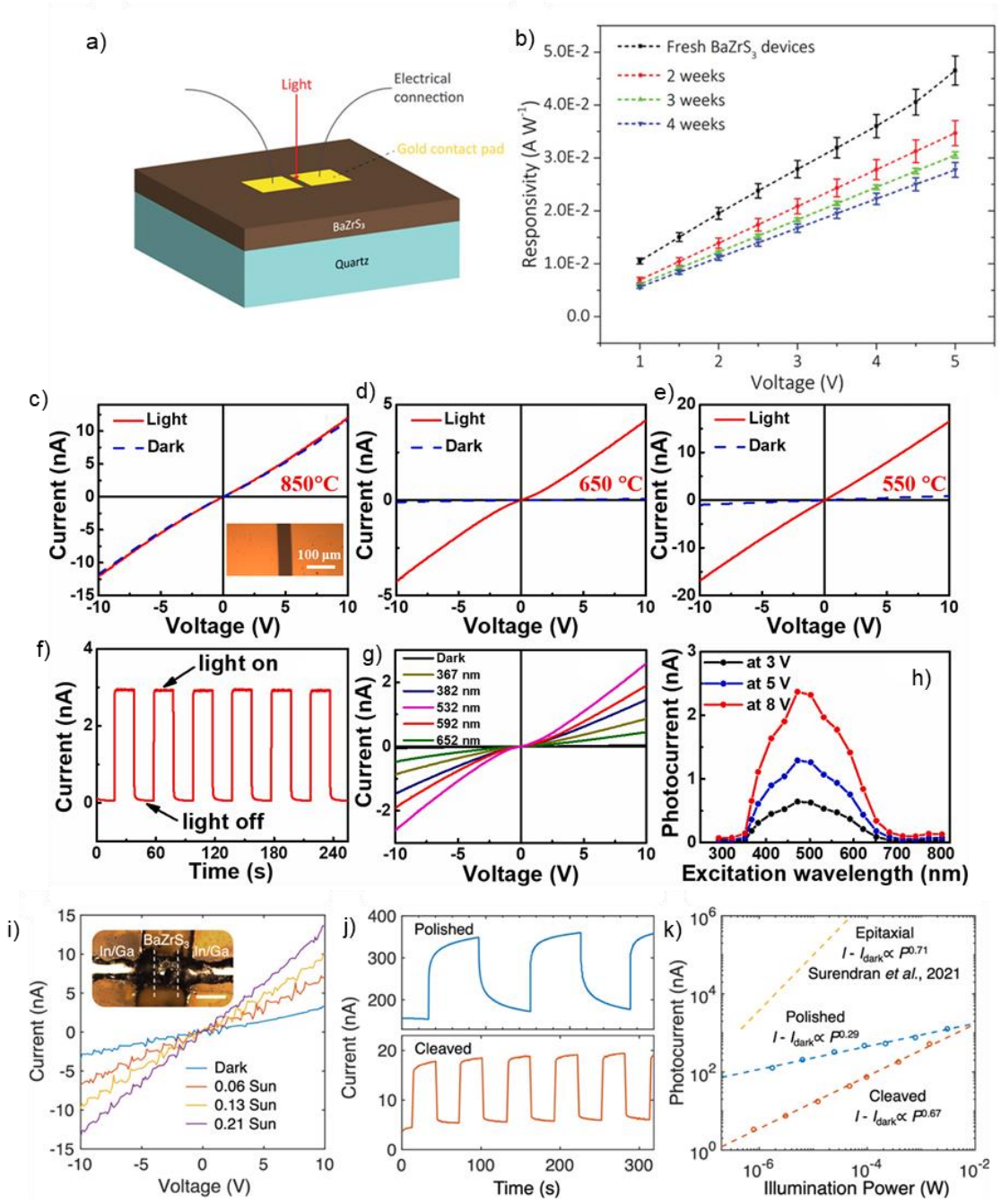

Figure 27. Photoelectric performance of $BaZrS_3$ photodetectors. a)-b) Photodetector design and photoresponsivity measurements as a function of applied voltage for $BaZrS_3$ film grown via CS_2 sulfurization of solution-deposited $BaZrO_3$ film. a)-b) Reproduced with permission.[62] Copyright 2020, Wiley. c)-e) Current-Voltage measurements under dark and illumination conditions for $BaZrS_3$ films annealed at different temperatures during growth. f) Current vs. time for the device using the film annealed at 650 °C, with a periodically switched light source (532 nm) at a fixed bias of 8 V. g) I-V curves measured at different excitation wavelengths for the device using the film synthesized at 650 °C. h) Wavelength-dependent photocurrent at bias voltages of 3, 5, and 8 V extracted from g). c)-h) Reproduced with permission.[93] Copyright 2021, Elsevier. i) Photocurrent vs. voltage for different illuminations. j) Transient photocurrent measurements. k) Photocurrent as a function of illumination power for $BaZrS_3$ single crystal. i)-k) Reproduced with permission.[146] Copyright 2024, American Chemical Society.

Unlike the Koratkar group, Zeng group deposited $BaZrO_3$ films using pulsed laser deposition and sulfurized them in a flowing CS_2 environment at 1050°C. [86] They also observed a high dark current, which was very similar to the current under light, thereby affecting the proper measurement of photoresponse. It was argued that the high annealing time at such temperatures led to a large number of sulfur vacancies, resulting in high carrier concentration and affecting the photoresponse measurements. However, reducing the annealing time significantly increased the sample resistivity and decreased the dark current by three orders of magnitude, further confirming that sulfur vacancies were inflating the carrier concentration. Consequently, a decent photoresponse was obtained.

Table 3. Photoreponsivity and ON/OFF ratios of $BaZrS_3$ photodetector devices.

Responsivity (mA/W) (bias applied)	ON/OFF ratio (bias applied)	Power density (mW/cm2)	Wavelength (nm)	References
0.02 (5 V)	20 (2 V)	58	532	Wei et al. 2020 [86]
46.5 (5 V)	1.5 (5 V)	55	405	Gupta et al. 2020 [62]
0.08 (5 V)	80 (10 V)	140	532	Yu et al. 2021 [93]
6.6 (5 V)	125 (5 V)	60	532	Surendran et al. 2021 [72]
300 (10 V)	3.3 (5 V)	13	532	Zhao et al. 2024 [146]
1 (4 V)			600	Sadeghi et al. 2023 [90]

Zeng group also fabricated photodetectors using $BaZrS_3$ films synthesized by CS_2 sulfurization of PLD-deposited amorphous Ba-Zr-S films. [93] They produced devices for films sulfurized at 550°C, 650°C, and 850°C. Similar to the earlier findings, they reported a high dark current for the film sulfurized at 850°C, likely due to sulfur vacancies that resulted in a high intrinsic carrier concentration, overshadowing any photoresponse. However, much lower dark currents were observed for the films sulfurized at 650°C and 550°C, allowing for the detection of photoresponse with a higher illumination current for the film sulfurized at 550°C (see **Figures 27.c-e**). Despite this, the ON/OFF ratio was only 20, marked by a relatively high dark current, possibly due to poor crystallinity in the film leading to small grains with extended defects that may contribute free carriers. The responsivity of the 550°C film was just 0.08 mA/W at 5 V, significantly lower than the value reported by Gupta et al.[62] The device demonstrates a rapid response with low rise and fall times, as indicated by the current measurements over time under periodic illumination (shown in **Figure 27.f**) whereas **Figure 27.g** shows the I-V curves measured under different illumination wavelength. Furthermore, the film showed the highest photoresponse at an excitation wavelength of around 550 nm and had a cutoff wavelength around 670 nm (~1.85 eV), matching the reported bandgap of $BaZrS_3$ (shown in **Figure 27.h**).

Given that sulfur vacancies inflate the carrier concentration and affect photoresponse measurements, Surendran et al. synthesized pulsed laser-deposited quasi-epitaxial films at 750°C—lower than typical temperatures used in perovskite literature—at low H_2S concentrations.[72] They completed the photodetector by depositing Ti/Au electrodes. The photodetector exhibited photocurrent orders of magnitude higher than the dark current, with a responsivity of 6.6 mA/W at 5V and a 532 nm excitation wavelength, comparable to the 46.5 mA/W reported by Gupta et al.[62] They fitted their photocurrent values at different incident powers to a power law and, based on the extracted exponent, determined that charge trapping limited the photocurrent. They attributed this to sulfur vacancies and oxygen substitution defects.[72] However, recent

work from Hautier's group suggests that sulfur vacancies are extremely shallow defects and oxygen substitution defects are benign, indicating that these should not significantly contribute to charge trapping.[122] Interestingly, the transient photoresponse for Surendran et al. showed an impressively high ON/OFF ratio of 125—the highest reported for $BaZrS_3$—with a rise time of 0.72 s and a decay time of 5.14 s.[72] In comparison, Gupta et al. reported an ON/OFF ratio of merely 1.5.[62] The slow decay time was attributed to sulfur vacancies trapping the carriers, which requires further assessment. The high crystallinity of the epitaxial films, with lower defect density, likely contributed to the improved photoresponse compared to other $BaZrS_3$ deposition methods. It would be interesting to grow these epitaxial films at different temperatures or post-anneal them in a sulfur environment to verify the role of sulfur vacancies in the high performance of epitaxial films.

The Jaramillo group synthesized $BaZrS_3$ and $BaZrS_{3-y}Se_y$ films using gas source molecular beam epitaxy, which is expected to produce pristine, high-quality films. However, they reported a mere 1 mA/W responsivity for the $BaZrS_3$ photodetector, which increased to 100 mA/W for $BaZrS_2Se$ and then declined sharply with further selenium content, indicating an increasing number of defects trapping carriers.[90] Interestingly, their subsequent report showed that H_2Se treatment of $BaZrS_3$ films to synthesize $BaZrS_{3-y}Se_y$ films resulted in orders of magnitude better photoresponse than directly grown films, highlighting the reduced trap centers with the anion exchange method.[61]

While Dhole et al. observed some photoresponse for their polymer-assisted deposited $BaZrS_3$ film, little analysis was performed, making it difficult to compare this method's effectiveness to others based on photoresponse.[94] Single crystals of $BaZrS_3$ likely represent the intrinsic material best. Zhao et al. fabricated a photodetector from $BaZrS_3$ crystals (polished vs cleaved) synthesized using $BaCl_2$ flux and noted a high photoresponsivity of 300 mA/W at 10V under 532 nm excitation.[146] The measured characteristics of the fabricated photodetector are shown in **Figures 27.i-k**. They observed significant dark current and slow response, particularly in the polished crystals, which were characterized by an increased number of surface defects. This observation was further supported by the fitted power law, which revealed a notably lower exponent for the polished crystals.

Although not discussed in detail herein, during the revision stage of this paper, we successfully fabricated a photodetector based on a solution-processed $BaZrS_3$ thin film derived from metal acetylacetonate precursors.[119] Gold contacts were thermally evaporated onto the film, forming Ohmic contacts. The fabricated photodetector exhibited an exceptionally fast photoresponse, with rise and decay times of less than 40 ms—significantly faster than previously reported values for $BaZrS_3$. This improved response time indicates a reduced trap density in the material.

Table 3 summarizes the photoresponsivity and ON/OFF ratios of $BaZrS_3$ photodetector devices. Based on the literature, sulfur vacancies in $BaZrS_3$ are causing excessively high carrier concentrations and negatively affecting device performance. It is likely that defects arising from composition and processing conditions also play a role, as different methods have produced significantly varying photoresponses.

4.2. Photocatalyst and Electrocatalyst

One area where lead-halide perovskites continue to face challenges is in water-based applications, such as photocatalytic hydrogen evolution. Preliminary studies on $BaZrS_3$, however, indicate that it has better water stability compared to halide perovskites. Ravi et al. tested the photocatalytic activity of $BaZrS_3$ in water by evaluating the degradation of methylene blue dye. In their experiments, the absorbance of the dye decreased

significantly in the presence of $BaZrS_3$ nanocrystals, with a reduction of approximately 98% within 50 minutes of exposure to sunlight. While this demonstrates the water stability and photoactivity of $BaZrS_3$, more extensive research is needed to fully assess its potential.[65] In contrast, a recent publication by Humphrey et al. reported computational and experimental measurements indicating that the overpotential of $BaZrS_3$ is much higher than that of Pt.[84] Consequently, $BaZrS_3$ may not be a suitable candidate for the electrocatalytic hydrogen evolution reaction.

Recently, the Chandiran group from IIT Madras employed $BaZrS_3$ in a FTO/TiO_2/$BaZrS_3$ device architecture as a photoanode, with Ag/AgCl serving as the reference electrode and platinum as the counter electrode, for photocatalytic oxygen evolution reactions.[166] They demonstrated the high stability of $BaZrS_3$ across a wide pH range (3–13) using X-ray diffraction measurements. Under simulated one-sun conditions, the device achieved a maximum photocurrent density of 0.36 mA/cm^2 at 0.323 V vs. Ag/AgCl at pH 12, maintaining stability for at least 30 minutes. The study further confirmed the n-type conductivity of $BaZrS_3$ using Mott-Schottky analysis. Additionally, the films exhibited a modest photovoltage of 0.42 V and a high surface charge separation efficiency of 79% at pH 12. Prior to device fabrication, the band alignment was verified by determining the band positions of $BaZrS_3$ relative to the reference electrode using Mott-Schottky plots and absorbance spectra. These findings present promising prospects for the application of $BaZrS_3$ in solar-to-fuel conversion technologies.

4.3. Field effect transistor

Apart from photodetectors, field-effect transistors (FETs) could also be useful devices to test the quality of $BaZrS_3$ films. Ravi et al. utilized nanoparticle ink developed from capping ligands on solid-state synthesized $BaZrS_3$ nanoparticles suspended in chloroform. The film from this colloidal ink was coated, and films annealed at different temperatures were tested for FETs. They argued that the annealing temperature affected the continuity and roughness of the film, possibly due to the decomposition of oleylamine and other molecular residues. They used Si as the substrate and the gate electrode and deposited a thin dielectric layer of ZnO_x on top of the Si substrate via the sol-gel method. A ~50 nm thin layer of $BaZrS_3$ from the colloidal ink was then spin-coated on top of the ZnO_x layer. Finally, Au contacts were deposited, representing the source and drain electrodes. The FETs exhibited ambipolar behavior, conducting both holes and electrons, and showed a high on/off current modulation, indicating their potential as electronic switches. However, the estimated mobilities for holes and electrons were extremely low (below 0.1 cm^2/V·s), which further decreased for films annealed at high temperatures.[65] These results are promising but highlight the need for further optimization of the film synthesis. Otherwise, it is challenging to determine if the film characteristics or the intrinsic properties of $BaZrS_3$ are the limiting factors.

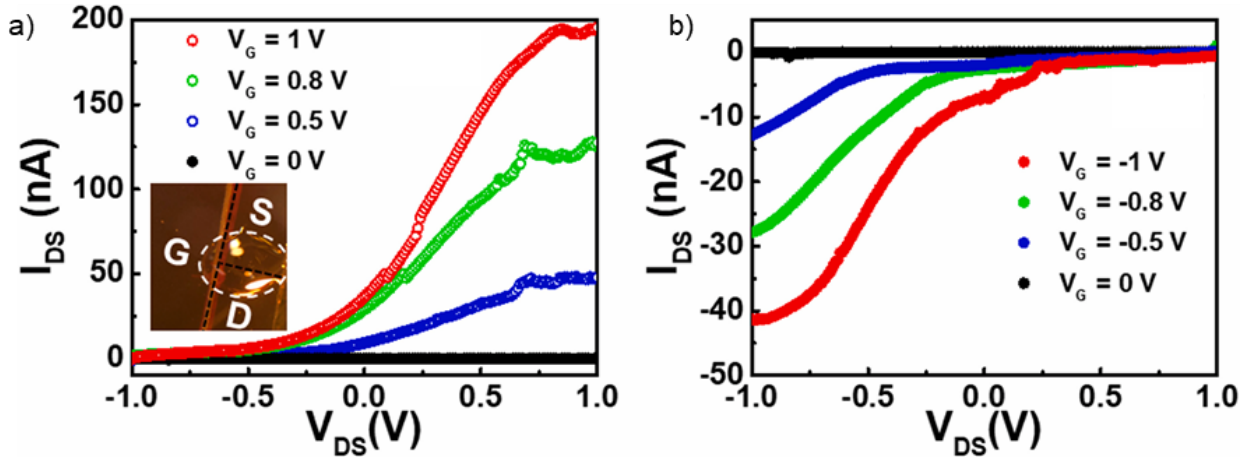

Figure 28. The drain-source current (I_{DS}) versus drain-source voltage (V_{DS}) for the FET fabricated using the film annealed at 650 °C under (a) positive and (b) negative gate voltages (V_G). a)-b) Reproduced with permission.[93] Copyright 2021, American Chemical Society.

Yu et al. also synthesized FETs from $BaZrS_3$ films annealed at 650°C, utilizing the ionic liquid Diethylmethyl(2-methoxyethyl)ammonium bis(trifluoromethylsulfonyl)imide (DEME-TFSI) as the gate and gold (Au) for the source and drain electrodes.[93] Their analysis indicated a low intrinsic density with n-type conductivity. The low-temperature synthesis may have minimized the formation of sulfur vacancies, resulting in a low carrier density of approximately 10^{10} cm^{-3}, which is lower than what is typically reported in the literature. Similar to Ravi et al., a low ON/OFF ratio of around 6.5×10^{-3} was reported. The I-V curves suggested ambipolar behavior in the FETs with decent carrier mobilities, with electron and hole mobilities being 16.8 cm^2/Vs and 2.6 cm^2/Vs, respectively (see the I-V curves in **Figure 28.a-b** with positive and negative gate voltages). They proposed that the small grain size affected the carrier mobilities due to increased carrier scattering, but further work is needed to assess this carefully.

4.4. Photovoltaic

Chalcogenide perovskites have primarily garnered attention for light-emitting diode and photovoltaic applications, largely because lead-halide perovskites have dominated these two areas. $BaZrS_3$, in particular, has attracted interest within the photovoltaic community due to its suitable bandgap for tandem solar cell applications and its theoretically estimated exceptional optoelectronic properties. However, challenges related to finding suitable substrates, high-temperature synthesis, poor film morphology, and mediocre optoelectronic properties have hindered researchers from developing solar cells without first optimizing these variables. Nishigaki et al. proposed a hybrid perovskite/c-Si monolithic two-terminal tandem solar cell architecture for $BaZrS_3$, $Ba(Zr,Ti)S_3$, and $BaZr(S,Se)_3$, given the successful demonstration of high efficiencies in halide perovskite/c-Si tandem solar cells (see **Figure 29.a**). They calculated the maximum achievable efficiencies as a function of the perovskite layer thickness using their measured absorption coefficients, blackbody radiation, and the solar AM 1.5 spectrum. Although their estimation of the bandgap for $BaZrS_3$ was slightly higher than typically reported, they found that $BaZrS_3$ could achieve a maximum efficiency of around 35%. For $Ba(Zr_{0.95}Ti_{0.05})S_3$, the maximum efficiency was around 38.7% with an absorber thickness of 550 nm, an estimated Voc of 2.11 V, a Jsc of 20.6 mA/cm^2, and a fill factor of 0.888. Similarly high efficiencies were calculated for Se-alloyed $BaZrS_3$, although with much thicker films (shown in **Figure 29.b**).

Overcoming the challenges with thin-film fabrication, Dallas et al. successfully synthesized the first working solar cell using $BaZrS_3$, employing a dye-sensitized solar cell architecture with an $I^-/I3^-$ redox electrolyte in an organic solvent and a Pt cathode (see **Figure 29.c**). [167] Following Ravi et al.'s approach, they prepared a colloidal suspension of solid-state nanoparticles, capped with oleylamine ligands and dispersed in chloroform. This dispersion was drop-cast onto a layer of mesoporous TiO_2 on an FTO transparent glass substrate and annealed at various temperatures (120°C, 200°C, and 350°C) to remove excess solvent. They also tested a NaS/S redox couple in H_2O but achieved no reasonable current in the completed devices, suggesting that the $BaZrS_3$ particles decomposed or hydrolyzed in water. Nonetheless, their completed devices with the I^-/I^{3-} redox couple demonstrated some charge separation and collection, reporting an average device efficiency of 0.11% with a maximum efficiency of 0.17%. The devices exhibited a short circuit current of 0.71 mA/cm², an open circuit voltage of 0.39 V, and a fill factor of 63% under 1-sun illumination (shown in **Figure 29.d**). While the efficiencies varied slightly with the annealing temperature, they remained within the same range.[167] Furthermore, their device demonstrated significant stability over time, as illustrated in **Figures 29.e-f**. This does not fully demonstrate the potential of chalcogenide perovskites, especially $BaZrS_3$, but it highlights the need for further optimization of the material and device architecture.

To fully unlock the potential of $BaZrS_3$, it is crucial to utilize a thin-film solar cell architecture. However, there has been limited research on the surface and interfacial properties of $BaZrS_3$. Eya et al. studied various surface terminations, identifying the (001), (100), and (111) surfaces with S-S, S-S, and S-Ba terminations, respectively, as the most stable.[168] They further performed ionization energy and electron affinity calculations for these surfaces and found that the (111) surface forms favorable alignments and optimal band offsets with many electron and hole transport materials (ETLs and HTLs) used in perovskite solar cells (depicted in **Figure 29.g**). According to their calculations, TiO_2, ZnSe, and ZnO are promising electron transport layers due to their low conduction band offsets at the $BaZrS_3$(111)/ETL interface. Similarly, NiO and CuI are attractive options for hole transport layers.[168] However, to date, there has been no experimental verification or utilization of these transport layers. Nonetheless, several SCAPS modeling studies have been conducted to simulate solar cell architectures using $BaZrS_3$. Researchers have explored various architectures, but these simulations often rely on several assumptions about the properties of $BaZrS_3$, which are still under investigation in many cases.[169–175] Therefore, while these studies are useful, they still await a definitive assessment of the performance or potential of $BaZrS_3$-based solar cells.

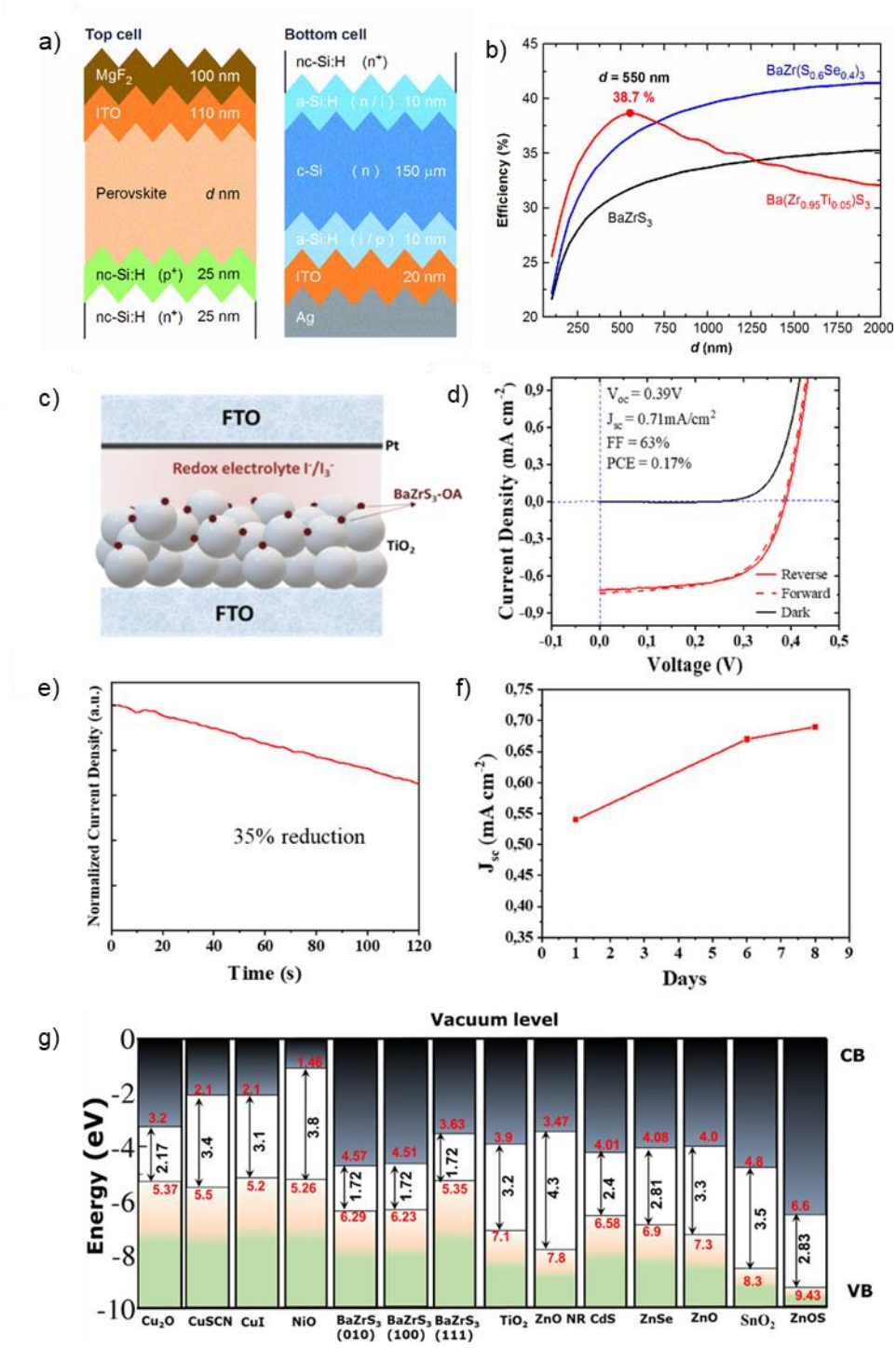

Figure 29. Modeling and experimental performance of $BaZrS_3$ solar cells. a)-b) Proposed configuration of a perovskite-silicon tandem solar cell and the calculated device efficiencies. a)-b) Reproduced with permission.[67] Copyright 2020, Wiley. c) Configuration of a $BaZrS_3$ solar cell in a dye-sensitized architecture. d) J-V characteristics for the synthesized solar cell. e) Maximum power point tracking at V_{MPP}. f) Stability of current density over several days. c)-f) Reproduced with permission.[167] Copyright 2024, Elsevier. g) Estimated band positions of different planes of $BaZrS_3$ along with potential electron transport layers (ETLs) and hole transport layers (HTLs). g) Reproduced with permission.[168] Copyright 2023, American Chemical Society.

4.5. Thermoelectrics

$BaZrS_3$ shows promise for thermoelectric applications due to its high Seebeck coefficient and low thermal conductivity. Through first-principles calculations, Osei-Agyemang et al. determined an effective Seebeck coefficient of 3000 μV K−1 and an ultralow thermal conductivity of 1.16 W/m·K at 300 K, resulting in a thermoelectric figure of merit (zT) around 1 at 300 K, which supports the potential of $BaZrS_3$ as a thermoelectric material. They noted that a high ZT is achieved at carrier concentrations around 10^{15}-10^{18} cm^{-3}, as higher concentrations lead to a decrease in the Seebeck coefficient. As temperature increased, thermal conductivity also increased, causing zT to drop below 1.[176,177] Gupta et al. also reported extremely low conductivity for $BaZrS_3$, with their calculations indicating an enhancement in the Seebeck coefficient and a decrease in thermal conductivity with increasing temperature. Below 500 K, zT decreased with increasing concentration.[62]

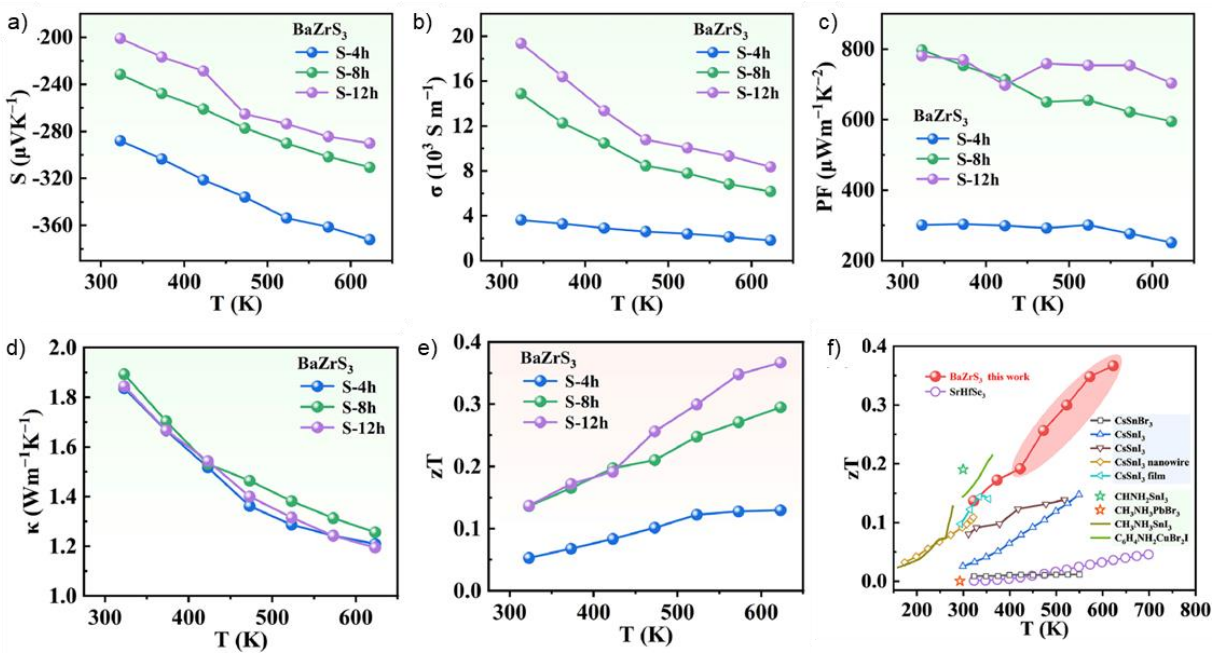

Figure 30. Thermoelectric performance of $BaZrS_3$. a)-f) Seebeck coefficient (S), electrical conductivity (σ), power factor (PF), thermal conductivity (k), and thermoelectric efficiency (zT) as functions of annealing temperature for dense $BaZrS_3$ bulk samples. a)-f) Reproduced with permission.[66] Copyright 2024, Elsevier.

Yang et al. experimentally confirmed the superior thermoelectric performance of $BaZrS_3$. [66] They synthesized $BaZrS_3$ powders and converted them into dense bulks through spark plasma sintering, measuring the electronic and thermoelectric properties (see **Figure 30.a-f**). They found that the samples were electrically insulating at low sintering temperatures, preventing measurement of the Seebeck coefficient, but showed high n-type conductivity at high sintering temperatures (about 1600°C) due to sulfur vacancies. The conductivity increased sharply by 5 orders of magnitude as the sintering temperature rose from 1000°C to 1600°C. For the optimized sintering temperature of 1600°C, the Seebeck coefficient decreased while electrical conductivity increased as the sulfurization time of $BaZrS_3$ powder increased from 4 to 12 hours. This increase in conductivity was likely due to increased carrier concentration from higher sulfur deficiency. The negative Seebeck coefficient indicated n-type conductivity with electrons as the

majority carriers, as expected due to shallow sulfur vacancies. As sulfurization time increased from 4 to 12 hours, carrier concentration rose to 1.02×10^{19} cm^{-3}, while carrier mobility decreased from 385 to 104 $cm^2/V\cdot s$. Nonetheless, these are the highest reported mobility values for $BaZrS_3$, comparable to lead halide perovskites. The authors attributed these high mobility values to improved and optimized synthesis conditions. A low thermal conductivity of 1.74-1.82 W/m·K was achieved at room temperature due to the intrinsic structure of $BaZrS_3$ and high sulfur deficiency, decreasing to 1.11-1.2 W/m·K at 623 K. Consequently, the zT value increased with sulfurization time, reaching a maximum of 0.37 at 623 K for $BaZrS_3$ sulfurized for 12 hours. This experimental zT value for $BaZrS_3$ is among the highest reported for sulfide materials (**Figure 30.f**).

Furthermore, Li et al. investigated the thermoelectric properties of $BaZrS_3$ under pressure and observed a non-linear relationship with pressure due to the irregular variation of the phonon lifetime. They found that the band effective mass and degeneracy decrease, leading to a reduction in the Seebeck coefficient and an increase in electrical conductivity, ultimately reducing the power factor and zT, indicating that the thermoelectric performance of $BaZrS_3$ degrades under pressure. [178] Wu et al. attributed the low thermal conductivity in $BaZrS_3$ to weak bonding and strong anharmonicity, suggesting that the thermoelectric performance of $BaZrS_3$ can be improved by alloying with Se or Ti.[179]

These computational and experimental observations suggest a promising future for $BaZrS_3$ in thermoelectrics. Its thermoelectric performance could also be modified through alloying, doping, nanostructuring, or other strategies.

4.6. Spintronics

Spintronic applications require semiconductor materials with specific properties that enable the manipulation and detection of electron spin states. Semiconductors that exhibit ferromagnetism or can be magnetized are particularly beneficial for spintronic devices, as they combine magnetic and semiconducting properties. To achieve such materials, transition metals are often doped into parent materials to induce magnetism. Yu et al. investigated doping $BaZrS_3$ with up to 5% Mn and Fe, aiming to develop a new magnetic semiconductor. The authors observed that Mn and Fe can be doped at the Zr site up to 5% without forming secondary phases and noted a monotonic decrease in bandgap with increasing doping levels. The level of magnetization also increased with doping. While Mn-doped samples exhibited paramagnetic behavior at room temperature, Fe-doped samples showed ferromagnetism. Nevertheless, further research is required to elucidate the mechanisms by which Mn and Fe doping induces magnetism, to comprehensively characterize the resulting magnetic properties, and to explore the potential of $BaZrS_3$ for applications that leverage these properties.[180]

Recently, Yaghoubi et al. employed density functional theory (DFT) calculations to identify two previously unreported phases of $BaZrS_3$, designated as $Pna2_1$ and $Pmc2_1$, which have not yet been experimentally observed.[181] They noted that these phases exhibit powder X-ray diffraction patterns and Raman spectra that closely resemble those of the widely studied Pnma phase. However, subtle distinctions in Laue diffraction patterns were identified as a potential method for differentiating these phases.

The authors further demonstrated that the non-polar Pnma phase lacks ferroelectric behavior, whereas their calculations suggest that the $Pna2_1$ and $Pmc2_1$ phases exhibit weak ferroelectric properties, with ionic and

electronic polarizations nearly canceling each other. They also proposed that the application of strain could enhance the ferroelectric characteristics of these phases, suggesting that strain engineering may provide a viable experimental approach for observing them.

If validated experimentally, this discovery could hold significant promise for $BaZrS_3$, as ferroelectric behavior in solar cell materials is known to enhance charge separation and potentially improve photovoltaic efficiency. These findings open exciting new avenues for the application of $BaZrS_3$ in advanced optoelectronic and energy-harvesting devices.

4.7. Piezoelectricity

Semiconductor materials are also frequently utilized as piezoelectric materials, where an electric charge is generated in response to applied pressure. This phenomenon arises from the intrinsic crystal structure of these materials, which lack a center of symmetry. When mechanical stress is applied, it causes a displacement of the positive and negative charge centers within the crystal, resulting in an electric dipole moment and the generation of an electric charge on the surface.

While $BaZrS_3$ typically exhibits a centrosymmetric structure (which is generally non-polar and weakly piezoelectric), first-principles calculations by Abir et al. indicate that it has a loosely packed unit cell with significant vacant space. [182] This allows for an extended displacement of ions, resulting in a displacement-mediated dipole moment. Similar piezoelectric behavior is not observed in centrosymmetric $BaZrO_3$ due to its tightly packed unit cell. The significance of the piezoresponse in $BaZrS_3$ lies in the abundance and non-toxicity of its elements, contrasting with other commonly used piezoelectric materials.

Table 4. Basic properties of $BaZrS_3$.

Property of $BaZrS_3$	Reported values
Bandgap (eV)	1.74 (ref. [40]), 1.75 (ref. [62]), 1.82 (ref. [86]), 1.85 (ref. [105]), 1.89 (ref. [93]), 1.9 (ref. [89]), 1.94 (ref. [67]), 2.23 (ref. [48])
Electron Affinity (eV)	(4.57 (010), 4.51 (100), 3.63 (111)) (ref. [168])
Ionization Potential (eV)	(6.29 (010), 6.23 (100), 5.35 (111)) (ref. [168])
Dielectric constant	76.2 (ref. [69]), 46 (ref. [183])
Electron mobility ($cm^2/V.s$)	385 (ref. [66]), 13.7 (ref. [86]), 16.8 (ref. [93]), 1 (ref. [153])
Hole mobility ($cm^2/V.s$)	2.6 (ref. [93]), 30 (ref. [48])
Electron effective mass	0.3 (ref. [184]), 0.43 (ref. [70]), 0.318 (ref. [59]), 0.3 (ref. [122])
Hole effective mass	0.46 (ref. [184]), 0.75 (ref. [70]), 0.459 (ref. [59]), 0.9 (ref. [86,122])
Carrier density (cm^{-3})	(10^{19}-10^{20}) (ref. [86]), 4.4*10^{10} (ref. [93]), > 10^{20} (ref. [153]), 1.102*10^{19} (ref. [66]) ,10^{18} (ref. [48])
Extinction coefficient	1.7 (ref. [168])
Absorption coefficient (cm^{-1})	10^5 (ref. [168]), ~10^5 (ref. [67]), ~10^5 (ref. [68])
Work function	(6.20 (010), 5.624 (100), 5.109 (111)) (ref. [168]), 4.44 (ref. [146])
Reflectivity	22% (ref. [168])
Refractive index	2.75 (ref. [168])
Seebeck coefficient (μV/K)	3000 (ref. [177]), ~280 (ref. [66])

Thermal conductivity (W/mK)	1.16 (ref. [177]), 1.84 (ref. [179]),1.74-1.82 (ref. [66])
zT	0.58 (ref. [179]), ~1 (ref. [177]), (0.37 at 600 K, 0.14 at 300 K) (ref. [66])
Heat capacity (J/g.K)	100 (ref. [177])

For 300 nm $BaZrS_3$ films deposited on quartz, Abir et al. observed a strong piezoelectric response of ~21.38 ± 1.51 pm/V (picometers per volt) through Piezoresponse Force Microscopy (PFM), where the amplitude increased with increasing voltage. This piezoresponse of $BaZrS_3$ is comparable to other piezoelectric materials. This experimental result for $BaZrS_3$ aligns with piezoresponse values calculated through first-principles Density Functional Perturbation Theory (DFPT). Interestingly, the calculated piezoresponse for $BaHfS_3$ is even higher, around 102.58 pm/V (for d21), making it a promising candidate for piezoelectric applications.[182]

Abir et al. also demonstrated practical devices exhibiting piezoelectric behavior by creating a composite matrix of $BaZrS_3$ powder dispersed in polymer (Polycaprolactone: PCL), which provides ductility for energy harvesting materials. They completed the device by attaching Cu electrodes to the top and bottom surfaces of the polymer film. Testing various loadings of $BaZrS_3$ in the polymer, they found that the optimal performance was achieved with 15% loading, as higher percentages led to agglomeration and disconnection from the polymer matrix, reducing response. The device yielded a peak output of ~103.5 μW cm^{-2}, surpassing some of the best-performing piezoelectric materials. Abir et al. successfully demonstrated the charging of capacitors and lighting of LEDs through body movements while wearing their flexible piezoelectric device.[182]

These findings highlight a significant application for $BaZrS_3$. Future research could focus on inducing defects in the material, breaking centrosymmetry, and amplifying the piezoresponse to further enhance its performance.

5. Future challenges and Outlook

$BaZrS_3$ has emerged as an exciting, non-toxic absorber material for photovoltaic applications (**Table 4** summarizes the properties of $BaZrS_3$). Composed of earth-abundant elements, it is expected to benefit from its perovskite crystal structure. Despite advancements in reducing synthesis temperatures, developing various deposition methods, and experimentally verifying its promising absorption coefficient, further work is needed in the following areas to fully demonstrate its potential:

1. $BaZrS_3$ has been synthesized using various methods, including sputtering, pulsed laser deposition, molecular beam epitaxy, and solution processing. However, limited work has been done on optimizing the composition of the final film, leading to inconsistent compositions across the literature. This inconsistency has made it challenging to assess the role of composition accurately. A barium-deficient composition might result in barium-related defects, such as V_{Ba} or Zr_{Ba}, which could impact the optical and electronic properties. In our previous work, we demonstrated that $BaZrS_3$ does not decompose into binaries until the Ba ratio is approximately 0.7. Conversely, barium-rich compositions might lead to undetected amorphous secondary phases in the film, significantly affecting its properties. Therefore, accurate composition determination is crucial for correlating composition with optical and electrical properties. While techniques like energy-dispersive X-ray spectroscopy are frequently used, determining the correct composition without a

$BaZrS_3$ standard is challenging due to overlapping peaks. Thus, exploring other accessible composition analysis techniques is essential. Inductively Coupled Plasma Optical Emission Spectroscopy (ICP-OES) could be one such method, as it can accurately provide the bulk composition, assuming all constituent elements from the film are soluble in a common solvent, typically a dilute acid. However, co-dissolving Ba and S in any dilute acid has been challenging due to the formation of insoluble $BaSO_4$ species.

2. Once a method to accurately measure composition is established, it is essential to study the effect of composition on electrical and optical properties. In sulfur-poor conditions, sulfur vacancies easily form, potentially leading to a very high electron concentration, which is undesirable for a solar absorber. Conversely, sulfur-rich conditions could result in deep sulfur interstitial defects. A barium-poor composition film grown in a sulfur-poor environment might balance out the excess electrons, thereby reducing excess carrier concentrations. Therefore, there is a need to grow films under various sulfur environments with different metal ratios to optimize the properties of $BaZrS_3$ as a solar absorber.

3. It is important to synthesize $BaZrS_3$ at temperatures below 600°C to integrate with other layers of a solar cell, which likely cannot withstand higher temperatures. Although solution-processing methods and sputtering-based techniques have achieved low-to-moderate temperature synthesis of $BaZrS_3$, these methods have shown limited control over material quality. Notably, these methods have reported no photoluminescence in the films, which is concerning. Since most of these methods were conducted in sulfur-rich environments, sulfur interstitials may have formed, quenching the photoluminescence. Additionally, sulfur-poor growth conditions in some methods have resulted in Ruddlesden-Popper impurities, indicating a need for careful optimization of growth conditions at low temperatures. Furthermore, nanoparticles grown by Zilevu et al.[136] did not exhibit photoluminescence, while those by Yang et al.[135] displayed an unnatural blue-shifted photoluminescence peak, potentially arising from secondary phases or organic residues. Importantly, the electrical transport properties of these methods have not been measured and need to be tested and optimized. Overall, low-temperature growth methods are crucial for exploring $BaZrS_3$ in solar cells, but significant work is required to improve and optimize their growth conditions and properties. A low-temperature photoluminescence (PL) study can be performed to investigate the presence of midgap defect transitions. For nanoparticles, conducting a ligand exchange to a more suitable organic or ionic ligand could effectively passivate surface defects, thereby enhancing photoluminescence efficiency.

4. Another significant bottleneck is the overgrowth of grains in methods relying on liquid flux. Solution-processed $BaZrS_3$ films have not been found to nucleate on a hotplate in an inert environment at temperatures below 500°C, unlike other chalcogenides such as $Cu(In,Ga)S_2$ and Cu_2ZnSnS_4. This limitation necessitates an additional sulfurization step, where the amorphous film, consisting of a Ba-Zr-S matrix, is sulfurized in the presence of excess sulfur. This process relies on the formation of BaS_x liquid flux, which apparently does not produce many nucleation sites and causes Ostwald ripening, resulting in large, disconnected grains. Consequently, synthesizing a smooth film with well-connected grains of $BaZrS_3$ through solution-processing methods has been challenging. While methods utilizing sulfurization under CS_2 at high temperatures have achieved reasonable film continuity, they have not attained satisfactory grain growth. Therefore, optimizing growth conditions and creating additional nucleation sites during sulfurization could be crucial for

achieving smooth, contiguous films. This outcome could potentially be achieved through a multi-temperature sulfurization process.

5. To successfully implement $BaZrS_3$ in a thin-film solar cell architecture, the films must be deposited on a conductive substrate. Alternatively, they could be transferred using a conductive epoxy lift-off to a substrate of choice. However, limited work has been done on the former approach, with only one report on $BaZrS_3$ synthesis on a molybdenum substrate, which produced a film with small grain size and significant sulfurization of the Mo contact into a MoS_2 layer, which is not ideal. There does not appear to be a suitable conductive substrate that can withstand corrosive sulfur environments at high temperatures. Similarly, moderate temperatures with long annealing times are also not favorable. While some conductive substrates, such as gold, might be more tolerant to degradation, they would negate the cost and abundance benefits of $BaZrS_3$. A more thoughtful solution is required to address this challenge effectively. Potential approaches may include the development of low-sulfur-pressure-based annealing methods or the transfer of the synthesized film onto a conductive substrate using a lift-off technique.

6. The optical quality of $BaZrS_3$ grown by various methods has consistently fallen short of expectations. While CS_2-based sulfurization methods have yielded films with reasonable photoluminescence, the FWHM of the peaks has been significantly higher compared to lead halide perovskites, indicating substantial defects, disorders, and inhomogeneities within the material. Moreover, there are no reported values of PLQY for $BaZrS_3$. Transient photoluminescence studies on $BaZrS_3$ films and single crystals have shown a fast initial decay followed by a slow decay, further suggesting defect-mediated recombinations. Additionally, other sulfurization methods, including those involving low-temperature synthesis, have produced films with either very broad, low-quality photoluminescence or no photoluminescence at all. This points to a recurring issue of material quality and defect-related problems across all synthesis methods. Yuan et al. described that oxygen-related point defects do not lead to deep states within the bandgap of $BaZrS_3$.[122] Therefore, the argument that CS_2, being more reactive at high temperatures than sulfur or H_2S, would more effectively remove oxygen impurities and thus improve properties may not be valid and requires experimental verification. Even films grown by molecular beam epitaxy have not shown exceptional photoluminescence or photoconductivity, casting doubt on the intrinsic properties of the material. There are also not many reports characterizing the photoluminescence spectra of $BaZrS_3$ across the full wavelength range, as we reported a PL peak at around 1.1 eV in all the solution-deposited films and synthesized solid-state powders irrespective of the flux used.[123] It is difficult to say if it appeared because of some recurring impurity (such as a Ruddlesden Popper phase) or if it is a midgap defect. Hence, a more detailed investigation is needed to improve the bulk material quality and passivate the surfaces.

7. The transport properties of $BaZrS_3$ have not shown significant promise. Most literature reports n-type conductivity for $BaZrS_3$, attributed to shallow sulfur vacancy defects contributing electrons to the conduction band. These shallow defects, which have low formation energy, combined with sulfur-poor growth conditions at high annealing temperatures, have resulted in extremely high carrier concentrations. Such high carrier concentrations are not ideal for a solar absorber in a typical p-n junction architecture and may lead to unwanted Auger recombinations. Therefore, controlling carrier concentrations through engineering growth conditions, adjusting composition, or implementing extrinsic doping is necessary. Extrinsic doping with elements that can introduce

holes to the valence band without creating unwanted mid-gap defects would be ideal, as they can reduce electron concentrations or potentially change the conductivity type with extensive doping. Possible dopants include alkali metals such as Na, K, and La, among others. While the highest carrier mobilities observed for $BaZrS_3$ are comparable to other chalcogenides like $Cu(In,Ga)Se_2$, they are an order of magnitude lower than those for halide perovskites. These mobilities could be limited by unoptimized films with bulk defects, imperfections, small grains with unpassivated grain boundaries, surface states, non-ideal composition, high doping levels, and impurities. Therefore, significant work is needed to address these issues and improve the carrier properties of $BaZrS_3$.

8. Recent studies have successfully alloyed $BaZrS_3$ with Ti, Se, and Hf, exploring a range of bandgaps from 1.3 eV to 2.1 eV. This makes these alloyed absorbers promising candidates for single-junction and tandem solar cell applications. However, most research has focused on synthesizing solid-state powders, with only a few reports on thin films and limited characterizations. Therefore, more comprehensive optical and electronic characterizations are needed to evaluate the absorber quality of these films fully. Other candidates for A-site and B-site alloying, such as Sr, Eu, Mo, Nb, Ta and W, should be explored and studied.

9. The limitations in the material quality of $BaZrS_3$ have hindered the PV community from fabricating solar cells from $BaZrS_3$ and utilizing it for other applications. Dallas et al. made significant progress by employing a dye-sensitized solar cell architecture for $BaZrS_3$.[167] While it is promising to observe some photocurrent and a decent open-circuit voltage, a proper thin-film device architecture is required to unlock the full potential of $BaZrS_3$ for photovoltaic applications. Eya et al. also estimated the band positions of different $BaZrS_3$ crystal planes and suggested various hole and electron transport layers.[168] However, no substantial work has been done to experimentally confirm the band positions of $BaZrS_3$. Therefore, it is crucial to experimentally determine the band positions and identify the junction partners that are compatible with $BaZrS_3$ and other layers to ensure efficient device integration.

10. While the focus is on utilizing $BaZrS_3$ for tandem solar cells, its other exciting properties should also be leveraged for various applications such as thermoelectric, piezoelectric, resistive switching memories, anodes in batteries, gas sensors, X-ray detectors, among others.

$BaZrS_3$ remains an exciting, earth-abundant candidate for photovoltaics and other applications. Over the past 5-6 years, a surge of synthesis methods has significantly reduced the synthesis temperature. There is now an improved understanding of the transport properties, stability, and defect characteristics of the material. However, key challenges persist, including high carrier concentration, inconsistent optoelectronic properties, and the synthesis of a contiguous film with large, connected grains on a conductive substrate. It is expected that the overview of $BaZrS_3$ and the potential strategies for future work presented in this review will aid towards the development and utilization of this class of materials.

Data Availability

No data were used for the research described in the article

Conflicts of Interests

The authors declare that there are no known competing conflicts of interests.

Acknowledgements

This work was supported by the NSF program 10001536 (INFEWS)).

References

(1) Shahbaz, I.; Tahir, M.; Li, L.; Song, Y. Advancements in 2D Transition Metal Dichalcogenides (TMDs) Inks for Printed Optoelectronics: A Comprehensive Review. Materials Today 2024. https://doi.org/10.1016/j.mattod.2024.06.008.

(2) Chaudhary, O. S.; Denaï, M.; Refaat, S. S.; Pissanidis, G. Technology and Applications of Wide Bandgap Semiconductor Materials: Current State and Future Trends. Energies (Basel) 2023, 16 (18), 6689. https://doi.org/10.3390/en16186689.

(3) Dong, H.; Ran, C.; Gao, W.; Li, M.; Xia, Y.; Huang, W. Metal Halide Perovskite for Next-Generation Optoelectronics: Progresses and Prospects. eLight 2023, 3 (1), 3. https://doi.org/10.1186/s43593-022-00033-z.

(4) Guo, Z.; Zhang, J.; Liu, X.; Wang, L.; Xiong, L.; Huang, J. Optoelectronic Synapses and Photodetectors Based on Organic Semiconductor/Halide Perovskite Heterojunctions: Materials, Devices, and Applications. Adv Funct Mater 2023, 33 (46). https://doi.org/10.1002/adfm.202305508.

(5) Song, S.; Rahaman, M.; Jariwala, D. Can 2D Semiconductors Be Game-Changers for Nanoelectronics and Photonics? ACS Nano 2024, 18 (17), 10955–10978. https://doi.org/10.1021/acsnano.3c12938.

(6) Ghosh, B.; Tay, D. J. J.; Roeffaers, M. B. J.; Mathews, N. Lead-Free Metal Halide (Halogenidometallate) Semiconductors for Optoelectronic Applications. Appl Phys Rev 2023, 10 (3). https://doi.org/10.1063/5.0150873.

(7) Li, N.; Zhang, S.; Peng, Y.; Li, X.; Zhang, Y.; He, C.; Zhang, G. 2D Semiconductor-Based Optoelectronics for Artificial Vision. Adv Funct Mater 2023, 33 (52). https://doi.org/10.1002/adfm.202305589.

(8) Verlinden, P.; Young, D. L.; Xiong, G.; Reese, M. O.; Mansfield, L. M.; Powalla, M.; Paetel, S.; France, R. M.; Chiu, P. T.; Haegel, N. M. Photovoltaic Device Innovation for a Solar Future. Device 2023, 1 (1), 100013. https://doi.org/10.1016/j.device.2023.100013.

(9) Rauf, A.; Nureen, N.; Irfan, M.; Ali, M. The Current Developments and Future Prospects of Solar Photovoltaic Industry in an Emerging Economy of India. Environmental Science and Pollution Research 2023, 30 (16), 46270–46281. https://doi.org/10.1007/s11356-023-25471-1.

(10) Urbina, A. Sustainability of Photovoltaic Technologies in Future Net-zero Emissions Scenarios. Progress in Photovoltaics: Research and Applications 2023, 31 (12), 1255–1269. https://doi.org/10.1002/pip.3642.

(11) Liu, J.; De Bastiani, M.; Aydin, E.; Harrison, G. T.; Gao, Y.; Pradhan, R. R.; Eswaran, M. K.; Mandal, M.; Yan, W.; Seitkhan, A.; Babics, M.; Subbiah, A. S.; Ugur, E.; Xu, F.; Xu, L.; Wang, M.; Rehman, A. ur; Razzaq, A.; Kang, J.; Azmi, R.; Said, A. A.; Isikgor, F. H.; Allen, T. G.; Andrienko, D.; Schwingenschlögl, U.; Laquai, F.; De Wolf, S. Efficient and Stable Perovskite-Silicon Tandem Solar Cells through Contact Displacement by MgFx. Science (1979) 2022, 377 (6603), 302–306. https://doi.org/10.1126/science.abn8910.

(12) Li, H.; Zhang, W. Perovskite Tandem Solar Cells: From Fundamentals to Commercial Deployment. Chem Rev 2020, 120 (18), 9835–9950. https://doi.org/10.1021/acs.chemrev.9b00780.

(13) Ho-Baillie, A. W. Y.; Zheng, J.; Mahmud, M. A.; Ma, F.-J.; McKenzie, D. R.; Green, M. A. Recent Progress and Future Prospects of Perovskite Tandem Solar Cells. Appl Phys Rev 2021, 8 (4). https://doi.org/10.1063/5.0061483.

(14) George, S. D. B.; Soosaimanickam, A.; Sundaram, S. Third-Generation Photovoltaics: Introduction, Overview, Innovation, and Potential Markets. In Photovoltaics Beyond Silicon; Elsevier, 2024; pp 75–110. https://doi.org/10.1016/B978-0-323-90188-8.00020-8.

(15) Dale, P. J.; Scarpulla, M. A. Efficiency versus Effort: A Better Way to Compare Best Photovoltaic Research Cell Efficiencies? Solar Energy Materials and Solar Cells 2023, 251, 112097. https://doi.org/10.1016/j.solmat.2022.112097.

(16) Werner, J.; Niesen, B.; Ballif, C. Perovskite/Silicon Tandem Solar Cells: Marriage of Convenience or True Love Story? – An Overview. Adv Mater Interfaces 2018, 5 (1). https://doi.org/10.1002/admi.201700731.

(17) Yamaguchi, M.; Lee, K.-H.; Araki, K.; Kojima, N. A Review of Recent Progress in Heterogeneous Silicon Tandem Solar Cells. J Phys D Appl Phys 2018, 51 (13), 133002. https://doi.org/10.1088/1361-6463/aaaf08.

(18) Lal, N. N.; Dkhissi, Y.; Li, W.; Hou, Q.; Cheng, Y.; Bach, U. Perovskite Tandem Solar Cells. Adv Energy Mater 2017, 7 (18). https://doi.org/10.1002/aenm.201602761.

(19) K. Rao, M.; Sangeetha, D. N.; Selvakumar, M.; Sudhakar, Y. N.; Mahesha, M. G. Review on Persistent Challenges of Perovskite Solar Cells' Stability. Solar Energy 2021, 218, 469–491. https://doi.org/10.1016/j.solener.2021.03.005.

(20) Correa-Baena, J.-P.; Saliba, M.; Buonassisi, T.; Grätzel, M.; Abate, A.; Tress, W.; Hagfeldt, A. Promises and Challenges of Perovskite Solar Cells. Science 2017, 358 (6364), 739–744. https://doi.org/10.1126/science.aam6323.

(21) Adjogri, S. J.; Meyer, E. L. Chalcogenide Perovskites and Perovskite-Based Chalcohalide as Photoabsorbers: A Study of Their Properties, and Potential Photovoltaic Applications. Materials 2021, 14 (24), 7857. https://doi.org/10.3390/ma14247857.

(22) Raj, R.; Singh, R.; Guin, M. Chalcogenide Perovskite, An Emerging Photovoltaic Material: Current Status and Future Perspectives. ChemistrySelect 2023, 8 (45). https://doi.org/10.1002/slct.202303550.

(23) Sopiha, K. V; Comparotto, C.; Márquez, J. A.; Scragg, J. J. S. Chalcogenide Perovskites: Tantalizing Prospects, Challenging Materials. Advanced Optical Materials 2022, p 2101704. https://doi.org/10.1002/adom.202101704.

(24) Ju, M.; Dai, J.; Ma, L.; Zeng, X. C. Perovskite Chalcogenides with Optimal Bandgap and Desired Optical Absorption for Photovoltaic Devices. Adv Energy Mater 2017, 7 (18), 1700216. https://doi.org/10.1002/aenm.201700216.

(25) Sun, Y.-Y.; Agiorgousis, M. L.; Zhang, P.; Zhang, S. Chalcogenide Perovskites for Photovoltaics. Nano Lett 2015, 15 (1), 581–585. https://doi.org/10.1021/nl504046x.

(26) Tiwari, D.; Hutter, O. S.; Longo, G. Chalcogenide Perovskites for Photovoltaics: Current Status and Prospects. Journal of Physics: Energy 2021, 3 (3), 034010. https://doi.org/10.1088/2515-7655/abf41c.

(27) Li, W.; Niu, S.; Zhao, B.; Haiges, R.; Zhang, Z.; Ravichandran, J.; Janotti, A. Band Gap Evolution in Ruddlesden-Popper Phases. Phys Rev Mater 2019, 3 (10), 101601. https://doi.org/10.1103/PhysRevMaterials.3.101601.

(28) Niu, S.; Zhao, B.; Ye, K.; Bianco, E.; Zhou, J.; McConney, M. E.; Settens, C.; Haiges, R.; Jaramillo, R.; Ravichandran, J. Crystal Growth and Structural Analysis of Perovskite Chalcogenide BaZrS 3 and Ruddlesden–Popper Phase Ba3Zr2S7. J Mater Res 2019, 34 (22), 3819–3826. https://doi.org/10.1557/jmr.2019.348.

(29) Shahmohamadi, H.; Naghavi, S. S. Sulfide Perovskites for Thermoelectricity. ACS Appl Mater Interfaces 2021, 13 (12), 14189–14197. https://doi.org/10.1021/acsami.0c22842.

(30) Paudel, T. R.; Tsymbal, E. Y. Evaluating the Thermoelectric Properties of BaTiS3 by Density Functional Theory. ACS Omega 2020, 5 (21), 12385–12390. https://doi.org/10.1021/acsomega.0c01139.

(31) Shuhaib, J. H. Al; Fernández, J. F.; Bodega, J.; Ares, J. R.; Ferrer, I. J.; Leardini, F. Synthesis, Optical Band Gap and Thermoelectric Properties of Sr1+xTiS3-y Chalcogenide Perovskites. Mater Res Bull 2023, 167, 112405. https://doi.org/10.1016/j.materresbull.2023.112405.

(32) Feng, W.; Zhao, R.; Wang, X.; Xing, B.; Zhang, Y.; He, X.; Zhang, L. Global Instability Index as a Crystallographic Stability Descriptor of Halide and Chalcogenide Perovskites. Journal of Energy Chemistry 2022, 70, 1–8. https://doi.org/10.1016/j.jechem.2022.02.018.

(33) Swarnkar, A.; Mir, W. J.; Chakraborty, R.; Jagadeeswararao, M.; Sheikh, T.; Nag, A. Are Chalcogenide Perovskites an Emerging Class of Semiconductors for Optoelectronic Properties and Solar Cell? †. Chemistry of Materials 2019, pp 565–575. https://doi.org/10.1021/acs.chemmater.8b04178.

(34) Peng, Y.; Sun, Q.; Chen, H.; Yin, W.-J. Disparity of the Nature of the Band Gap between Halide and Chalcogenide Single Perovskites for Solar Cell Absorbers. J Phys Chem Lett 2019, 10 (16), 4566–4570. https://doi.org/10.1021/acs.jpclett.9b01657.

(35) Hüttig, G. F. Notiz Zur Geometrie Der Koordinationszahl. Z Anorg Allg Chem 1920, 114 (1), 24–26. https://doi.org/10.1002/zaac.19201140103.

(36) Li, C.; Soh, K. C. K.; Wu, P. Formability of ABO3 Perovskites. J Alloys Compd 2004, 372 (1–2), 40–48. https://doi.org/10.1016/j.jallcom.2003.10.017.

(37) Jensen, W. B.; Jensen, W. B. The Origin of the Ionic-Radius Ratio Rules. J Chem Educ 2010, 87 (6), 587–588. https://doi.org/10.1021/ed100258f.

(38) Glazer, A. M. The Classification of Tilted Octahedra in Perovskites. Acta Crystallogr B 1972, 28 (11), 3384–3392. https://doi.org/10.1107/S0567740872007976.

(39) Goldschmidt, V. M. Die Gesetze Der Krystallochemie. Naturwissenschaften 1926, 14 (21), 477–485. https://doi.org/10.1007/BF01507527.

(40) Perera, S.; Hui, H.; Zhao, C.; Xue, H.; Sun, F.; Deng, C.; Gross, N.; Milleville, C.; Xu, X.; Watson, D. F.; Weinstein, B.; Sun, Y. Y.; Zhang, S.; Zeng, H. Chalcogenide Perovskites - an Emerging Class of Ionic Semiconductors. Nano Energy 2016, 22, 129–135. https://doi.org/10.1016/j.nanoen.2016.02.020.

(41) Eya, H. I.; Ntsoenzok, E.; Dzade, N. Y. First–Principles Investigation of the Structural, Elastic, Electronic, and Optical Properties of α– and β–SrZrS3: Implications for Photovoltaic Applications. Materials 2020, 13 (4), 978. https://doi.org/10.3390/ma13040978.

(42) Han, M. L.; Hu, Y. Structural, Electronic, Elastic, and Optical Properties of Chalcogenide Perovskite SrZrS3 under Ambient and High-Pressure Conditions. Chalcogenide Letters 2023, 20 (8), 619–628. https://doi.org/10.15251/CL.2023.208.619.

(43) Hanzawa, K.; Iimura, S.; Hiramatsu, H.; Hosono, H. Material Design of Green-Light-Emitting Semiconductors: Perovskite-Type Sulfide SrHfS3. J Am Chem Soc 2019, 141 (13), 5343–5349. https://doi.org/10.1021/jacs.8b13622.

(44) Han, Y.; Fang, J.; Liang, Y.; Gao, H.; Yang, J.; Chen, X.; Yuan, Y.; Shi, Z. Preparation of Chalcogenide Perovskite SrHfS3 and Luminescent SrHfS3:Eu2 + Thin Films. Appl Phys Lett 2024, 124 (13). https://doi.org/10.1063/5.0200555.

(45) Liang, Y.; Li, J.; Chen, Z.; Li, G.; Li, M.; Jia, M.; Chen, X.; Li, X.; Han, Y.; Shi, Z. Tapping the Light Emitting Potential of Chalcogenide Perovskite SrHfS3 via Eu 2+ Doping. Adv Opt Mater 2024, 12 (6). https://doi.org/10.1002/adom.202301977.

(46) Zhang, H.; Wu, X.; Ding, K.; Xie, L.; Yang, K.; Ming, C.; Bai, S.; Zeng, H.; Zhang, S.; Sun, Y.-Y. Prediction and Synthesis of a Selenide Perovskite for Optoelectronics. Chemistry of Materials 2023, 35 (11), 4128–4135. https://doi.org/10.1021/acs.chemmater.2c03676.

(47) Du, J.; Shi, J.; Guo, W.; Liu, S.; He, Y.; Tian, C.; Zhu, Y.; Zhong, H. Cerium-Based Lead-Free Chalcogenide Perovskites for Photovoltaics. Phys Rev B 2021, 104 (23), 235206. https://doi.org/10.1103/PhysRevB.104.235206.

(48) Han, Y.; Xu, J.; Liang, Y.; Chen, X.; Jia, M.; Zhang, J.; Lian, L.; Liu, Y.; Li, X.; Shi, Z. P-Type Conductive BaZrS3 Thin Film and Its Band Gap Tunning via Ruddlesden-Popper Ba3Zr2S7 and Titanium Alloying. Chemical Engineering Journal 2023, 473, 145351. https://doi.org/10.1016/j.cej.2023.145351.

(49) Zhang, Y.; Shimada, T.; Kitamura, T.; Wang, J. Ferroelectricity in Ruddlesden–Popper Chalcogenide Perovskites for Photovoltaic Application: The Role of Tolerance Factor. J Phys Chem Lett 2017, 8 (23), 5834–5839. https://doi.org/10.1021/acs.jpclett.7b02591.

(50) Niu, S.; Sarkar, D.; Williams, K.; Zhou, Y.; Li, Y.; Bianco, E.; Huyan, H.; Cronin, S. B.; McConney, M. E.; Haiges, R.; Jaramillo, R.; Singh, D. J.; Tisdale, W. A.; Kapadia, R.; Ravichandran, J. Optimal Bandgap in a 2D Ruddlesden–Popper Perovskite Chalcogenide for Single-Junction Solar Cells. Chemistry of Materials 2018, 30 (15), 4882–4886. https://doi.org/10.1021/acs.chemmater.8b01707.

(51) Ye, K.; Zhao, B.; Diroll, B. T.; Ravichandran, J.; Jaramillo, R. Time-Resolved Photoluminescence Studies of Perovskite Chalcogenides. Faraday Discuss 2022, 239, 146–159. https://doi.org/10.1039/D2FD00047D.

(52) L. Agiorgousis, M.; Sun, Y.; Choe, D.; West, D.; Zhang, S. Machine Learning Augmented Discovery of Chalcogenide Double Perovskites for Photovoltaics. Adv Theory Simul 2019, 2 (5). https://doi.org/10.1002/adts.201800173.

(53) Sun, Q.; Chen, H.; Yin, W.-J. Do Chalcogenide Double Perovskites Work as Solar Cell Absorbers: A First-Principles Study. Chemistry of Materials 2019, 31 (1), 244–250. https://doi.org/10.1021/acs.chemmater.8b04320.

(54) Kassa, M. D.; Debelo, N. G.; Woldemariam, M. M. First-Principles Calculations to Investigate Small Band Gap Ca2ZrHfS6 Double Chalcogenide Perovskites for Optoelectronic Application. Indian Journal of Physics 2023. https://doi.org/10.1007/s12648-023-02905-7.

(55) Jess, A.; Yang, R.; Hages, C. J. On the Phase Stability of Chalcogenide Perovskites. Chemistry of Materials 2022, 30 (3), 679–684. https://doi.org/10.1021/acs.chemmater.2c01289.

(56) Turnley, J.; Agarwal, S.; Agrawal, R. Rethinking Tolerance Factor Analysis for Chalcogenide Perovskites. Mater Horiz 2024. https://doi.org/10.1039/D4MH00689E.

(57) Wei, X.; Hui, H.; Perera, S.; Sheng, A.; Watson, D. F.; Sun, Y.-Y.; Jia, Q.; Zhang, S.; Zeng, H. Ti-Alloying of BaZrS3 Chalcogenide Perovskite for Photovoltaics. ACS Omega 2020, 5 (30), 18579–18583. https://doi.org/10.1021/acsomega.0c00740.

(58) Liu, D.; Peng, H.; He, J.; Sa, R. Alloy Engineering to Tune the Optoelectronic Properties and Photovoltaic Performance for Hf-Based Chalcogenide Perovskites. Mater Sci Semicond Process 2024, 169, 107919. https://doi.org/10.1016/j.mssp.2023.107919.

(59) Kanoun, M. B.; Ul Haq, B.; Kanoun, A.-A.; Goumri-Said, S. Ti Alloying as a Route to BaZrS3 Chalcogenide Perovskite with Enhanced Photovoltaic Performance. Energy & Fuels 2023, 37 (13), 9548–9556. https://doi.org/10.1021/acs.energyfuels.3c01272.

(60) Chami, R.; Lekdadri, A.; Chafi, M.; Omari, L. H.; Hlil, E. K. Sn-Alloying of BaZrS3 Chalcogenide Perovskite as Eco-Friendly Material for Photovoltaics: First Principle Insight. Solid State Commun 2023, 369, 115212. https://doi.org/10.1016/j.ssc.2023.115212.

(61) Ye, K.; Sadeghi, I.; Xu, M.; Van Sambeek, J.; Cai, T.; Dong, J.; Kothari, R.; LeBeau, J. M.; Jaramillo, R. A Processing Route to Chalcogenide Perovskites Alloys with Tunable Band Gap via Anion Exchange. Adv Funct Mater 2024. https://doi.org/10.1002/adfm.202405135.

(62) Gupta, T.; Ghoshal, D.; Yoshimura, A.; Basu, S.; Chow, P. K.; Lakhnot, A. S.; Pandey, J.; Warrender, J. M.; Efstathiadis, H.; Soni, A.; Osei-Agyemang, E.; Balasubramanian, G.; Zhang, S.; Shi, S.; Lu, T.; Meunier, V.; Koratkar, N. An Environmentally Stable and Lead-Free Chalcogenide Perovskite. Adv Funct Mater 2020, 30 (23), 2001387. https://doi.org/10.1002/adfm.202001387.

(63) Bystrický, R.; Tiwari, S. K.; Hutár, P.; Sýkora, M. Thermal Stability of Chalcogenide Perovskites. Inorg Chem 2024, 63 (28), 12826–12838. https://doi.org/10.1021/acs.inorgchem.4c01308.

(64) Niu, S.; Milam-Guerrero, J.; Zhou, Y.; Ye, K.; Zhao, B.; Melot, B. C.; Ravichandran, J. Thermal Stability Study of Transition Metal Perovskite Sulfides. J Mater Res 2018, 33 (24), 4135–4143. https://doi.org/10.1557/jmr.2018.419.

(65) Ravi, V. K.; Yu, S. H.; Rajput, P. K.; Nayak, C.; Bhattacharyya, D.; Chung, D. S.; Nag, A. Colloidal BaZrS3 Chalcogenide Perovskite Nanocrystals for Thin Film Device Fabrication. Nanoscale 2021, 13 (3), 1616–1623. https://doi.org/10.1039/D0NR08078K.

(66) Yang, Z.; Han, Y.; Liang, Y.; Shen, W.; Zhang, Z.; Fang, C.; Wang, Q.; Wan, B.; Chen, L.; Zhang, Y.; Jia, X. Chalcogenide Perovskite BaZrS3 Bulks for Thermoelectric Conversion with Ultra-High Carrier Mobility and Low Thermal Conductivity. Acta Mater 2024, 276, 120156. https://doi.org/10.1016/j.actamat.2024.120156.

(67) Nishigaki, Y.; Nagai, T.; Nishiwaki, M.; Aizawa, T.; Kozawa, M.; Hanzawa, K.; Kato, Y.; Sai, H.; Hiramatsu, H.; Hosono, H.; Fujiwara, H. Extraordinary Strong Band-Edge Absorption in Distorted Chalcogenide Perovskites. Solar RRL 2020, 4 (5), 1900555. https://doi.org/10.1002/solr.201900555.

(68) Márquez, J. A.; Rusu, M.; Hempel, H.; Ahmet, I. Y.; Kölbach, M.; Simsek, I.; Choubrac, L.; Gurieva, G.; Gunder, R.; Schorr, S.; Unold, T. BaZrS3 Chalcogenide Perovskite Thin Films by H2S Sulfurization of Oxide Precursors. J Phys Chem Lett 2021, 12 (8), 2148–2153. https://doi.org/10.1021/acs.jpclett.1c00177.

(69) Filippone, S.; Song, S.; Jaramillo, R. High Densification of BaZrS3 Powder Inspired by the Cold-Sintering Process. J Mater Res 2021, 36 (21), 4404–4412. https://doi.org/10.1557/s43578-021-00404-1.

(70) Kuhar, K.; Crovetto, A.; Pandey, M.; Thygesen, K. S.; Seger, B.; Vesborg, P. C. K.; Hansen, O.; Chorkendorff, I.; Jacobsen, K. W. Sulfide Perovskites for Solar Energy Conversion Applications: Computational Screening and Synthesis of the Selected Compound LaYS3. Energy Environ Sci 2017, 10 (12), 2579–2593. https://doi.org/10.1039/C7EE02702H.

(71) Du, J.; Shi, J. 2D Ca3Sn2S7 Chalcogenide Perovskite: A Graphene-Like Semiconductor with Direct Bandgap 0.5 eV and Ultrahigh Carrier Mobility 6.7×10^4 Cm^2 V^{-1} s^{-1}. Advanced Materials 2019, 31 (51). https://doi.org/10.1002/adma.201905643.

(72) Surendran, M.; Chen, H.; Zhao, B.; Thind, A. S.; Singh, S.; Orvis, T.; Zhao, H.; Han, J.-K.; Htoon, H.; Kawasaki, M.; Mishra, R.; Ravichandran, J. Epitaxial Thin Films of a Chalcogenide Perovskite. Chemistry of Materials 2021, 33 (18), 7457–7464. https://doi.org/10.1021/acs.chemmater.1c02202.

(73) Agarwal, S.; Turnley, J. W.; Pradhan, A. A.; Agrawal, R. Moderate Temperature Sulfurization and Selenization of Highly Stable Metal Oxides: An Opportunity for Chalcogenide Perovskites. J Mater Chem C Mater 2023, 11 (45), 15817–15823. https://doi.org/10.1039/D3TC02716C.

(74) Turnley, J. W.; Vincent, K. C.; Pradhan, A. A.; Panicker, I.; Swope, R.; Uible, M. C.; Bart, S. C.; Agrawal, R. Solution Deposition for Chalcogenide Perovskites: A Low-Temperature Route to BaMS3 Materials (M = Ti, Zr, Hf). J Am Chem Soc 2022, 144 (40), 18234–18239. https://doi.org/10.1021/jacs.2c06985.

(75) McLeod, S. M.; Hages, C. J.; Carter, N. J.; Agrawal, R. Synthesis and Characterization of 15% Efficient CIGSSe Solar Cells from Nanoparticle Inks. Progress in Photovoltaics: Research and Applications 2015, 23 (11), 1550–1556. https://doi.org/10.1002/pip.2588.

(76) Mitzi, D. B.; Yuan, M.; Liu, W.; Kellock, A. J.; Chey, S. J.; Gignac, L.; Schrott, A. G. Hydrazine-Based Deposition Route for Device-Quality CIGS Films. Thin Solid Films 2009, 517 (7), 2158–2162. https://doi.org/10.1016/j.tsf.2008.10.079.

(77) Guo, Q.; Ford, G. M.; Yang, W.-C.; Walker, B. C.; Stach, E. A.; Hillhouse, H. W.; Agrawal, R. Fabrication of 7.2% Efficient CZTSSe Solar Cells Using CZTS Nanocrystals. J Am Chem Soc 2010, 132 (49), 17384–17386. https://doi.org/10.1021/ja108427b.

(78) Agarwal, S.; Weideman, K.; Rokke, D.; Vincent, K. C.; Zemlyanov, D.; Agrawal, R. Enhancing the Optoelectronic Properties of Solution-Processed AgInSe2 Thin Films for Application in Photovoltaics. J Mater Chem C Mater 2024, 12 (1), 325–336. https://doi.org/10.1039/D3TC03540A.

(79) Turnley, J. W.; Agrawal, R. Solution Processed Metal Chalcogenide Semiconductors for Inorganic Thin Film Photovoltaics. Chemical Communications 2024, 60 (40), 5245–5269. https://doi.org/10.1039/D4CC01057D.

(80) Hahn, H.; Mutschke, U. Untersuchungen uber Ternare Chalkogenide. XI. Versuche Zur Darstellung von Thioperowskiten. Zeitschrift for anorganische und allgemeine Chemie 1957, 288 (5–6), 269–278. https://doi.org/10.1002/zaac.19572880505.

(81) Zilevu, D.; Creutz, S. E. Solution-Phase Synthesis of Group 3–5 Transition Metal Chalcogenide Inorganic Nanomaterials. Chemical Communications 2023, 59 (57), 8779–8798. https://doi.org/10.1039/D3CC01731A.

(82) Kepp, K. P. A Quantitative Scale of Oxophilicity and Thiophilicity. Inorg Chem 2016, 55 (18), 9461–9470. https://doi.org/10.1021/acs.inorgchem.6b01702.

(83) Gross, N.; Sun, Y. Y.; Perera, S.; Hui, H.; Wei, X.; Zhang, S.; Zeng, H.; Weinstein, B. A. Stability and Band-Gap Tuning of the Chalcogenide Perovskite BaZrS3 in Raman and Optical Investigations at High Pressures. Phys Rev Appl 2017, 8 (4), 18–21. https://doi.org/10.1103/PhysRevApplied.8.044014.

(84) Humphrey, N.; Tsung, A.; Singh, S.; Irshad, A.; Zhao, B.; Narayan, S.; Ravichandran, J.; Mallikarjun Sharada, S. The Hydrogen Evolution Activity of BaZrS3, BaTiS3, and BaVS3 Chalcogenide Perovskites. ChemPhysChem 2024, 25 (13). https://doi.org/10.1002/cphc.202300953.

(85) Kong, S.; Dong, H.; Yu, Z.; Guo, J.; Cao, K.; Chen, K.; Ke, X.; Zhou, C.; Deng, J.; Yang, S.; Zhang, Y. Ti–S Antibonding Coupling Enables Enhanced Bandgap Tuning in Ti-Substituted BaHfS3 Perovskite. Ceram Int 2024, 50 (7), 10889–10896. https://doi.org/10.1016/j.ceramint.2023.12.405.

(86) Wei, X.; Hui, H.; Zhao, C.; Deng, C.; Han, M.; Yu, Z.; Sheng, A.; Roy, P.; Chen, A.; Lin, J.; Watson, D. F.; Sun, Y. Y.; Thomay, T.; Yang, S.; Jia, Q.; Zhang, S.; Zeng, H. Realization of BaZrS3 Chalcogenide Perovskite Thin Films for Optoelectronics. Nano Energy 2020, 68, 104317. https://doi.org/10.1016/j.nanoen.2019.104317.

(87) Filippone, S. A.; Sun, Y. Y.; Jaramillo, R. Determination of Adsorption-Controlled Growth Windows of Chalcogenide Perovskites. MRS Commun 2018, 8 (1), 145–151. https://doi.org/10.1557/mrc.2018.10.

(88) Bystrický, R.; Tiwari, S. K.; Hutár, P.; Vančo, L.; Sýkora, M. Synthesis of Sulfide Perovskites by Sulfurization with Boron Sulfides. Inorg Chem 2022. https://doi.org/10.1021/acs.inorgchem.2c03200.

(89) Sadeghi, I.; Ye, K.; Xu, M.; Li, Y.; LeBeau, J. M.; Jaramillo, R. Making BaZrS3 Chalcogenide Perovskite Thin Films by Molecular Beam Epitaxy. Adv Funct Mater 2021, 31 (45), 2105563. https://doi.org/10.1002/adfm.202105563.

(90) Sadeghi, I.; Van Sambeek, J.; Simonian, T.; Xu, M.; Ye, K.; Cai, T.; Nicolosi, V.; LeBeau, J. M.; Jaramillo, R. Expanding the Perovskite Periodic Table to Include Chalcogenide Alloys with Tunable Band Gap Spanning 1.5–1.9 eV. Adv Funct Mater 2023, 33 (41). https://doi.org/10.1002/adfm.202304575.

(91) Surendran, M.; Zhao, B.; Ren, G.; Singh, S.; Avishai, A.; Chen, H.; Han, J.-K.; Kawasaki, M.; Mishra, R.; Ravichandran, J. Quasi-Epitaxial Growth of BaTiS3 Films. J Mater Res 2022, 37 (21), 3481–3490. https://doi.org/10.1557/s43578-022-00776-y.

(92) Sharma, S.; Ward, Z. D.; Bhimani, K.; Sharma, M.; Quinton, J.; Rhone, T. D.; Shi, S.-F.; Terrones, H.; Koratkar, N. Machine Learning-Aided Band Gap Engineering of BaZrS3 Chalcogenide Perovskite. ACS Appl Mater Interfaces 2023, 15 (15), 18962–18972. https://doi.org/10.1021/acsami.3c00618.

(93) Yu, Z.; Wei, X.; Zheng, Y.; Hui, H.; Bian, M.; Dhole, S.; Seo, J.-H.; Sun, Y.-Y.; Jia, Q.; Zhang, S.; Yang, S.; Zeng, H. Chalcogenide Perovskite BaZrS3 Thin-Film Electronic and Optoelectronic Devices by Low Temperature Processing. Nano Energy 2021, 85 (March), 105959. https://doi.org/10.1016/j.nanoen.2021.105959.

(94) Dhole, S.; Wei, X.; Hui, H.; Roy, P.; Corey, Z.; Wang, Y.; Nie, W.; Chen, A.; Zeng, H.; Jia, Q. A Facile Aqueous Solution Route for the Growth of Chalcogenide Perovskite BaZrS3 Films. Photonics 2023, 10 (4), 366. https://doi.org/10.3390/photonics10040366.

(95) Ramanandan, S. P.; Giunto, A.; Stutz, E. Z.; Reynier, B.; Lefevre, I. T. F. M.; Rusu, M.; Schorr, S.; Unold, T.; Fontcuberta I Morral, A.; Márquez, J. A.; Dimitrievska, M. Understanding the Growth Mechanism of BaZrS3 Chalcogenide Perovskite Thin Films from Sulfurized Oxide Precursors. Journal of Physics: Energy 2023, 5 (1), 014013. https://doi.org/10.1088/2515-7655/aca9fe.

(96) Sharma, S.; Ward, Z.; Bhimani, K.; Li, K.; Lakhnot, A.; Jain, R.; Shi, S.-F.; Terrones, H.; Koratkar, N. Bandgap Tuning in BaZrS3 Perovskite Thin Films. ACS Appl Electron Mater 2021, 3 (8), 3306–3312. https://doi.org/10.1021/acsaelm.1c00575.

(97) Comparotto, C.; Davydova, A.; Ericson, T.; Riekehr, L.; Moro, M. V.; Kubart, T.; Scragg, J. Chalcogenide Perovskite BaZrS3: Thin Film Growth by Sputtering and Rapid Thermal Processing. ACS Appl Energy Mater 2020, 3 (3), 2762–2770. https://doi.org/10.1021/acsaem.9b02428.

(98) Freund, T.; Cicconi, M. R.; Wellmann, P. Fabrication of Bariumtrisulphide Thin Films as Precursors for Chalcogenide Perovskites. physica status solidi (b) 2022, 1 (69), 5–24. https://doi.org/10.1002/pssb.202200094.

(99) Jamshaid, S.; Cicconi, M. R.; Heiss, W.; Webber, K. G.; Wellmann, P. J. Synthesis and Characterization of BaZrS3 Thin Films via Stacked Layer Methodology: A Comparative Study of BaZrS3 on Zirconium Foil and Silicon Carbide Substrates. Adv Eng Mater 2024. https://doi.org/10.1002/adem.202302161.

(100) Yang, R.; Nelson, J.; Fai, C.; Yetkin, H. A.; Werner, C.; Tervil, M.; Jess, A. D.; Dale, P. J.; Hages, C. J. A Low-Temperature Growth Mechanism for Chalcogenide Perovskites. Chemistry of Materials 2023, 35 (12), 4743–4750. https://doi.org/10.1021/acs.chemmater.3c00494.

(101) Vincent, K. C.; Agarwal, S.; Turnley, J. W.; Agrawal, R. Liquid Flux–Assisted Mechanism for Modest Temperature Synthesis of Large-Grain BaZrS3 and BaHfS3 Chalcogenide Perovskites. Advanced Energy and Sustainability Research 2023, 4 (5). https://doi.org/10.1002/aesr.202300010.

(102) Wang, Y.; Sato, N.; Fujino, T. Synthesis of BaZrS3 by Short Time Reaction at Lower Temperatures. J Alloys Compd 2001, 327 (1–2), 104–112. https://doi.org/10.1016/S0925-8388(01)01553-5.

(103) Agarwal, S.; Vincent, K. C.; Agrawal, R. Quantitative Scales for Haliphilicity of Metals: Tailoring the Halide Affinity of Alkaline Earth Metals to Synthesize Chalcogenide Perovskite BaMS3 (M = Zr, and Hf) and Cu2BaSnS4 Compounds. ACS Appl Energy Mater 2024, 7 (22), 10584–10595. https://doi.org/10.1021/acsaem.4c02205.

(104) Okamoto, H. Desk Handbook: Phase Diagrams for Binary Alloys; ASM International, 2010.

(105) Vincent, K. C.; Agarwal, S.; Fan, Z.; Canizales, A. S. M.; Agrawal, R. Expanding the Horizons for Viable Precursors and Liquid Fluxes for the Synthesis of BaZrS3 and Related Compounds. J Mater Chem C Mater 2024. https://doi.org/10.1039/D4TC02287D.

(106) Suresh, S.; Uhl, A. R. Present Status of Solution-Processing Routes for Cu(In,Ga)(S,Se)2 Solar Cell Absorbers. Adv Energy Mater 2021, 11 (14), 2003743. https://doi.org/10.1002/aenm.202003743.

(107) Suresh, S.; Rokke, D. J.; Drew, A. A.; Alruqobah, E.; Agrawal, R.; Uhl, A. R. Extrinsic Doping of Ink-Based Cu(In,Ga)(S,Se)2 -Absorbers for Photovoltaic Applications. Adv Energy Mater 2022, 2103961. https://doi.org/10.1002/aenm.202103961.

(108) Todorov, T. K.; Gunawan, O.; Gokmen, T.; Mitzi, D. B. Solution-Processed Cu(In,Ga)(S,Se)2 Absorber Yielding a 15.2% Efficient Solar Cell. Progress in Photovoltaics: Research and Applications 2013, 21 (1), 82–87. https://doi.org/10.1002/pip.1253.

(109) Suresh, S.; Uhl, A. R. Present Status of Solution-Processing Routes for Cu(In,Ga)(S,Se)2 Solar Cell Absorbers. Advanced Energy Materials 2021. https://doi.org/10.1002/aenm.202003743.

(110) McCarthy, C. L.; Brutchey, R. L. Solution Processing of Chalcogenide Materials Using Thiol–Amine “Alkahest” Solvent Systems. Chemical Communications 2017, 53 (36), 4888–4902. https://doi.org/10.1039/C7CC02226C.

(111) Mavlonov, A.; Razykov, T.; Raziq, F.; Gan, J.; Chantana, J.; Kawano, Y.; Nishimura, T.; Wei, H.; Zakutayev, A.; Minemoto, T.; Zu, X.; Li, S.; Qiao, L. A Review of Sb2Se3 Photovoltaic Absorber Materials and Thin-Film Solar Cells. Solar Energy 2020, 201, 227–246. https://doi.org/10.1016/j.solener.2020.03.009.

(112) Clark, J. A.; Murray, A.; Lee, J.; Autrey, T. S.; Collord, A. D.; Hillhouse, H. W. Complexation Chemistry in N,N -Dimethylformamide-Based Molecular Inks for Chalcogenide Semiconductors and Photovoltaic Devices. J Am Chem Soc 2019, 141 (1), 298–308. https://doi.org/10.1021/jacs.8b09966.

(113) Pradhan, A. Solution-Phase Synthesis of Earth Abundant Semiconductors for Photovoltaic Applications, Purdue University Graduate School, 2023.

(114) Deshmukh, S. D.; Ellis, R. G.; Sutandar, D. S.; Rokke, D. J.; Agrawal, R. Versatile Colloidal Syntheses of Metal Chalcogenide Nanoparticles from Elemental Precursors Using Amine-Thiol Chemistry. Chemistry of Materials 2019, 2. https://doi.org/10.1021/acs.chemmater.9b03401.

(115) Zhao, X.; Deshmukh, S. D.; Rokke, D. J.; Zhang, G.; Wu, Z.; Miller, J. T.; Agrawal, R. Investigating Chemistry of Metal Dissolution in Amine−Thiol Mixtures and Exploiting It toward Benign Ink Formulation for Metal Chalcogenide Thin Films. Chem. Mater 2019, 31 (15), 5674–5682. https://doi.org/10.1021/acs.chemmater.9b01566.

(116) McCarthy, C. L.; Brutchey, R. L. Solution Deposited Cu2BaSnS4– xSex from a Thiol–Amine Solvent Mixture. Chemistry of Materials 2018, 30 (2), 304–308. https://doi.org/10.1021/acs.chemmater.7b03931.

(117) Pradhan, A. A.; Uible, M. C.; Agarwal, S.; Turnley, J. W.; Khandelwal, S.; Peterson, J. M.; Blach, D. D.; Swope, R. N.; Huang, L.; Bart, S. C.; Agrawal, R. Synthesis of BaZrS3 and BaHfS3 Chalcogenide Perovskite Films Using Single-Phase Molecular Precursors at Moderate Temperatures. Angewandte Chemie International Edition 2023, 62 (15). https://doi.org/10.1002/anie.202301049.

(118) Thompson, J. R. Development of Single-Source CVD Precursors for Group IV, V and VI Metal Disulfides. PhD Thesis, University of Bath, 2016.

(119) Agarwal, S.; Vincent, K. C.; Turnley, J. W.; Hayes, D. C.; Uible, M. C.; Durán, I.; Canizales, A. S. M.; Khandelwal, S.; Panicker, I.; Andoh, Z.; Spilker, R. M.; Ma, Q.; Huang, L.; Hwang, S.; Kisslinger, K.; Svatek, S.; Antolin, E.; Bart, S. C.; Agrawal, R. Breaking Barriers in Chalcogenide Perovskite Synthesis: A Generalized Framework for Fabrication of BaMS3 (M═Ti, Zr, Hf) Materials. Adv Funct Mater 2024, 34 (46). https://doi.org/10.1002/adfm.202405416.

(120) Kayastha, P.; Tiwari, D.; Holland, A.; Hutter, O. S.; Durose, K.; Whalley, L. D.; Longo, G. High-Temperature Equilibrium of 3D and 2D Chalcogenide Perovskites. Solar RRL 2023, 7 (9). https://doi.org/10.1002/solr.202201078.

(121) Kayastha, P.; Longo, G.; Whalley, L. D. A First-Principles Thermodynamic Model for the Ba–Zr–S System in Equilibrium with Sulfur Vapour. ACS Applied Energy Materials 2024. https://doi.org/10.1021/acsaem.3c03208

(122) Yuan, Z.; Dahliah, D.; Claes, R.; Pike, A.; Fenning, D. P.; Rignanese, G.-M.; Hautier, G. Assessing Carrier Mobility, Dopability, and Defect Tolerance in the Chalcogenide Perovskite BaZrS3. PRX Energy 2024. https://doi.org/10.1103/PRXEnergy.3.033008

(123) Pradhan, A.; Agarwal, S.; Vincent, K. C.; Hayes, D.; Peterson, J. M.; Turnley, J.; Spilker, R. M.; Uible, M.; Bart, S.; Huang, L.; Kisslinger, K.; Agrawal, R. Emergence of Ruddlesden-Popper Phases and

Other Pitfalls for Moderate Temperature Solution Deposited Chalcogenide Perovskites. Mater Chem Front 2024, 8, 3358-3372. https://doi.org/10.1039/D4QM00441H

(124) Zilevu, D.; Creutz, S. E. Shape-Controlled Synthesis of Colloidal Nanorods and Nanoparticles of Barium Titanium Sulfide. Chemistry of Materials 2021, 33 (13), 5137–5146. https://doi.org/10.1021/acs.chemmater.1c01193.

(125) Ingram, N. E.; Jordan, B. J.; Donnadieu, B.; Creutz, S. E. Barium and Titanium Dithiocarbamates as Precursors for Colloidal Nanocrystals of Emerging Optoelectronic Materials. Dalton Transactions 2021, 50 (44), 15978–15982. https://doi.org/10.1039/D1DT03018C.

(126) Hages, C. J.; Koeper, M. J.; Miskin, C. K.; Brew, K. W.; Agrawal, R. Controlled Grain Growth for High Performance Nanoparticle-Based Kesterite Solar Cells. Chemistry of Materials 2016, 28 (21), 7703–7714. https://doi.org/10.1021/acs.chemmater.6b02733.

(127) Yang, W.-C.; Miskin, C. K.; Carter, N. J.; Agrawal, R.; Stach, E. A. Compositional Inhomogeneity of Multinary Semiconductor Nanoparticles: A Case Study of Cu2ZnSnS4. Chemistry of Materials 2014, 26 (24), 6955–6962. https://doi.org/10.1021/cm502930d.

(128) McLeod, S. M.; Hages, C. J.; Carter, N. J.; Agrawal, R. Synthesis and Characterization of 15% Efficient CIGSSe Solar Cells from Nanoparticle Inks. Progress in Photovoltaics: Research and Applications 2015, 23 (11), 1550–1556. https://doi.org/10.1002/pip.2588.

(129) Rein, C.; Engberg, S.; Andreasen, J. W. Stable, Carbon-Free Inks of Cu2ZnSnS4 Nanoparticles Synthesized at Room Temperature Designed for Roll-to-Roll Fabrication of Solar Cell Absorber Layers. J Alloys Compd 2019, 787, 63–71. https://doi.org/10.1016/j.jallcom.2019.02.014.

(130) Paudel, T. R.; Tsymbal, E. Y. Evaluating the Thermoelectric Properties of BaTiS3 by Density Functional Theory. ACS Omega 2020, 5 (21), 12385–12390. https://doi.org/10.1021/acsomega.0c01139.

(131) Yang, F.; Li, K.; Fan, M.; Yao, W.; Fu, L.; Xiong, C.; Jiang, S.; Li, D.; Xu, M.; Chen, C.; Zhang, G.; Tang, J. Strongly Anisotropic Quasi-1D BaTiS3 Chalcogenide Perovskite for Near-Infrared Polarized Photodetection. Adv Opt Mater 2023, 11 (5). https://doi.org/10.1002/adom.202201859.

(132) Chen, H.; Singh, S.; Mei, H.; Ren, G.; Zhao, B.; Surendran, M.; Wang, Y.-T.; Mishra, R.; Kats, M. A.; Ravichandran, J. Molten Flux Growth of Single Crystals of Quasi-1D Hexagonal Chalcogenide BaTiS3. Journal of Materials Research 2024, 39, 1901–1910. https://doi.org/10.1557/s43578-024-01379-5

(133) Nagaveni, G. H.; I Sattigeri, N.; Halse, S. V.; Hodlur, R. M.; Murgunde, B. K.; Kalasad, M. N. Formation and Characterization of Oleylamine Stabilized Ceria Nanoparticles. Mater Today Proc 2022, 67, 210–214. https://doi.org/10.1016/j.matpr.2022.06.306.

(134) Shuhaib, J. H. Al; Fernández, J. F.; Bodega, J.; Ares, J. R.; Ferrer, I. J.; Leardini, F. Synthesis, Optical Band Gap and Thermoelectric Properties of Sr1+xTiS3-y Chalcogenide Perovskites. Mater Res Bull 2023, 167, 112405. https://doi.org/10.1016/j.materresbull.2023.112405.

(135) Yang, R.; Jess, A. D.; Fai, C.; Hages, C. J. Low-Temperature, Solution-Based Synthesis of Luminescent Chalcogenide Perovskite BaZrS3 Nanoparticles. J Am Chem Soc 2022, 144 (35), 15928–15931. https://doi.org/10.1021/jacs.2c06168.

(136) Zilevu, D.; Parks, O. O.; Creutz, S. E. Solution-Phase Synthesis of the Chalcogenide Perovskite Barium Zirconium Sulfide as Colloidal Nanomaterials. Chemical Communications 2022, 58 (75), 10512–10515. https://doi.org/10.1039/D2CC03494H.

(137) Hayes, D. C.; Agarwal, S.; Vincent, K. C.; Aimiuwu, I. M.; Pradhan, A. A.; Uible, M. C.; Bart, S. C.; Agrawal, R. A Reliable, Colloidal Synthesis Method of the Orthorhombic Chalcogenide Perovskite, BaZrS3, and Related ABS3 Nanomaterials (A = Sr, Ba; B = Ti, Zr, Hf): A Step Forward for Earth-Abundant, Functional Materials. Chem Sci 2025. https://doi.org/10.1039/D4SC06116K.

(138) Comparotto, C.; Ström, P.; Donzel-Gargand, O.; Kubart, T.; Scragg, J. J. S. Synthesis of BaZrS3 Perovskite Thin Films at a Moderate Temperature on Conductive Substrates. ACS Appl Energy Mater 2022, 5 (5), 6335–6343. https://doi.org/10.1021/acsaem.2c00704.

(139) Riva, S.; Mukherjee, S.; Butorin, S. M.; Comparotto, C.; Aggarwal, G.; Allan, A. R.; Johannesson, E.; Abdel-Hafiez, M.; Scragg, J.; Rensmo, H. Electronic Structure Characterization by Photoelectron Spectroscopy of BaZrS3 Perovskite Powder and Thin Film. ChemRxiv 2024. https://doi.org/10.26434/chemrxiv-2024-mgkv1.

(140) Xu, J.; Fan, Y.; Tian, W.; Ye, L.; Zhang, Y.; Tian, Y.; Han, Y.; Shi, Z. Enhancing the Optical Absorption of Chalcogenide Perovskite BaZrS3 by Optimizing the Synthesis and Post-Processing Conditions. J Solid State Chem 2022, 307, 122872. https://doi.org/10.1016/j.jssc.2021.122872.

(141) Mukherjee, S.; Riva, S.; Comparotto, C.; Johansson, F. O. L.; Man, G. J.; Phuyal, D.; Simonov, K. A.; Just, J.; Klementiev, K.; Butorin, S. M.; Scragg, J. J. S.; Rensmo, H. Interplay between Growth Mechanism, Materials Chemistry, and Band Gap Characteristics in Sputtered Thin Films of Chalcogenide Perovskite BaZrS3. ACS Appl Energy Mater 2023, 6 (22), 11642–11653. https://doi.org/10.1021/acsaem.3c02075.

(142) Wu, X.; Gao, W.; Chai, J.; Ming, C.; Chen, M.; Zeng, H.; Zhang, P.; Zhang, S.; Sun, Y.-Y. Defect Tolerance in Chalcogenide Perovskite Photovoltaic Material BaZrS3. Sci China Mater 2021, 64 (12), 2976–2986. https://doi.org/10.1007/s40843-021-1683-0.

(143) Meng, W.; Saparov, B.; Hong, F.; Wang, J.; Mitzi, D. B.; Yan, Y. Alloying and Defect Control within Chalcogenide Perovskites for Optimized Photovoltaic Application. Chemistry of Materials 2016, 28 (3), 821–829. https://doi.org/10.1021/acs.chemmater.5b04213.

(144) Eya, H. I.; Dzade, N. Y. First-Principles Investigation of Oxygen and Water Adsorption on (010), (100), and (111) Surfaces of BaZrS3 Chalcogenide Perovskite. The Journal of Physical Chemistry C 2024, 128 (43), 18409–18421. https://doi.org/10.1021/acs.jpcc.4c02395.

(145) Ye, K.; Menahem, M.; Salzillo, T.; Zhao, B.; Niu, S.; Knoop, F.; Sadeghi, I.; Hellman, O.; Ravichandran, J.; Jaramillo, R.; Yaffe, O. Vibrational Properties Differ between Halide and Chalcogenide Perovskite Semiconductors, and It Matters for Optoelectronic Performance. Phys. Rev. Materials 2024, 8, 085402. https://doi.org/10.1103/PhysRevMaterials.8.085402

(146) Zhao, B.; Chen, H.; Ahsan, R.; Hou, F.; Hoglund, E. R.; Singh, S.; Shanmugasundaram, M.; Zhao, H.; Krayev, A. V.; Htoon, H.; Hopkins, P. E.; Seidel, J.; Kapadia, R.; Ravichandran, J. Photoconductive Effects in Single Crystals of BaZrS3. ACS Photonics 2024, 11 (3), 1109–1116. https://doi.org/10.1021/acsphotonics.3c01563.

(147) Romagnoli, L.; Ciccioli, A.; Dale, P. J.; Yetkin, H. A.; Panetta, R.; Latini, A. A Simple Synthetic Approach to BaZrS3, BaHfS3, and Their Solid Solutions. Journal of the American Ceramic Society 2024, 107 (2), 698–703. https://doi.org/10.1111/jace.19506.

(148) Minoura, S.; Kodera, K.; Maekawa, T.; Miyazaki, K.; Niki, S.; Fujiwara, H. Dielectric Function of Cu(In,Ga)Se2-Based Polycrystalline Materials. J Appl Phys 2013, 113 (6). https://doi.org/10.1063/1.4790174.

(149) Kato, M.; Nishiwaki, M.; Fujiwara, H. Very High Oscillator Strength in the Band-Edge Light Absorption of Zincblende, Chalcopyrite, Kesterite, and Hybrid Perovskite Solar Cell Materials. Phys Rev Mater 2020, 4 (3), 035402. https://doi.org/10.1103/PhysRevMaterials.4.035402.

(150) Lombardi, G. A.; de Oliveira, F. M.; Teodoro, M. D.; Chiquito, A. J. Investigation of Trapping Levels in P-Type Zn3P2 Nanowires Using Transport and Optical Properties. Appl Phys Lett 2018, 112 (19). https://doi.org/10.1063/1.5026548.

(151) Nishikubo, R.; Saeki, A. Solution-Processed Bi2S3 Photoresistor Film To Mitigate a Trade-off between Morphology and Electronic Properties. J Phys Chem Lett 2018, 9 (18), 5392–5399. https://doi.org/10.1021/acs.jpclett.8b02218.

(152) Vidal, J.; Lany, S.; d'Avezac, M.; Zunger, A.; Zakutayev, A.; Francis, J.; Tate, J. Band-Structure, Optical Properties, and Defect Physics of the Photovoltaic Semiconductor SnS. Appl Phys Lett 2012, 100 (3). https://doi.org/10.1063/1.3675880.

(153) Aggarwal, G.; Mirza, A. S.; Riva, S.; Comparotto, C.; Frost, R. J. W.; Mukherjee, S.; Morales-Masis, M.; Rensmo, H.; Scragg, J. S. Charge Transport and Defects in Sulfur-Deficient Chalcogenide Perovskite BaZrS3. arXiv 2024. https://doi.org/10.48550/arXiv.2405.17327

(154) Zhou, P.; Schiettecatte, P.; Vandichel, M.; Rousaki, A.; Vandenabeele, P.; Hens, Z.; Singh, S. Synthesis of Colloidal WSe2 Nanocrystals: Polymorphism Control by Precursor-Ligand Chemistry. Cryst Growth Des 2021, 21 (3), 1451–1460. https://doi.org/10.1021/acs.cgd.0c01036.

(155) Kayastha, P.; Fransson, E.; Erhart, P.; Whalley, L. D. Octahedral Tilt-Driven Phase Transitions in BaZrS3 Chalcogenide Perovskite. arXiv 2024. https://doi.org/10.48550/arXiv.2411.14289

(156) Jaiswal, A.; Sakharov, K. A.; Lekina, Y.; Kamonsuangkasem, K.; Tomm, Y.; Wei, F.; White, T. J. High-Temperature Polymorphism and Band-Gap Evolution in BaZrS3. Inorg Chem 2024. https://doi.org/10.1021/acs.inorgchem.4c03895.

(157) Li, Q.; Yan, L.; Chu, W.; He, J.; Luo, H.; Frauenheim, T.; Tretiak, S.; Zhou, L. Control of Polaronic Behavior and Carrier Lifetimes via Metal and Anion Alloying in Chalcogenide Perovskites. J Phys Chem Lett 2022, 4955–4962. https://doi.org/10.1021/acs.jpclett.2c00880.

(158) Zilevu, D.; Miller, K.; Arrykova, N.; Locke, A.; Creutz, S. Solution-Phase Synthesis of Alloyed Ba(Zr1-XTix)S3 Perovskite and Non-Perovskite Nanomaterials. Nanoscale 2024,16, 17126-17140. 2024. https://doi.org/10.1039/D4NR02412E

(159) Tranchitella, L. J.; Fettinger, J. C.; Dorhout, P. K.; Van Calcar, P. M.; Eichhorn, B. W. Commensurate Columnar Composite Compounds: Synthesis and Structure of Ba 15 Zr 14 Se 42 and Sr 21 Ti19Se57. J Am Chem Soc 1998, 120 (30), 7639–7640. https://doi.org/10.1021/ja972442p.

(160) Ong, M.; Guzman, D. M.; Campbell, Q.; Dabo, I.; Jishi, R. A. BaZrSe3: Ab Initio Study of Anion Substitution for Bandgap Tuning in a Chalcogenide Material. J Appl Phys 2019, 125 (23). https://doi.org/10.1063/1.5097940.

(161) Zitouni, H.; Tahiri, N.; El Bounagui, O.; Ez-Zahraouy, H. Electronic, Optical and Transport Properties of Perovskite BaZrS3 Compound Doped with Se for Photovoltaic Applications. Chem Phys 2020, 538, 110923. https://doi.org/10.1016/j.chemphys.2020.110923.

(162) Rong, Z.; Zhi, C.; Jun, C. Ab Initio Calculation of Mechanical, Electronic and Optical Characteristics of Chalcogenide Perovskite BaZrS3 at High Pressures. Acta Crystallogr C Struct Chem 2022, 78 (10), 570–577. https://doi.org/10.1107/S2053229622009147.

(163) Wu, J.; Wang, N.; Yan, X.; Wang, H. Emerging Low-Dimensional Materials for Mid-Infrared Detection. Nano Res 2021, 14 (6), 1863–1877. https://doi.org/10.1007/s12274-020-3128-7.

(164) Niu, S.; Joe, G.; Zhao, H.; Zhou, Y.; Orvis, T.; Huyan, H.; Salman, J.; Mahalingam, K.; Urwin, B.; Wu, J.; Liu, Y.; Tiwald, T. E.; Cronin, S. B.; Howe, B. M.; Mecklenburg, M.; Haiges, R.; Singh, D. J.; Wang, H.; Kats, M. A.; Ravichandran, J. Giant Optical Anisotropy in a Quasi-One-Dimensional Crystal. Nat Photonics 2018, 12 (7), 392–396. https://doi.org/10.1038/s41566-018-0189-1.

(165) Sun, B.; Niu, S.; Hermann, R. P.; Moon, J.; Shulumba, N.; Page, K.; Zhao, B.; Thind, A. S.; Mahalingam, K.; Milam-Guerrero, J.; Haiges, R.; Mecklenburg, M.; Melot, B. C.; Jho, Y.-D.; Howe, B. M.; Mishra, R.; Alatas, A.; Winn, B.; Manley, M. E.; Ravichandran, J.; Minnich, A. J. High Frequency Atomic Tunneling Yields Ultralow and Glass-like Thermal Conductivity in Chalcogenide Single Crystals. Nat Commun 2020, 11 (1), 6039. https://doi.org/10.1038/s41467-020-19872-w.

(166) Das, A.; Halpati, J. S.; Raj, V.; Chandiran, A. K. Highly Stable BaZrS3 Chalcogenide Perovskites for Photoelectrochemical Water Oxidation. Energy & Fuels 2024, 38 (22), 22527–22535. https://doi.org/10.1021/acs.energyfuels.4c03175.

(167) Dallas, P.; Gkini, K.; Kaltzoglou, A.; Givalou, L.; Konstantakou, M.; Orfanoudakis, S.; Boukos, N.; Sakellis, E.; Tsipas, P.; Kalafatis, A.; Karydas, A. G.; Lagogiannis, A.; Falaras, P.; Psycharis, V.; Stergiopoulos, T. Exploring the Potential of Powder-to-Film Processing for Proof-of-Concept BaZrS3 Perovskite Solar Cells. Mater Today Commun 2024, 39, 108608. https://doi.org/10.1016/j.mtcomm.2024.108608.

(168) Eya, H. I.; Dzade, N. Y. Density Functional Theory Insights into the Structural, Electronic, Optical, Surface, and Band Alignment Properties of BaZrS3 Chalcogenide Perovskite for Photovoltaics. ACS Appl Energy Mater 2023, 6 (11), 5729–5738. https://doi.org/10.1021/acsaem.3c00103.

(169) Karthick, S.; Velumani, S.; Bouclé, J. Chalcogenide BaZrS3 Perovskite Solar Cells: A Numerical Simulation and Analysis Using SCAPS-1D. Opt Mater (Amst) 2022, 126, 112250. https://doi.org/10.1016/j.optmat.2022.112250.

(170) Barman, B.; Ingole, S. Analysis of Si Back-Contact for Chalcogenide Perovskite Solar Cells Based on BaZrS3 Using SCAPS-1D. Adv Theory Simul 2023, 6 (7). https://doi.org/10.1002/adts.202200820.

(171) Karthick, S.; Velumani, S.; Bouclé, J. Experimental and SCAPS Simulated Formamidinium Perovskite Solar Cells: A Comparison of Device Performance. Solar Energy 2020, 205, 349–357. https://doi.org/10.1016/j.solener.2020.05.041.

(172) Vincent Mercy, E. N.; Srinivasan, D.; Marasamy, L. Emerging BaZrS3 and Ba(Zr,Ti)S3 Chalcogenide Perovskite Solar Cells: A Numerical Approach Toward Device Engineering and Unlocking Efficiency. ACS Omega 2024, 9 (4), 4359–4376. https://doi.org/10.1021/acsomega.3c06627.

(173) Pal, D.; Almawgani, A. H. M.; Das, S.; Pal, A.; Rahman, Md. F.; Alhawari, A. R. H.; Bhattarai, S. Numerical Investigation of a High-Efficiency BaZr x Ti 1− x S 3 Chalcogenide Perovskite Solar Cell. New Journal of Chemistry 2024, 48 (6), 2474–2483. https://doi.org/10.1039/D3NJ04832B.

(174) Rono, N.; Ahia, C. C.; Meyer, E. L. A Numerical Simulation and Analysis of Chalcogenide BaZrS3-Based Perovskite Solar Cells Utilizing Different Hole Transport Materials. Results Phys 2024, 61, 107722. https://doi.org/10.1016/j.rinp.2024.107722.

(175) El-Naggar, A. A.; Lotfy, L. A.; Felfela, A. A.; Ismail, W.; Abdelfatah, M.; Sharshir, S. W.; El-Shaer, A. Numerical Simulation Based Performance Enhancement Approach for an Inorganic BaZrS3/CuO Heterojunction Solar Cell. Sci Rep 2024, 14 (1), 7614. https://doi.org/10.1038/s41598-024-57636-4.

(176) Osei-Agyemang, E.; Koratkar, N.; Balasubramanian, G. Examining the Electron Transport in Chalcogenide Perovskite BaZrS3. J Mater Chem C Mater 2021, 9 (11), 3892–3900. https://doi.org/10.1039/D1TC00374G.

(177) Osei-Agyemang, E.; Balasubramanian, G. Understanding the Extremely Poor Lattice Thermal Transport in Chalcogenide Perovskite BaZrS3. ACS Appl Energy Mater 2020, 3 (1), 1139–1144. https://doi.org/10.1021/acsaem.9b02185.

(178) Li, M.; Zhao, S.; Li, B.; Zu, X.; Qiao, L.; Xiao, H. Effects of Hydrostatic Pressure on the Thermoelectric Performance of BaZrS3. The European Physical Journal Plus 2023, 138 (2), 149. https://doi.org/10.1140/epjp/s13360-023-03741-8.

(179) Wu, Y.; Chen, Y.; Fang, Z.; Ding, Y.; Li, Q.; Xue, K.; Shao, H.; Zhang, H.; Zhou, L. Ultralow Lattice Thermal Transport and Considerable Wave-like Phonon Tunneling in Chalcogenide Perovskite BaZrS3. J Phys Chem Lett 2023, 14 (50), 11465–11473. https://doi.org/10.1021/acs.jpclett.3c02940.

(180) Yu, Z.; Deng, C.; Kong, S.; Hui, H.; Guo, J.; Zhao, Q.; Tian, F.; Zhou, C.; Zhang, Y.; Yang, S.; Zeng, H. Transition Metal-Doped Chalcogenide Perovskite Magnetic Semiconductor BaZrS3. J Magn Magn Mater 2022, 563, 169886. https://doi.org/10.1016/j.jmmm.2022.169886.

(181) Yaghoubi, A.; Patterson, R.; Hao, X. Exotic Ferroelectricity in Strained BaZrS3 Chalcogenide Perovskite for Photovoltaics. Commun Mater 2024, 5 (1), 262. https://doi.org/10.1038/s43246-024-00705-y.

(182) Abir, S. S. H.; Sharma, S.; Sharma, P.; Karla, S.; Balasubramanian, G.; Samuel, J.; Koratkar, N. Piezoelectricity in Chalcogenide Perovskites. Nat Commun 2024, 15 (1), 5768. https://doi.org/10.1038/s41467-024-50130-5.

(183) Bennett, J. W.; Grinberg, I.; Rappe, A. M. Effect of Substituting of S for O: The Sulfide Perovskite BaZrS3 Investigated with Density Functional Theory. Phys Rev B 2009, 79 (23), 235115. https://doi.org/10.1103/PhysRevB.79.235115.

(184) Huo, Z.; Wei, S.-H.; Yin, W.-J. High-Throughput Screening of Chalcogenide Single Perovskites by First-Principles Calculations for Photovoltaics. J Phys D Appl Phys 2018, 51 (47), 474003. https://doi.org/10.1088/1361-6463/aae1ee.